UNIVERSITY OF CALIFORNIA,
IRVINE

Two-Layer and Two-Phase Modeling of Shallow Flows with Dam-Break and Swash Zone Applications

DISSERTATION

submitted in partial satisfaction of the requirements
for the degree of

DOCTOR OF PHILOSOPHY

in Civil and Environmental Engineering

by

Morteza Shakeri Majd

Dissertation Committee:
Professor Brett F. Sanders, Chair
Professor Amir Aghakouchak
Professor Russell Detwiler

2015

DEDICATION

To
my kind, passionate, caring parents,
and my beautiful, warm, loving daughter.

TABLE OF CONTENTS

LIST OF FIGURES

LIST OF TABLES

ACKNOWLEDGMENTS

In September 2010, I started graduate school at UC Irvine with little knowledge of life in the US. It has been more than five years from starting date of this remarkable journey. Number of people that made this journey possible, and helped me along this way. First and foremost, I would like to express my sincere gratitude to my very kind adviser, mentor, and guide, Prof. Brett F. Sanders. His patience, care and nurturing helped me to adapt at UCI. What is more, Prof. Sanders provided so many insightful discussions about research, and life in general. His deep knowledge and understanding of different fields of study enabled me to progress on different fronts and maximize my research output. His astute guidance and remarkable personality encouraged me to find the right resources to craft solutions to research questions. I am also grateful for his generous funding support, careful editing of my papers, and for being so accessible!

I would also like to thank my committee members, Profs. Amir Aghakouchak and Russell Detwiler, for their supports, flexibility and care. I remember Profs. Amir Aghakouchak and Russell Detwiler classes which taught me the basics of modeling and analyzing extreme events, and I also am deeply grateful for their perceptive discussions. I appreciate all I learned from my committee members on developing a career in academia.

I would also like to acknowledge my friends role in my life and thank them for their support, passion and help. Thank you Mojtaba Sadegh, Reza Sobhani, Nasrin Nasrollahi, Mahdieh Allahviranloo, Mahdi Navari, Neda Masoud, Ali Hojjat, and others. Moreover, thank you my office mates Ali Zafarani, Pasha Ameli, Trevor Jones, Ricardo Medina, Wade Monsen and Adam Luke for providing such a nice and friendly environment. I would also like to thank Dr.s Timu W. Gallien and Jochen E. Schubert for being so accessible and their remarkable help in my publications.

This work was supported by the Infrastructure Management and Extreme Events program of the National Science Foundation (CMMI-1129730), and was made possible by the gracious cooperation of City of Newport Beach personnel who authorized access to the site and provided equipment and operators to construct the beach berms. Also, I appreciate financial support from Department of Civil Engineering at UC Irvine.

Most importantly thank you my beautiful mom, Monir, my kind dad, M. Taghi, and my sibling Moin, Matin and Moshir for their unconditional love and support. I would like also thank my beautiful and precious daughter, Shawna, for being the most important part of my life.

CURRICULUM VITAE

Morteza Shakeri Majd

EDUCATION

Doctor of Philosophy in Civil and Environmental Engineering **2015**
University of California, Irvine *Irvine, California*

Master of Science in Civil and Environmental Engineering **2003**
Tahsilat Takmili of Tehran *Tehran, Iran*

Bachelor of Science in Civil and Environmental Engineering **2001**
Guilan University *Rasht, Iran*

RESEARCH EXPERIENCE

Graduate Research Assistant **2010–2015**
University of California, Irvine *Irvine, California*

Lecturer, Faculty **2003–2008**
Anzali Port University *Anzali Port, Iran*

Civil Engineer **2000-2003**
Shomal Consulting Engineers Co. *Rasht, Iran*

TEACHING EXPERIENCE

Teaching Assistant: Introduction to fluid mechanics **2012–2014**
University of California, Irvine *Irvine, California*

Instructor: fluid mechanics **Fall semesters 2003-2008**
Instructor: Hydrology **Winter semesters 2003-2008**
Anzali Port University *Anzali Port, Iran*

REFEREED JOURNAL PUBLICATIONS

M.S. Majd, T.W. Gallien, J.E. Schubert, B.F. Sanders, Multi-Phase Shock-Capturing Model of Beach Hydromorphodynamics **2015**
Journal of Coastal Engineering, In Review

J.E. Schubert, T.W. Gallien, M.S. Majd, B.F. Sanders, Terrestrial laser scanning of anthropogenic beach berm erosion and overtopping **2015**
Journal of Coastal Research,1,47–60

M.S. Majd, and B.F. Sanders , The LHLLC scheme for Two-Layer and Two-Phase transcritical flows overa mobile bed with avalanching, wetting and drying **2014**
Advances in Water Resources, 67, 1631,

REFEREED CONFERENCE PUBLICATIONS

M.S. Majd, and B.F. One Dimensional Modeling of Anthropogenic Beach Berm Erosion **2013**
American Geophysical Union (AGU),, San Francisco, USA

M.S. Majd, and B.F. Godunov-Based model of the swash zone dynamics to advance coastal flood predictio **2012**
American Geophysical Union (AGU),, San Francisco, USA

SOFTWARE

MATLAB, FORTRAN

ABSTRACT OF THE DISSERTATION

Two-Layer and Two-Phase Modeling of Shallow Flows with Dam-Break and Swash Zone Applications

By

Morteza Shakeri Majd

Doctor of Philosophy in Civil and Environmental Engineering

University of California, Irvine, 2015

Professor Brett F. Sanders, Chair

Coastal areas are important habitats and contain large human populations. It is estimated that 20 million people reside along coasts below normal high tide levels and over 200 million people are vulnerable to coastal flooding during storms. Many communities are currently protected from flooding by beaches that are sometimes modified with anthropogenic (artificial) berms, so understanding and characterizing beach and berm response to storm waves is critical to adapting and mitigating climate change effects. Beach dynamics are challenging to model because of the complexity of wave dynamics, sediment transport and bed profile adjustments.

This dissertation aims to advance the state of the art in coastal flood prediction by improving modeling of beach dynamics over times scales of hours, when a combination of high tides, storm surge and waves from a storm event can threaten flooding. It is envisioned that with advances in laser scanning technology, beach profiles can be rapidly assessed to provide initial conditions to swash zone models, but improvements in mechanistic modeling are needed to predict whether a beach will be eroded and overtopped, and the extent of flooding, especially when anthropogenic beach berms are used to strengthen coastal flood defenses.

This dissertation proposes a beach model based on vertically averaged, multi-phase flow

equations solved by a shock-capturing finite volume scheme. The model domain corresponds to the the so-called swash zone, the region between the shoreline and the inner surf zone where a layer-averaged model based on the assumption of hydrostatic pressure has been found to be a good approximation of system dynamics. Further offshore at intermediate to deep water depths, spectral wave models are routinely applied to describe wave transformations and output can be used as a boundary condition for the beach model.

The main contributions of this dissertation include new shock-capturing numerical methods for solving layer-averaged multi-phase flow equations, original experiments characterizing anthropogenic berm erosion and overtopping at field scale, and numerical modeling of beach and berm erosion aimed at measuring the predictive skill of the proposed model, developing an improved process understanding, and assessing strengths and weaknesses of the model.

Chapter 1

Introduction

1.1 Background and Motivation

Coastal areas are important habitats and contain large human populations [Nicholls, 2011], and people are increasingly migrating towards coastal cities [Hanson et al., 2011]. Hanson et al. [2011] report that 13 out of the 20 most populated cities in the world are port cities as of 2011. These trends raise serious concerns about the vulnerability of coastal communities to flooding. It is estimated that 20 million people reside along coasts below normal high tide levels, and over 200 million people are vulnerable to coastal flooding during storms [Nicholls, 2011].

There is an extensive and growing body of literature indicating that a combination of climate-induced sea level rise, storm surge, high tides, and waves will result in more frequent and damaging storms in coming decades [Nicholls, 2011, Tebaldi and Zervas, 2012]. California is among the most sensitive areas in the United States because of significant development within 1 m of present-day high tides [Strauss et al., 2012]. Based on sea level rise projections of $1 - 1.4$ meters by 2100 [Cayan and et.al., 2009], urbanized lowlands valued at over 100

billion dollars will be threatened [Heberger and et.al., 2009]. In many coastal cities in southern California, developed coastal lowlands are guarded from flooding by beaches and therefore beach erosion and overtopping from a combination of high tides and waves is a major concern [Schubert et al., 2014]. Furthermore, southern California beaches attract millions of visitors and tourists each year, so erosion represents a threat to local economies [Schubert et al., 2014].

Anthropogenic (artificial) berms/dunes are in use internationally to enhance the natural ability of beaches to withstand overtopping [Armaroli et al., 2012]. They are built on a seasonal basis or in anticipation of a hazardous event [Armaroli et al., 2012, Gallien et al., 2015]. In southern California, anthropogenic berms are used in beach cities like Venice Beach, Long Beach, Seal Beach and Newport Beach [Schubert et al., 2014, Gallien et al., 2015]. For example, berms used to protect Newport Beach, California are shown in Fig. 1.1. Newport Beach has experienced episodic dune overtopping and damaging flooding on numerous occasions[Gallien et al., 2011].

Figure 1.1: Temporary sand berm constructed at Newport Beach in 2010.

The growing threat of coastal flooding, and the vulnerability of coastal lowands protected by beaches, motivates improved management of beaches and improved tools for forecasting flood impacts so communities can take steps to mitigate impacts, including use of early warning systems and targeted flood preparedness campaigns [Harley and Ciavola, 2013]. In southern California, the Coastal Data Information Program (CDIP) provides a forecast of wave heights but presently does not offer a prediction of localized flooding that accounts for beach erosion[Gallien et al., 2013]. The fact is that such a prediction calls for a suite of models that account for tide and surge heights, wave heights, beach erosion and overtopping,

overland flow, and urban drainage; it is an ambitious task. This dissertation is focused on modeling some of the dynamics that occur on beaches as a result of wave uprush, downrush, and mobile sediment vulnerable to erosion and transport.

Empirical models have been developed to predict the overtopping volume associated with wave runup, which is important for coastal flooding [Van Der Meer and Janssen, 1995, Reis et al., 2008]. For example, with the aid of an empirical overtopping model, Gallien et al. [2014] were successful predicting urban flooding in Newport Beach caused by a long-period swell that occurred at a high tide. However, analysis of overtopping depends on the level of freeboard which varies as the beach is eroded by waves. Hence, empirical models are limited to instances where the beach profile can be assumed to be rigid. This limitation can be overcome with one of several types of numerical models that offer different strengths and weaknesses. Numerical methods can be classified into three main groups: Navier-Stokes equations, Boussinesq equations and Nonlinear Shallow Water Equations (NLSWE) (see Fig. 1.2).

Navier-Stokes models include those based on Reynolds Averaged Navier Stokes (RANS), and Large Eddie Simulation (LES). For instance, COBRAS (Cornell Breaking Waves and Structures) is a 2D Reynolds Averaged Navier-Stokes (RANS) approach and has been applied to regular wave overtopping of a porous structure [Liu et al., 1999]. Gotoh [Gotoh et al., 2004] has applied a Smooth Particle Hydrodynamics (SPH) with Large Eddy Simulation (LES) to study overtopping and non-overtopping conditions for partially submerged breakwater, but only a few seconds of 12,000 particle simulations were run. While full Navier-Stokes equations can model complicated hydrodynamics and resolve some limitations associated with breaking wave and wave structure simulations [Losada et al., 2008], they are still too computationally demanding for field scale simulation and practical problems.

Another approach is to solve Boussinesq equations, which are depth-integrated equations that retain the ability to account for wave dispersion caused by non-hydrostatic effects [Peregrine,

1967]. This approach is valid only where the ratio of the depth to deep water wave length is less than 0.2; and when nonlinearity and dispersion effects are of similar order [Abbott et al., 1978, Tonelli and Petti, 2009], so they are not good candidates for mid to inner surf zone modeling, where the nonlinearity is dominant.

A third approach is to solve non-linear shallow-water equations (NLSWE) with result from depth-averaging the Navier Stokes equations under the assumption of hydrostatic pressure. This approach is valid when the horizontal length scale dominates the vertical length scale; in other words, vertical velocity is neglected in comparison to horizontal velocity. The hydrostatic pressure distribution assumption may be violated when waves break, but NLSWEs have nevertheless been proven to offer a good approximation of flow near the shoreline (in the mid to inner surf zone) [Brocchini and Dodd, 2008]. Additionally, numerous models based on NLSWEs have been developed to predict overtopping of beaches and hardened coastal defenses [Hubbard and Dodd, 2002, Hu et al., 2000]. For instance, the shallow-water model AMAZON [Hu et al., 2000] has been successfully applied to simulate overtopping of coastal structures. Models based on NLSWE strike an attractive balance between computational cost and descriptive ability. Three dimensional models require an order of magnitude more computational cells to resolve the vertical dimension, roughly, and Boussinesq models require an order of magnitude smaller time step, roughly, for stability in the presence of high-order spatial derivatives that are used to model wave dispersion. Irrespective of the flow model formulation, an empirical law describing sediment entrainment must be used to simultaneously predict flow, sediment transport, and changes in sediment height and there are many ways to mix and match flow and sediment transport models Wu et al. [2002].

This dissertation is inspired by a class of models developed for debris flows characterized by hyperconcentrated levels of suspended sediment and rapid changes in sediment height. These so-called Debris Flow Models (DFMs) are derived by layer-averaging multi-phase flow equations under the assumption of hydrostatic pressure and instantaneous energetics sed-

iment transport models, and the governing equations are solved by shock-capturing finite volume schemes that do an excellent job of resolving sharp discontinuities in flow (e.g., hydraulic jumps) and sediment (e.g., step change in sediment height or concentration) [Capart and Young, 1998, Fraccarollo et al., 2003]. The swash zone is characterized by bores, transcritical flow, and wetting drying fronts that cycle repeatedly in a dynamic way and cause localized spikes in sediment concentration and transport [Hubbard and Dodd, 2002, Briganti and Dodd, 2009a,b, Brocchini and Baldock, 2008]. Hence, swash zone modeling appears to be an excellent application for DFMs yet this possibility has not been previously explored.

This dissertation presents improved numerical methods for solving layer-averaged models of flow, sediment transport, and bed change (Chapter 2), original experiments to study anthropogenic berm erosion in southern California (Chapter 3), and proposes a multi-phase shock-capturing (MPSC) model of swash zone dynamics to predict beach and berm erosion and possible overtopping during storm events (Chapter 4). Experimental data presented in Chapter 3 are used to evaluate the model presented in Chapter 4 based on numerical methods presented in Chapter 2. Chapter 2 and 3 were previously published as research papers and Chapter 4 was recently submitted to a journal for review and possible publication. This material was reformatted to meet university requirements, but the content is unchanged. Chapter 5 presents a 2D form of the MPSC model, and Chapter 6 presents conclusions. It is noted that the berm erosion experiments were a collaborative effort of several members of the Sanders Lab, including myself, and my leadership role was in the area of numerical model development which is the main focus of this dissertation.

To frame the practical goals of this dissertation, Fig. 1.2 shows where the proposed MPSC model is applied on a typical beach and how it can be coupled to an operational wave model such as Simulating Waves in the Nearshore (SWAN) [Booij et al., 1999]. SWAN predicts the transformation of the wave energy spectrum from an offshore location, where waves are measured by an operational buoy, into the nearshore accounting for the effect of variable

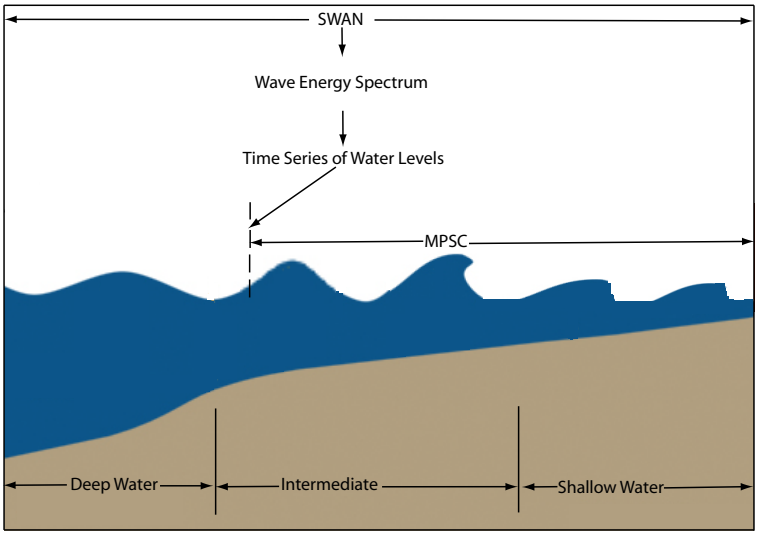

Figure 1.2: Range of applicability of numerical models.

bathymetry, wave breaking, bottom friction, and so on. At a point in the surf zone, the wave spectrum predicted by SWAN can be transformed into a stochastic time series representative of irregular wave action at that depth. In turn, this time series forces the MPSC model through its offshore boundary condition giving rise to swash zone predictions that vary in space and time. It is envisioned that with advances in remote sensing technologies, in the near future laser scanning of beaches will become common in advance of storms to check for vulnerabilities and to initialize predictive models. Hence, it is envisioned that the initial conditions required by the MPSC model will be obtained from laser scanning data and the boundary conditions will be obtained from SWAN predictions based on real-time wave data. The output of the MPSC model, in turn, can be used to predict coastal flooding using a model based on the shallow-water equations [Gallien et al., 2014]. Modeling systems of this type could offer coastal communities invaluable data regarding imminent flood impacts, helping to improve flood preparedness and response and thus minimize impacts.

Chapter 2

The LHLLC Scheme for Two-layer and Two-phase Flows on a Mobile Bed

This Chapter has been published in Advances Water Resources. Citation: Majd, M.S., and Sanders,B.F. (2014), The LHLLC scheme for Two-Layer and Two-Phase transcritical flows over a mobile bed with avalanching, wetting and drying, *Advances in Water Resources*, *67*, *16–31*, http://dx.doi.org/10.1016/j.advwatres.2014.02.002.

2.1 Introduction

Godunov-based models that solve a Riemann problem for flow and sediment fluxes under the assumption of a hydrostatic pressure distribution have been referred to as Debris Flow Models (DFMs) in numerous recent numerical modeling studies of hydromorphodynamics, e.g., [Fraccarollo and Capart, 2002, Fraccarollo et al., 2003, Rosatti and Fraccarollo, 2006, Armanini et al., 2009, Soares-Frazao and Zech, 2011]. DFMs form a hyperbolic system of conservation equations similar to the well-known shallow-water equations (SWEs), but include an additional transport equation for sediment and appropriate closures for turbulence and sediment mobility. Importantly, because the horizontal momentum balance is coupled to the sediment concentration, DFMs can be can be applied to hyper-concentrated flows including granular flows, mud flows and flows with discontinuities (shocks) in the flow and sediment heights [Capart and Young, 1998, Fraccarollo et al., 2003]. DFMs contrast with the Saint-Venant-Exner (SVE) approach whereby the fluid momentum balance assumes clean water, and thus the fluid momentum balance is decoupled from sediment concentrations [Goutire et al., 2008]. This limits the SVE approach to low sediment concentration regimes [Cao et al., 2002, Hudson and Sweby, 2003, Garegnani et al., 2012].

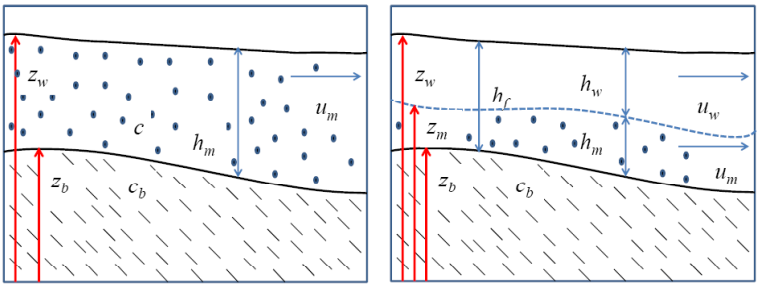

Figure 2.1: Left panel schematic sketch for Two-Phase approach, right panel schematic sketch for Two-Layer approach.

Alternative DFM formulations have been presented which differ in their assumption of layering. The *Two-Phase Approach* assumes a mobile, fluidized sediment mixture with a dynamic volumetric sediment concentration c, moving at a uniform velocity u_m, with a thickness h_m

and over an erodible sediment bed with an elevation of z_b, as shown in Fig. 2.1. [Rosatti and Fraccarollo, 2006, Cao et al., 2002, Wu and Wang, 2008, Rosatti et al., 2008, Armanini et al., 2009, Garegnani et al., 2012, Wu et al., 2002]. Defining the water surface elevation as $z_w = h_m + z_b$, this results in the following dependent variables which describe the flow Rosatti and Fraccarollo [2006],

$$V_{2\mathrm{P}} = (z_w \quad z_b \quad u_m \quad c) \tag{2.1}$$

Secondly, the *Two-Layer Approach* assumes two mobile layers above an erodible sediment bed including a sediment mixture layer of thickness h_m and velocity u_m, and a clear water layer with thickness h_w and velocity u_w. Numerous two-layer formulations appear in the literature with alternative approximations with respect to the vertical distribution of sediment concentration and horizontal velocity [Chen and Peng, 2006a, Chen et al., 2007, Zech et al., 2008, Spinewine and Zech, 2002, Zech et al., 2009], including 2D models with layer velocities that differ in both magnitude and direction [Swartenbroekx et al., 2013]. A common assumption is u_m=u_w [Fraccarollo et al., 2003, Spinewine and Zech, 2002], and defining $z_m = z_b + h_m$, the resulting dependent variables are [Fraccarollo et al., 2003],

$$V_{2\mathrm{L}} = (z_w \quad z_m \quad z_b \quad u_m) \tag{2.2}$$

DFMs clearly offer advantages over SVE approaches with the ability to resolve hyperconcentrated sediment flows, e.g., [Swartenbroekx et al., 2013], but little research has focused on the relative advantages and limitations of alternative DFM formulations. This information is valuable for assessing whether the uncertainty of unknown parameters and added computational demands of more complex models are overcome by improved predictive skill, an assessment that will surely depend on available site data and be influenced by numerous other factors such as computational resources.

This study focuses on Two-Phase and Two-Layer models that lead to four dependent vari-

ables defined by V_{2P} and V_{2L}, respectively. The former allows for a dynamically adjusting sediment concentration, and the latter for a dynamically adjusting sediment layer thickness of an assumed, constant, sediment concentration. Conceptually, the former matches the case where suspended load dominates the total sediment load, and the latter matches the case where bed load dominates the total load, but as will be shown later, the results of one can be recovered from the other for this special case where we assume $u_m = u_w$.

DFMs are cast in a form that is readily solved by Godunov-type finite volume methods (shock-capturing schemes), which have been proven robust for SWE applications such as dam-break, channel and overland flow problems with shocks [Fraccarollo and Capart, 2002, Fraccarollo et al., 2003]. However, the Riemann problem associated with the DFM is considerably more complex than for SWE [Fraccarollo and Capart, 2002], motivating numerous numerical modeling studies aimed at striking a good balance between stability, accuracy, and computational efficiency. Two widely used approximate Riemann solvers include the Harten, Lax and van Leer (HLL) scheme [Harten et al., 1983] and the Roe scheme [Roe, 1981], and both have been adapted for DFMs. Use of HLL has proven more common [Fraccarollo et al., 2003, Armanini et al., 2009, Chen et al., 2007, Chen and Peng, 2006a, Wu and Wang, 2008, Wu et al., 2002, Murillo and Garcia-Navarro, 2012], but there has also been work with the Roe solver [Rosatti et al., 2008, Rosatti and Begnudelli, 2010]. An appealing aspect of HLL-type approach [Harten et al., 1983, Fraccarollo and Toro, 1995] is that no special treatment (entropy fix) is needed to model critical flow points [Toro, 1992, Kuiry et al., 2011, Chen et al., 2007]. Godunov-type DFMs have also been extended to two dimensions to model more complex flow scenarios [Chen and Peng, 2006a, Armanini et al., 2009, Rosatti and Begnudelli, 2010, Wu et al., 2002, Murillo and Garcia-Navarro, 2012, Swartenbroekx et al., 2013].

The purpose of this paper is two-fold: (a) to present a common form of Two-Phase and Two-Layer DFMs in a unified way, with a consistent set of notation, to synthesize previous

Godunov-based DFM research and create a foundation for this and future studies aimed at developing improved computational models of shallow hydromorphodynamics, and (b) to present an improved computational scheme that is applicable to either the Two-Phase or Two-Layer DFM, as formulated here. The computational scheme is of the Godunov-type and builds on the LHLL model presented by Fraccarollo et al. [Fraccarollo et al., 2003], where the model name, LHLL=L+HLL, indicates use of *lateralization* (L) to discretize bottom slope terms in the momentum equation. LHLL is appealing because of its simplicity and efficiency, but it is overly diffusive with respect to sediment predictions **?**, and does not preserve stationary solutions involving wet/dry interfaces. The proposed scheme overcomes these limitations and is named LHLLC=L+HLL+C, where the L again indicates lateralization [Fraccarollo et al., 2003] and the C indicates use of the contact wave speed, in addition to gravity wave speeds, for the computation of sediment fluxes. Goutiere et al. [Goutire et al., 2008] successfully used a similar approach, i.e., HLL+C, for the SVE equations. Finally, the LHLLC model presented here incorporates an avalanching scheme that activates when slopes steepen beyond the angle of stability, and thus gravitational slumping occurs. Avalanching can be a significant contributor to sediment movement, such as head cut migration and the collapse of steep banks carved by incisive channel currents. Importantly, this form of transport cannot be described by a standard DFM model. The result of this paper is a unified presentation of basic Two-Phase and Two-Layer DFMs and an improved numerical solution scheme that enables less diffusive model predictions and applications to a wider range of test cases than previously possible.

The remainder of the paper continues as follows: Section 2 presents the governing equations for both Two-Phase and Two-Layer DFMs, and includes a characteristic analysis to show how the eigenvalues (i.e., wave speeds) are computed for each case, Section 3 presents the LHLLC scheme in a general way so as to solve either the Two-Phase or Two-Layer DFM, and Section 4 presents a range of test cases to measure the performance of the scheme, particularly in relation to the LHLL scheme. Comparisons between the Two-Layer and

Two-Phase LHLLC predictions are also shown to illustrate consistency. The paper closes with a discussion of results (Section 5) and conclusions (Section 6).

2.2 Governing equations

2.2.1 Sediment Mobility

Bagnold hypothesized that sediment movement or suspension dissipates energy [Bagnold, 1963, 1966], and numerous mathematical models based on energy principles have followed [de Groot, 2002]. Bailard [Bailard, 1981] used the fluid power per unit area P to scale the total load of sediment as follows,

$$P = \tau u_m \tag{2.3}$$

where τ is shear stress and u_m is fluid/sediment mixture velocity, as before. The shear stress between the mobile and fluidized sediment scales quadratically with velocity as follows Bailard [1981],

$$\tau = f \rho_w u_m^2 \tag{2.4}$$

where f is a dimensionless friction factor and ρ_w is the water density, so fluid power can be rewritten as,

$$P = f \rho_w u_m^3 \tag{2.5}$$

The total sediment load q_s in units of volume per unit width and time can be presented as [de Groot, 2002, Bailard, 1981],

$$q_s = (K_b + K_s)\frac{P}{(\rho_s - \rho_w)g} \tag{2.6}$$

where ρ_s represent the density for the solid phase, and K_b and K_s represent dimensionless, and potentially time-varying, scaling factors for bed-load and suspended-load, respectively. Substitution of Eq. 2.5 into Eq. 2.6 yields a well-known total load model for the rate of sediment transport that scales with the cubic of the mixture velocity,

$$q_s = (K_b + K_s)\frac{\rho_w f}{(\rho_s - \rho_w)g}u_m^3 \tag{2.7}$$

For two-phase DFMs, Eq. 2.7 has been further simplified as follows [Rosatti and Fraccarollo, 2006, Rosatti et al., 2008, Armanini et al., 2009],

$$q_s = cu_m h_m = c_b \beta u_m^3 \tag{2.8}$$

where c_b is the concentration by volume of the sediment in the bed and β is an empirical entrainment factor. Two-layer DFMs have employed a similar formula as follows [Fraccarollo et al., 2003],

$$q_s = u_m h_m = m u_m^3 \tag{2.9}$$

where m is an empirical mobility coefficient. Further, in the context of two-layer DFMs, the sediment concentration c_b has been termed a *granular packing* and referenced with different notation. However, here we adopt the notation of the Two-Phase model for consistency.

2.2.2 Two-Phase Model

The governing equations for the Two-Phase model are derived from continuity and momentum conservation laws for liquid and solid phases [Rosatti and Fraccarollo, 2006, Rosatti et al., 2008, Armanini et al., 2009]. A unified presentation of DFMs is given in differential form as follows,

$$\frac{\partial \mathbf{U}}{\partial t} + \frac{\partial \mathbf{F}}{\partial x} + \mathbf{H}\frac{\partial z_b}{\partial x} = \mathbf{S} \tag{2.10}$$

where

$$\mathbf{U} = \begin{pmatrix} h_m + z_b \\ c h_m + c_b z_b \\ (c\Delta + 1) u_m h_m \end{pmatrix}, \qquad \mathbf{F} = \begin{pmatrix} u_m h_m \\ c u_m h_m \\ (c\Delta + 1)(u_m^2 h_m + \frac{1}{2} g h_m^2) \end{pmatrix}$$

$$\mathbf{H} = \begin{pmatrix} 0 \\ 0 \\ (c\Delta + 1) g h_m \end{pmatrix}, \qquad \mathbf{S} = \begin{pmatrix} 0 \\ 0 \\ -f|u_m|u_m \end{pmatrix} \tag{2.11}$$

where $\Delta = (\rho_s - \rho_w)/\rho_w$. The first two equations in the above system account for mass conservation for the mixture and solid phase, respective, and the third equation is a momentum balance for the mixture. Note that the third term on the left-hand side of Eq. 2.10 accounts for bed slopes, and the right-hand side accounts for friction as given by Eq. 2.4. The total load sediment transport equation given by Eq. 2.8 represents the fourth equation of this system, allowing for prediction of $V_{2\mathrm{P}}$ as defined in Eq. 2.1.

Characteristic Analysis

Friction effects can be neglected when analyzing the instantaneous eigenstructure of the DFM, so we consider the homogeneous form of Eq. 2.10 given by,

$$\frac{\partial \mathbf{U}}{\partial t} + \frac{\partial \mathbf{F}}{\partial x} + \mathbf{H}\frac{\partial z_b}{\partial x} = 0 \tag{2.12}$$

and subsequently apply a transformation to place the above model in a quasi-linear form in terms of primitive variables as follows,

$$\mathbf{B}\frac{\partial \mathbf{W}}{\partial t} + \mathbf{A}\frac{\partial \mathbf{W}}{\partial x} = 0, \tag{2.13}$$

where

$$\mathbf{W} = \begin{pmatrix} h_m \\ u_m \\ z_b \end{pmatrix}, \quad \mathbf{B} = \begin{pmatrix} 1 & 0 & 1 \\ 0 & 2\beta c_b u_m & c_b \\ u_m & 3qu_m^2 + h_m & 0 \end{pmatrix} \tag{2.14}$$

$$\mathbf{A} = \begin{pmatrix} u_m & h_m & 0 \\ 0 & 3\beta c_b u_m^2 & 0 \\ \frac{1}{2}ru_m^2 + gh_m & (4qu_m^2 + rh_m)u_m & k \end{pmatrix} \tag{2.15}$$

and $k = gh_m(c\Delta + 1)$, $q = \beta c_b \Delta$, and $r = qg + 2$. Note that c does not appear in Eqs. 2.15 because it has been expressed in terms of u_m in accordance with Eq. 2.8. The eigenvalues of Eqs. 2.13 follow from the determinant of the coefficient matrices as follows,

$$|\mathbf{A} - \lambda \mathbf{B}| = 0 \tag{2.16}$$

which results in a cubic equation for eigenvalues,

$$\alpha_3 \lambda^3 + \alpha_2 \lambda^2 + \alpha_1 \lambda + \alpha_0 = 0 \tag{2.17}$$

$$\alpha_3 = h_m + u_m^2(2\beta + 3q), \tag{2.18}$$

$$\alpha_2 = -u_m^3(7q + 3\beta + r\beta) + 2\beta k u_m - h_m r u_m - 2\beta g h_m u_m, \tag{2.19}$$

$$\alpha_1 = -g h_m^2 + \frac{1}{2} u_m^2 [6\beta g h_m + r h_m - 10\beta k + u_m^2(3\beta r + 8q)], \tag{2.20}$$

$$\alpha_0 = 3\beta {u_m}^3 k, \tag{2.21}$$

The above equation yields three real and distinct roots (characteristic wave speeds) for which analytical solutions are not generally available [Fraccarollo and Capart, 2002, Fraccarollo et al., 2003], so the roots are calculated numerically using the solver presented in Section 2.3.1.

The characteristic wave speeds physically correspond to forward and backwards-moving gravity waves λ_1 and λ_3, respectively, and a contact wave speed λ_2 similar to other shallow flow and transport systems. However, unlike classical shallow-water equations wherein all characteristics take on the same sign in the limit of supercritical flow, there are always two roots with the same sign with this system, and one root with the opposite sign [Fraccarollo and Capart, 2002]. Hence, mathematically, information can propagate upstream against the flow when the Froude number, $Fr = u_m/(g h_m)^{1/2}$, exceeds unity.

2.2.3 Two-Layer Model

The governing equations for the Two-Layer model are similarly derived from continuity and momentum conservation laws for liquid and solid phases [Fraccarollo et al., 2003]. Using the general form given by Eqs. 2.10, and defining a total fluid layer thickness $h_f = h_w + h_m$, the

equations are defined by,

$$\mathbf{U} = \begin{pmatrix} h_f + z_b \\ h_m + z_b \\ u_m(h_f + \Delta' h_m) \end{pmatrix}, \qquad \mathbf{F} = \begin{pmatrix} u_m h_f \\ u_m h_m \\ (h_f + \Delta' h_m) u_m^2 + \frac{1}{2} g(h_f^2 + \Delta' h_m^2) \end{pmatrix}$$

$$\mathbf{H} = \begin{pmatrix} 0 \\ 0 \\ g(h_f + \Delta' h_m) \end{pmatrix}, \qquad \mathbf{S} = \begin{pmatrix} 0 \\ 0 \\ -f|u_m|u_m \end{pmatrix} \tag{2.22}$$

where $\Delta' = c_b \Delta$. The total load sediment transport equation given by Eq. 2.9 represents the fourth equation of this system, allowing for prediction of $V_{2\mathrm{L}}$ as defined in Eq. 2.2. The friction factor here is modeled by a friction angle φ as follows [Fraccarollo et al., 2003],

$$f = g c_b \Delta \tan \varphi \tag{2.23}$$

and the mobility parameter m in Eq. 2.9 is expressed by entrainment coefficent C_f as follows [Fraccarollo et al., 2003],

$$m = (1 + \Delta) C_f / f \tag{2.24}$$

As a brief aside, it is noteworthy that Two-Layer model solutions can be recovered from Two-Phase model solutions (and vice-versa), assuming the same friction and sediment mobility closure models are used. The conversion is achieved from the following identity,

$$(h_m)_{2L} = (c h_m / c_b)_{2P} \tag{2.25}$$

where the subscripts $2L$ and $2P$ refer to Two-Layer and Two-Phase, respectively.

Characteristic Analysis

When the two-layer model is presented in the quasi-linear form given by Eqs. 2.13, it can be presented as follows,

$$\mathbf{W} = \begin{pmatrix} h_f \\ u_m \\ z_b \end{pmatrix}, \quad \mathbf{B} = \begin{pmatrix} 1 & 0 & 1 \\ 0 & 2mu_m & 1 \\ u_m & h_f + 3\Delta' h_m & 0 \end{pmatrix}$$

$$\mathbf{A} = \begin{pmatrix} u_m & h_f & 0 \\ 0 & 3h_m & 0 \\ u_m^2 + gh_f & 2[h_f + (2 + gm)\Delta' h_m]u_m & g(h_f + \Delta' h_m) \end{pmatrix} \tag{2.26}$$

and when the eigenvalues are computed using Eq. 2.16, a cubic equation for the roots is again obtained (Eq.2.17) with the following coefficients,

$$\alpha_3 = h_f + (2 + 3\Delta')h_m, \tag{2.27}$$

$$\alpha_2 = -[2h_f + (5 + 7\Delta')h_m]u_m, \tag{2.28}$$

$$\alpha_1 = [h_f + (3 + 4\Delta')h_m]u_m^2 - g(h_f^2 + 2h_m h_f + 3\Delta' h_m^2), \tag{2.29}$$

$$\alpha_0 = 3(h_f + \Delta' h_m)gh_m u_m, \tag{2.30}$$

As before, the roots correspond to two gravity waves and one contact wave and are computed numerically using the scheme presented in Section 2.3.1. In this case, $Fr = u_m/(gh_f)^{1/2}$.

2.3 Numerical Methods

2.3.1 Cubic Equation Solver

DFMs give rise to cubic equations for the eigenvalues and also for updating the flow velocity, u_m, as will be shown later. A general form of the cubic equation is as follows,

$$a_3X^3 + a_2X^2 + a_1X + a_0 = 0 \tag{2.31}$$

and its roots are given by [M. R. Spiegel, 1999, Fraccarollo et al., 2003],

$$X_j = 2\sqrt{Q}cos(\Phi_j) - \frac{a_2}{3a_3} \tag{2.32}$$

where j=1,2 or 3,

$$\Phi_1 = \frac{\theta}{3} + \frac{2\Pi}{3}, \qquad \Phi_2 = \frac{\theta}{3} + \frac{4\Pi}{3}, \qquad \Phi_3 = \frac{\theta}{3} \tag{2.33}$$

and

$$\theta = \arccos(\frac{R}{Q^{3/2}}), \quad Q = \frac{a_2^2 - 3a_3a_1}{9a_3^2}, \quad R = \frac{9a_3a_2a_1 - 27a_3^2a_0 - 2a_2^3}{54a_3^3} \tag{2.34}$$

2.3.2 LHLLC scheme

The LHLLC scheme is presented here as a solver of the general DFM form given by Eqs. 2.10, so the solution vector **U**, fluxes **F**, the bed-slope pressure flux term **H**, and the bed friction term **S** are also referenced in a general way as follows,

$$\mathbf{U} = \begin{pmatrix} U_1 \\ U_2 \\ U_3 \end{pmatrix}, \qquad \mathbf{F} = \begin{pmatrix} F_1 \\ F_2 \\ F_3 \end{pmatrix}, \qquad \mathbf{H} = \begin{pmatrix} 0 \\ 0 \\ H_3 \end{pmatrix}, \qquad \mathbf{S} = \begin{pmatrix} 0 \\ 0 \\ S_3 \end{pmatrix} \tag{2.35}$$

This general approach is chosen to facilitate application of the scheme to either Two-Layer or Two-Phase DFM formulations, and to more easily adapt to alternative closure and entrainment schemes.

The domain is discretized into N cells and the solution is assumed to be piecewise constant with states $\mathbf{U}_i$, for $i = 1, \ldots, N$, and inter-cell interferes located at $x_{i+1/2}$, $i = 0, \ldots, N$. Following Fraccarollo et al. [Fraccarollo et al., 2003], the fluid mixture continuity equation is updated as follows,

$$(U_1)_i^{n+1} = (U_1)_i^n + \frac{\Delta t}{\Delta x}\left[(F_1)_{i-1/2}^* - (F_1)_{i+1/2}^*\right] \tag{2.36}$$

where $(F_1)_{i+1/2}^*$ represents fluxes computed with the HLL scheme as follows,

$$(F_1)^* = \frac{S_R F_{1L} - S_L F_{1R} + S_R S_L (U_{1R} - U_{1L})}{S_R - S_L} \tag{2.37}$$

where S indicates wave speeds and the subscripts L and R represents the cells to the left i and right $i+1$, respectively. Various choices are available to estimate the wave speeds S_L, S_R Toro [1997], and the following was used here [Fraccarollo et al., 2003].

$$S_L = \min(\lambda_{1L}, \lambda_{1R}) \tag{2.38}$$

$$S_R = \max(\lambda_{3L}, \lambda_{3R}) \tag{2.39}$$

where λ_1 and λ_3 represent maximum and minimum characteristic wave speeds, respectively [Fraccarollo et al., 2003].

Next, the sediment continuity equation is updated as follows,

$$(U_2)_i^{n+1} = (U_2)_i^n + \frac{\Delta t}{\Delta x}\left[(F_2)_{i-1/2}^* - (F_2)_{i+1/2}^*\right] \tag{2.40}$$

where the fluxes are computed using an HLLC scheme similar to [Goutire et al., 2008]. When $(F_1)^* \geq 0$, flow is in the positive x direction and the solid flux is computed as follows,

$$(F_2)^* = \frac{S_S F_{2L} - S_L F_{2R} + S_S S_L (U_{2R} - U_{2L})}{S_S - S_L} \tag{2.41}$$

where S_L is computed as before and S_S is computed from the speed of contact discontinuities (λ_2) in neighboring cells as follows,

$$S_S = \text{maxmod}(\lambda_{2L}, \lambda_{2R}) \tag{2.42}$$

where the function maxmod() returns the signed argument with the largest absolute value. On the other hand, when $(F_1)^* < 0$, the solid flux is computed as follows for directional symmetry,

$$(F_2)^* = \frac{S_R F_{2L} - S_S F_{2R} + S_R S_S (U_{2R} - U_{2L})}{S_R - S_S} \tag{2.43}$$

where S_S and S_R are computed as before.

Before the solid flux is used to update Eq. 2.40, a limiting function is applied to prevent the magnitude of the solid flux F_2^* from exceeding the magnitude of the total fluid mixture flux F_1^*, as this would give non-physical predictions. The limiting is expressed as follows,

$$(F_2)^*_{i+1/2} = \text{maxmod}[(F_1)^*_{i+1/2}, (F_2)^*_{i+1/2}] \tag{2.44}$$

Finally, the momentum equation is updated using the LHLL scheme in a two-step process as follows [Fraccarollo et al., 2003],

$$(U_3)^*_i = (U_3)^n_i + \frac{\Delta t}{\Delta x}\left[(F_3)^{*R}_{i-1/2} - (F_3)^{*L}_{i+1/2}\right] \tag{2.45}$$

$$(U_3)^{n+1}_i = (U_3)^*_i + \Delta t (S_3)^{n+1}_i \tag{2.46}$$

where the superscripts L and R represent adjustments to the fluxes F_3 that account for bed slope effects expressed by the H_3 term in Eq. 2.22. The first step begins with the application of an HLL scheme to compute F_3^* as follows,

$$(F_3)^* = \frac{S_R F_{3L} - S_L F_{3R} + S_R S_L (U_{3R} - U_{3L})}{S_R - S_L} \tag{2.47}$$

where S_L and S_R are computed as before. Next, lateralization terms are computed for the left L and right R side of each cell interface as follows,

$$\delta_{L,R} = \frac{S_{L,R}}{S_R - S_L} \frac{1}{2} (H_{3L} + H_{3R}) (z_{bR} - z_{bL}) \tag{2.48}$$

and the required fluxes for Eq. 4.15 are given by,

$$(F_3)^{*L} = (F_3)^* - \delta_L \qquad (F_3)^{*R} = (F_3)^* - \delta_R \tag{2.49}$$

The second step of the momentum update, Eq. 2.46, involves the solution of a cubic equation for u_m, that follows from the implicit formulation of the update equation. The cubic equation and final update procedure for U_3 depends on the type of DFM and the chosen closure scheme. The procedure for the Two-Phase and Two-Layer formulations presented here is shown next.

Two-Phase Model

Eq. 2.46 is expanded as follows in accordance with the Two-Phase formulation,

$$(c\Delta + 1) u_m h_m = U_3^* - \Delta t f |u_m| u_m \tag{2.50}$$

where the subscript i and superscript $n+1$ have been dropped to simplify the presentation, and U_3^* represents the update given by Eq. 4.15. Based on the definition of U_1 given by

Eq. 2.11, it follows that,

$$z_b = U_1 - h_m \tag{2.51}$$

Additionally, from Eq. 2.8 it follows that,

$$ch_m = c_b \beta u_m^2 \tag{2.52}$$

so substituting Eq. 2.51 and 2.52 into the expression for U_2 given by Eq. 2.11 leads to the following expression for h_m,

$$h_m = \beta u_m^2 + U_1 - U_2/c_b \tag{2.53}$$

Finally, substitution of Eq. 2.52 and Eq. 2.53 into Eq. 2.50 gives a cubic equation with only one unknown, u_m, as follows,

$$(1 + c_b\Delta)\beta u_m^3 + (U_1 - U_2/c_b)u_m = U_3^* - \Delta t f |u_m| u_m \tag{2.54}$$

which is solved using the method described in Section 2.3.1. Note that U_1, U_2 and U_3^* are computed using Eqs. 2.36, 2.40 and 4.15, respectively. After u_m is computed, h_m and z_b are sequentially computed using Eqs. 2.53 and 2.51, respectively, c is computed from Eq. 2.52, and U_3 is computed as,

$$U_3 = (c\Delta + 1)u_m h_m \tag{2.55}$$

which finalizes the update of conservative variables $\mathbf{U}^{n+1}$ and primitive variables c^{n+1}, h_m^{n+1}, u_m^{n+1} and z_b^{n+1} with respect to the DFM given by Eqs. 2.11.

Two-Layer Model

Eq. 2.46 is expanded as follows in accordance with the Two-Layer formulation,

$$u_m(h_f + \Delta' h_m) = U_3^* - \Delta t f |u_m| u_m \tag{2.56}$$

where the subscript i and superscript $n+1$ have been dropped to simplify the presentation, and U_3^* represents the update given by Eq. 4.15. Based on the definition of $\mathbf{U}$ given by Eq. 2.22, if follows that,

$$h_f = U_1 - U_2 + h_m \tag{2.57}$$

Additionally, from Eq. 2.9 it follows that,

$$h_m = m u_m^2 \tag{2.58}$$

so substituting Eq. 2.57 and 2.58 into Eq. 2.56 leads to a cubic equation with only one unknown, u_m, as follows,

$$(1 + \Delta')m u_m^3 + (U_1 - U_2) u_m = U_3^* - \Delta t f |u_m| u_m \tag{2.59}$$

which is also solved using the method described in Section 2.3.1. Note that U_1, U_2 and U_3^* are computed using Eqs. 2.36, 2.40 and 4.15, respectively. After u_m is computed, h_f and h_m are computed using Eqs. 2.57 and 2.58, respectively, U_3 is computed as,

$$U_3 = u_m(h_f + \Delta' h_m) \tag{2.60}$$

and z_b is computed as

$$z_b = U_1 - h_f \tag{2.61}$$

which finalizes the update of conservative variables $\mathbf{U}^{n+1}$ and primitive variables h_f^{n+1}, h_m^{n+1}, u_m^{n+1} and z_b^{n+1} with respect to the DFM given by Eqs. 2.22.

2.3.3 Wet/Dry Scheme

DFMs are designed to systematically model the dynamics of coupled fluid/sediment motion and thus handle wetting and drying fronts without any special numerical fixes. However, exceptions have previously been reported in the literature [Goutire et al., 2008], namely sediment motion on sloping topography in the absence of any fluid motion. Preliminary testing by the authors revealed that non-physical motion also occurred when a horizontal water surface intersected a sloping ground surface, creating a wet/dry interface as in a beach or the bank of a river. Consequently, the numerical scheme presented here includes a check for this condition and a minor modification of the flux calculation to enforce a reflection which preserves stationary solutions at wet/dry interfaces.

Consider the case where the mixture surface elevation in the cell on the left, $(z_w)_L$, is below the bed elevation of a cell on the right that is dry, $(z_b)_R$, i.e., $(z_w)_L < (z_b)_R$ and $(h_m)_R < \epsilon_h$ where ϵ_h represents a wet/dry tolerance. If this occurs, then $\mathbf{F}^*$ is given by,

$$\mathbf{F}^* = \begin{pmatrix} 0 \\ 0 \\ F_{3L} - S_L U_{3L} \end{pmatrix} \tag{2.62}$$

and the lateralization terms are given by,

$$\delta_L = 0, \qquad \delta_R = F_{3L} - S_L U_{3L} \tag{2.63}$$

Conversely, in the case where $(z_w)_R < (z_b)_L$ and $(h_m)_L < \epsilon_h$,

$$\mathbf{F}^* = \begin{pmatrix} 0 \\ 0 \\ F_{3R} - S_R U_{3R} \end{pmatrix} \tag{2.64}$$

and the lateralization terms are given by,

$$\delta_L = F_{3R} - S_R U_{3R}, \qquad \delta_R = 0 \tag{2.65}$$

It is noted that stable and accurate results have been obtained using a wide range of small values for ϵ_h, from microns to millimeters. A value of 1 mm comparable to the diameter of a sand grain is used for this study. In general, the parameter should be set significantly smaller than the minimum depth that the model is intended to resolve.

2.3.4 Avalanching Scheme

Avalanching in this context refers to a numerical process by which sediment on unstable slopes is redistributed into a stable distribution, as if the sediment moved under the influence of gravity similar to a real avalanche. This process of interest here is one that begins with sub aqueous (wet) erosion of a slope, and subsequently propagates into the subaerial (dry) sediments [Swartenbroekx et al., 2010b, van Rijn, 2009, Nagata et al., 2000]. For example, river bank erosion is commonly caused by hydrodynamic erosion at the toe, which steepens the bank and causes slumping (avalanching) of the subaerial soil.

In the model, a critical slope S_c is defined and the avalanching scheme engages when the magnitude of sediment slopes S computed by the model from bed elevation data exceed the critical slope, i.e., $|S| > S_c$. Separate "dry" and "wet" critical slopes are used, S_c^{dry} and S_c^{wet}, to account for the difference in the angle of repose beween subaerial and subaqueous sediments, respectively.

The avalanching scheme involves two main steps. In the first step, the slope is computed for each cell interface as follows,

$$S_{j+1/2} = \frac{(z_b)_{j+1} - (z_b)_j}{\Delta x} \tag{2.66}$$

and then the slope exceedance is also computed,

$$\Delta S_{j+1/2} = \begin{cases} |S_{j+1/2}| - (S_c)_{j+1/2} & \text{if} \quad |S_{j+1/2}| > (S_c)_{j+1/2} \\ 0 & \text{if} \quad |S_{j+1/2}| \leq (S_c)_{j+1/2} \end{cases} \tag{2.67}$$

In the second step, bed elevation is updated as follows,

$$(z_b)_j = (z_b)_j + \alpha \left[(\Delta z_b)^R_{j-1/2} + (\Delta z_b)^L_{j+1/2} \right] \tag{2.68}$$

where α is the under-relaxation factor required to be between zero and unity Roelvink et al. [2009], Sanchez and Wu [2011] and set here to 0.95 and

$$(\Delta z_b)^L_{j+1/2} = +\frac{\alpha}{2}\, s_{j+1/2} \Delta S_{j+1/2} \Delta x \tag{2.69}$$

$$(\Delta z_b)^R_{j+1/2} = -\frac{\alpha}{2}\, s_{j+1/2} \Delta S_{j+1/2} \Delta x \tag{2.70}$$

where $s_{j+1/2} = \text{sign}(S_{j+1/2})$.

The preceding steps given by Eqs. 2.66-2.70 are repeated, without any changes to flow parameters, until the process brings the overly steep slopes in line with the critical slopes, as if an avalanche were to occur on a time scale faster than the hydromorphodynamic change resolved by the DFM. Since the adjustment process tapers off over time and the adjusted slopes slowly converge upon the critical slopes, the iteration process is stopped when slopes are within 10% of the critical slope. It is noted that avalanching may not necessarily proceed

faster than the hydromorhodynamics resolved by the DFM, in which case a mechanistic avalanching scheme may be required.

One key feature of the above scheme is that the first step (slope calculation) is completed for all cells before the second step (bed update) begins. This eliminates the directional bias associated with schemes that compute slopes and update the bed height on a cell-by-cell basis, e.g., [Wu, 2007].

After the avalanching scheme converges, U_1^{n+1} and U_2^{n+1} are updated to account for changes in z_b. Defining $(\Delta z_b)_j^a$ to be the overall change in $(z_b)_j$ after all iterations of the avalanching scheme, U_1 is updated as follows,

$$(U_1)_j^{n+1} = (U_1)_j^{n+1} + (\Delta z_b)_j^a \tag{2.71}$$

The update of U_2 depends on whether it is a Two-Phase or Two-Layer model. For the Two-Phase model,

$$(U_2)_j^{n+1} = (U_2)_j^{n+1} + c_b(\Delta z_b)_j^a \tag{2.72}$$

while for the Two-Layer model,

$$(U_2)_j^{n+1} = (U_2)_j^{n+1} + (\Delta z_b)_j^a \tag{2.73}$$

2.3.5 Summary of Solution Procedure and Error Metric

To summarize, the LHLLC scheme advances the solution with a repeating cycle of: (1) computation of fluxes, (2) updating of solution in accordance with the DFM, (3) updating of the bed in accordance with the avalanching algorithm (when critical slopes are exceeded), and (4) the final updating of the solution vector $\mathbf{U}$.

To quantify model errors in an arbitrary primitive variable v, in the test problems that follow, an L_1 norm is used. This computes the difference between a discrete model prediction v_i and a reference solution $\hat{v}_i$ as follows,

$$L_1(v, \hat{v}) = \frac{1}{N} \sum_{i=1,N} |v_i - \hat{v}_i| \tag{2.74}$$

2.4 Results

A series of test cases are considered to critically examine the LHLLC scheme, including test problems with exact solutions and experimental data from laboratory studies of hydromorphodynamics. Wherever possible, the LHLLC predictions are compared against LHLL predictions to illuminate the benefits arising from explicit consideration of contact discontinuity wave speeds and to test for drawbacks or advantages from the wet/dry scheme. Additionally, test cases involving steep slopes are included to examine the avalanching model.

2.4.1 Stationarity Test

First, the ability of the LHLL and LHLLC scheme to preserve a stationary solution is examined using the Two-Phase DFM formulation. The two schemes are applied to a domain characterized by $x \in (-L,\ L)$, with L=100 m, that is configured similar to the cross-section of a trapezoidal channel with levees as shown in Fig. 2. The central part of the domain has a horizontal bottom elevation with $z_b = 0$, and the channel banks rise with a 1:2 slope from toe locations of $x = \pm 70$ m to a height of 2.5 m which represents the crest of the levee. Outside the crest of the levee, z_b slopes 1:5 downward away from the central portion of the channel and then levels off at an elevation of 1.5 m. The initial condition corresponds to the channel filled to an initial water surface elevation of 1 m and the initial fluid velocity is zero. The solution is integrated for 60 s using a Courant number of 0.95 and a grid resolution of Δx=1 m. β is set to 10^{-4}, c_b is set to 0.55 and f is set to 0.012. For this test case, the avalanching scheme is not activated so no movement of either fluid or sediment should occur.

Fig. 2.2 presents LHLL and LHLLC predictions of the water surface and bed profile with and without the wet/dry scheme activitated. The bottom, right hand panel shows the solution after 60 s with the wet/dry scheme activated, which is unchanged from the initial condition

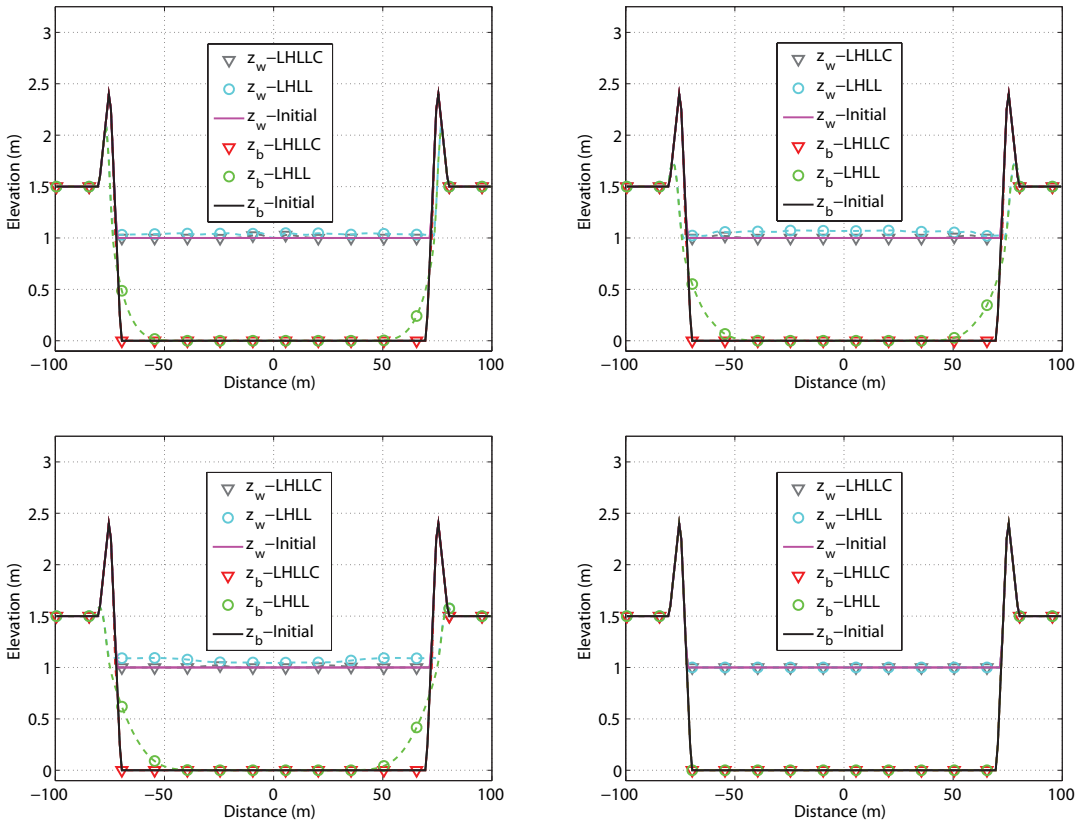

Figure 2.2: Numerical to solution to water-at-rest problem. Left-Top: wet/dry fix not used-at 20 s; Right-Top: wet/dry fix not used-at 40 s; Left-Bottom: wet/dry fix not used-at 60 s ; Right-Bottom: wet/dry fix used-at 60 s.

using either LHLL or LHLLC indicating that both schemes preserve stationarity. At the end of the run, the maximum velocity was measured to be $O(10^{-8})$ m/s in both cases. The other three panels show the solution at 20, 40 and 60 s without the wet/dry scheme activated. In this case, neither scheme preserves stationarity. The LHLL scheme predicts significant diffusion of the bed profile, as well as wave action on the water surface. The LHLLC predictions are considerably less diffusive, but do not preserve stationarity exactly.

2.4.2 Avalanching Test

The avalanching scheme is designed to take an overly steep slope, one that exceeds the critical slope of stability, and to redistribute sediment in the down-slope direction until the

slope is stabilized. To verify that the avalanching scheme performs as desired, a test case with a triangular berm 2 m high and 5 m wide is considered on a spatial domain $x \in (0,\ L)$ with L=20 m, which is discretized by Δx=0.1 m. The berm slopes are assumed to be at the angle of repose of the sediment, so berm slopes of 1:1.25 represent the critical slope S_c. Next, the left and right toe of the berm are "eroded" by setting $(z_b)_j = 0$ at the first elevated vertex on the left side of the berm and the last 14 elevated vertices on the right side of the berm. This is taken as an initial condition for the avalanching routine. Fig. 2.3

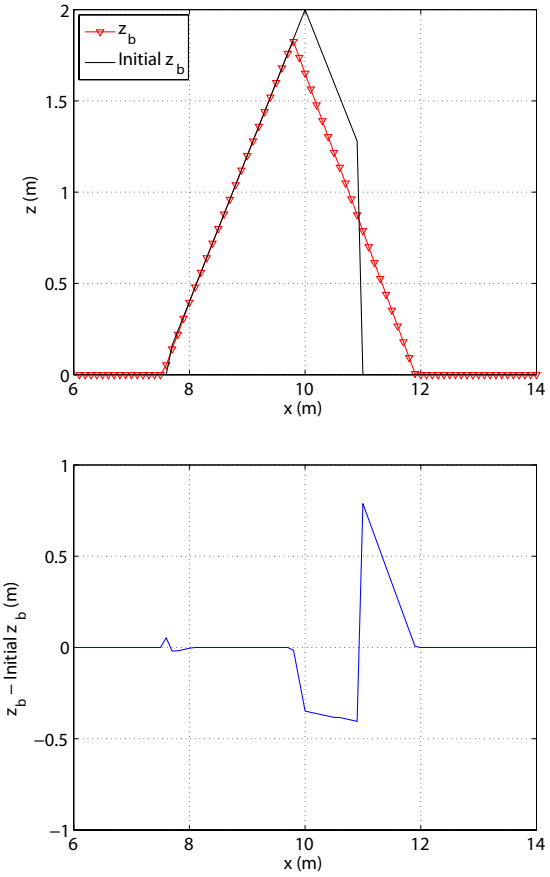

Figure 2.3: Top panel: initial and final z_b profile after adjustment by the avalanching scheme; bottom panel: difference between initial and final profile, showing redistribution of sediment.

presents the initial z_b profile and final profile predicted by the avalanching scheme. On the left side of the berm, the final profile tracks the initial profile very closely except at the toe, where sediment has filled in to achieve a uniform slope. This is indicated by the small bump in the bottom panel of Fig. 2.3 (left side of berm). On the right side, the final profile

Table 2.1: Values of parameters for trench evolution tests

Parameter	Description	Unit	Subcritical	Supercritical
Fr	Froude number	-	0.85	1.2
f	Friction parameter	-	0.012	0.01
β	Erosion parameter	-	3.5×10^{-4}	1×10^{-3}
ρ_s/ρ	Sediment relative density	-	1.580	1.580
c_b	Bed packing parameter	-	0.65	0.65
Δx	Grid resolution	m	0.05	0.05
-	Courant number	-	0.95	0.95
-	Bed slope	-	8.83×10^{-3}	1.57×10^{-2}
-	Initial depth	m	2	2
-	Initial velocity	m/s	3.76	5.31
-	Length of the trench	m	2	2
-	Depth of the trench	m	0.6	0.9

is markedly different from the initial profile since a much larger volume of sediment from the upper berm was moved downwards to equilibrate the slope at the angle of repose. The scheme converges to the critical slope after 198 iterations, and conserves mass to numerical precision. Importantly, the scheme is shown to account for both large (right side o berm) and small (left side) amounts of sediment movement.

2.4.3 Trench Test

Flow across a submerged trench has previously been used to qualitatively evaluate DFM performance [Rosatti and Fraccarollo, 2006, Rosatti et al., 2008] and is revisited here to characterize the relative amount of numerical diffusion between the LHLL and LHLLC models. As before, the models are applied to the Two-Phase DFM and test parameters shown in Table 2.1. Fig. 2.4 shows LHLL and LHLLC predictions of the z_b profile at t=60 s under subcritical flow conditions ($Fr < 1$). This shows that the LHLL scheme is overly diffusive as has been shown in previous studies [Rosatti and Fraccarollo, 2006]. On the other hand, the LHLLC scheme predicts sharp z_b fronts indicating that the scheme is much less diffusive.

Fig. 2.5 shows a similar comparison of LHLL and LHLLC under supercritical conditions ($Fr > 1$), using parameters shown in Table 1. In this case, the trench is quickly filled with

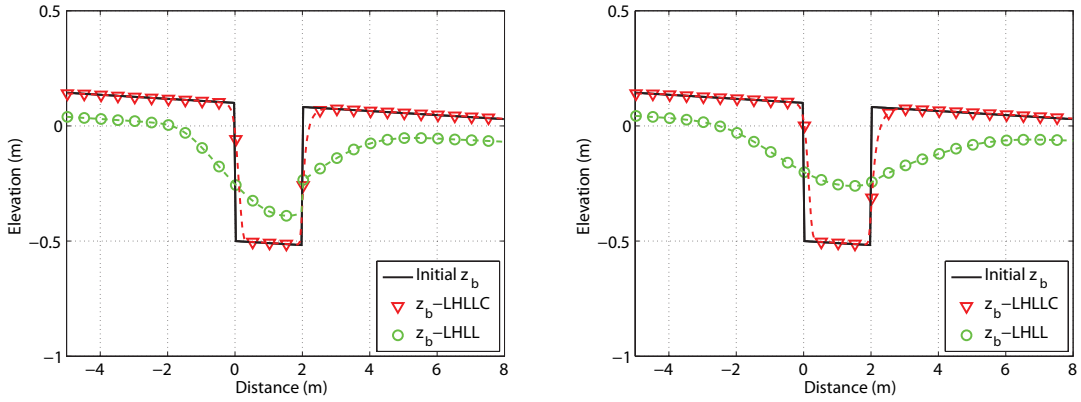

Figure 2.4: Evolution of a trench predicted by LHLL and LHLLC schemes under sub-critical flow conditions; left panel shows the results at 30 s and right panel at 60 s; spatial resolution 0.05 m and Courant number 0.95.

sediment and sediment depression waves are predicted to move away from the initial trench position. One depression wave is regressive, moving against the flow, and one depression wave is progressive, moving with the flow. This movement may seem peculiar at first because traditional notions of supercritical flow imply that all information moves in the downstream flow direction. However, the eigenstructure of the governing equations shown in Section 2.2.2 indicates one regressive and two progressive waves under both sub-critical and super-critical conditions, and this explains the upward moving sediment wave. Physically, the regressive depression wave is moving to supply the sediment required to fill the trench.

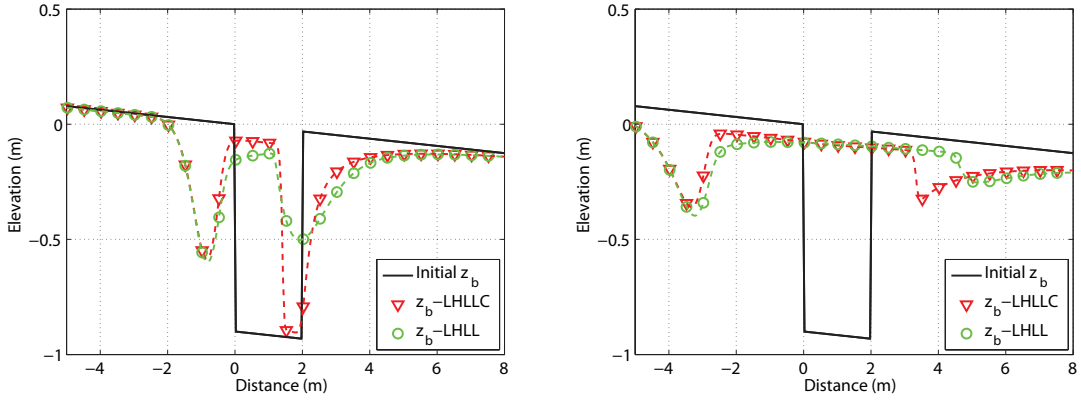

Figure 2.5: Evolution of a trench predicted by LHLL and LHLLC schemes under super-critical flow conditions; left panel shows the results at 10 s and right panel at 30 s; spatial resolution 0.05 m and Courant number 0.95.

Fig. 2.5. also shows that the LHLLC scheme is again less diffusive than the LHLL scheme, although the differences are not as prominent as in the sub-critical test case. Another key difference is that the LHLL scheme predicts a faster progressive wave than the LHLLC scheme, presumably because the LHLL scheme uses gravity wave speeds to predict sediment fluxes, whereas the LHLLC scheme considers the contact wave speed which is slower.

2.4.4 Classical Dam-Break Test

A classical dam-break test, with water at rest in reservoir and a dry downstream channel bed, is presented here to compare and contrast the mobile and immobile bed solutions. Table 2.2 shows the initial condition and parameters used for testing.

Table 2.2: Initial condition and model parameter for dam-break test

	Water depth (m)	Velocity (m/s)	Bed elevation (m)	c_b -	ρ_s/ρ -	β Mobile-Bed	f Mobile-Bed	β Fixed-Bed	f Fixed-Bed
Left	0.1	0.0	0.0	0.5	1.048	0.125	1×10^{-4}	1.25×10^{-8}	0.0
Right	0.0	0.0	0.0	0.5	1.048	0.125	1×10^{-4}	1.25×10^{-8}	0.0

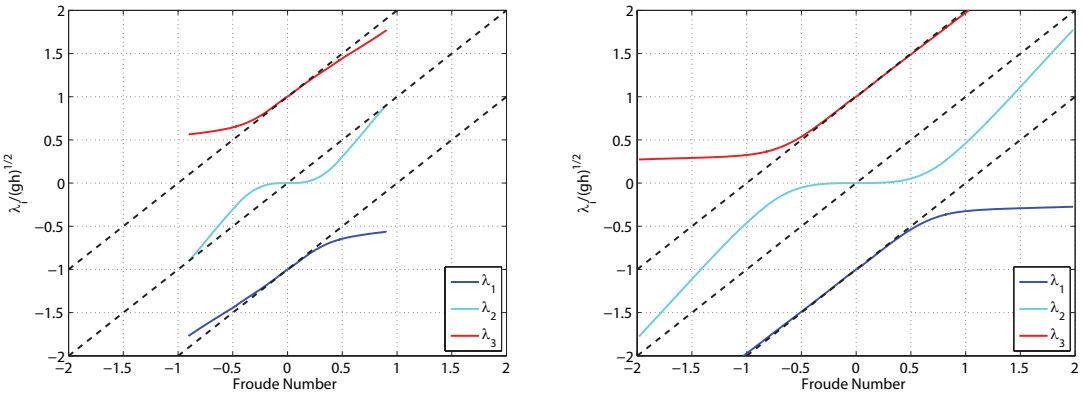

Figure 2.6: Characteristic wave speeds λ_1 λ_2 and λ_3. Left panel β is set to 0.125 and right panel β is set to 0.0125. Dashed lines represent wave speeds for immobile bed scenario, and colored lines represent mobile bed wave speeds computed using Eq. 2.17

.

The eigenvalues for this test problem are shown in Fig. 2.6, and and also for a second value of β to illustrate parameter sensitivity. Here, dashed lines represent the wave speeds under

immobile bed (clear water) conditions, and solid curves represent the DFM wave speeds. It can be seen that DFM theory dictates that there are always two down-stream moving waves and one up-stream moving wave, irrespective of Fr, in contrast to the case of an immobile bed theory where the possibility exists that all three eigenvalues take on the same sign. Also note that the λ_2 values are very close to zero for $0.2 < Fr < 0.2$ (approximately) and generally equal or smaller than predicted by immobile bed theory, indicating that flows are effectively slowed down in comparison to sediment-free flows under subcritical conditions. This emphasizes the potential significance of using the contact wave speed, λ_2, in sediment flux calculations.

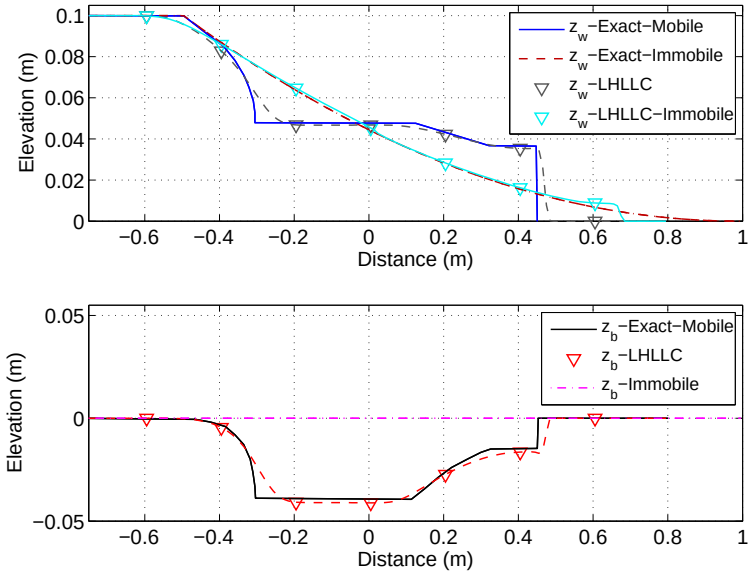

Figure 2.7: Mobile and immobile bed dam-break predictions by LHLLC scheme.

The Two-Phase DFM is solved with the LHLLC scheme using $\Delta x = 0.01$ m and integrated using $Cr = 0.95$, and Fig. 2.7 shows the free surface and bed profile at 0.5 s for the mobile and immobile bed scenarios. The LHLLC exhibits modest numerical diffusion as expected, particularly at the leading edge of the regressive depression wave,, but the scheme correctly predicts key attributes of the solution such as the depth and width of the erosion. As previously noted, the progressive wave is slowed down by the mobile sediment. This has practical implications, because a slower progressive wave affects the available time to evacuate

in the event of a dam failure.

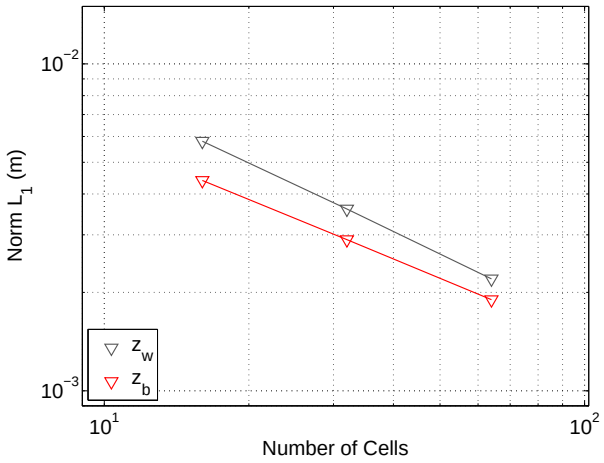

Figure 2.8: LHLLC scheme errors in the mobile dam-break probelm are shown to geometrically decay with grid refinement.

The preceding mobile-bed test case was repeated using Δx=0.1, 0.05, and 0.025 m and $Cr = 0.95$ to verify that the LHLLC scheme converges with grid refinement. Fig. 2.8 shows that errors (L_1 norms) are geometrically reduced with refinement, and thus the scheme is shown to converge in a classical sense.

2.4.5 Multiple Discontinuity Tests

Two additional dam-break test problems with multiple discontinuities, i.e., bed height and water height, are now considered to compare the LHLLC and LHLL schemes, quantitatively. Similar problems were considered by [Rosatti and Fraccarollo, 2006, Rosatti et al., 2008] for DFM research. Once again, the Two-Phase DFM is solved. Scenario parameters are shown in Table 2.3. Test A is a flow problem with three waves from left to right as follows: a regressive rarefaction wave, a progressive shock wave (discontinuity in z_b), and a progressive rarefaction wave. Test B is also a flow problem with three waves as follows: a regressive rarefaction, a progressive rarefaction and a shock. The LHLLC and LHLL schemes are both applied using Δx=0.1 m and integrated using Cr=0.95. Mass balance errors are computed

Table 2.3: Initial condition and model parameter for tests A and B

		Water depth (m)	Velocity (m/s)	Bed elevation (m)	c_b -	ρ_s/ρ -	β -	f -
Test A	Left	2.00	1.00	3.00	0.65	2.650	0.01	1×10^{-4}
Test A	Right	4.00	4.38	2.15	0.65	2.650	0.01	1×10^{-4}
Test B	Left	6.00	0.01	1.00	0.65	2.650	0.01	1×10^{-4}
Test B	Right	0.38	5.01	3.75	0.65	2.650	0.01	1×10^{-4}

Table 2.4: Error norms L_1 for Test A and B.

Test Case	Scheme	Variable	Reference Solution	Time	L_1(m)
Test A	LHLLC	z_w	Exact	5 s	0.0174
Test A	LHLL	z_w	Exact	5 s	0.0176
Test A	LHLLC	z_w	LHLL	5 s	0.0039
Test A	LHLLC	z_b	Exact	5 s	0.0039
Test A	LHLL	z_b	Exact	5 s	0.0080
Test A	LHLLC	z_b	LHLL	5 s	0.0058
Test B	LHLLC	z_w	Exact	5 s	0.0130
Test B	LHLL	z_w	Exact	5 s	0.0173
Test B	LHLLC	z_w	LHLL	5 s	0.0050
Test B	LHLLC	z_b	Exact	5 s	0.0109
Test B	LHLL	z_b	Exact	5 s	0.0165
Test B	LHLLC	z_b	LHLL	5 s	0.0085

for both the liquid and solid phases using the approach described by Rosatti et all. [Rosatti et al., 2008], and in all cases the errors were 1.0×10^{-12}. This shows that the LHLL and LHLLC scheme conserves mass to numerical precision.

Fig. 2.9 and 2.10 shows predictions of the water surface z_w and sediment bed z_b for Test A and B, respectively. Clearly, the LHLLC scheme provides a sharper prediction of the z_b discontinuity than the LHLL scheme, which is overly diffusive here. On the other hand, the rarefaction waves are predicted equally well by the LHLL and LHLLC schemes.

Numerical errors are shown in Table 2.4 in the form of L_1 norms and allow for a quantitative comparison of the LHLL and LHLLC schemes. Focusing first on water surface predictions, z_w, the LHLLC scheme is slightly more accurate than the LHLL scheme but the difference is arguably negligible. Table 4 also shows L_1 norms computed between the LHLL and LHLLC predictions, and for z_w this is much less than the numerical error of the LHLLC and LHLL

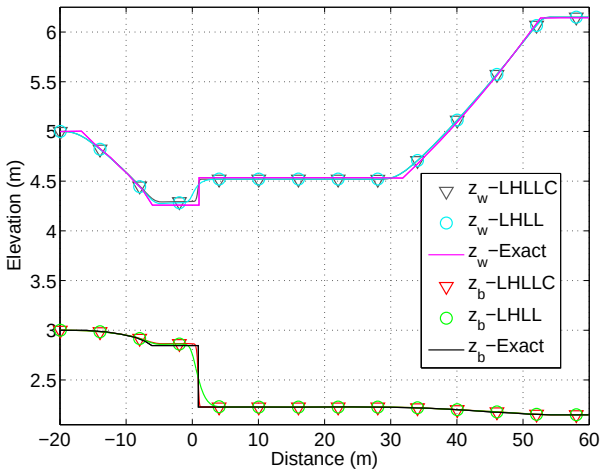

Figure 2.9: Test A water surface and bed elevation profiles at 5 s using Δx=0.1 m and Courant Number 0.95.

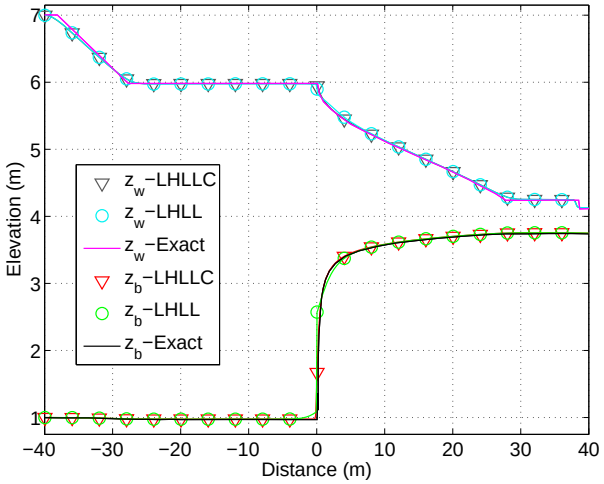

Figure 2.10: Test B water surface and bed elevation profiles at 5 s using Δx=0.1 m and Courant Number 0.95.

schemes.

Focusing now on bed elevation predictions, z_b, the LHLLC is about twice as accurate as LHLL in Test A, and about 30% more accurate in Test B. Also, in Test A, the L_1 norm measured between the LHLLC and LHLL schemes is larger than the error of the LHLLC scheme, which points to a clear advantage of the LHLLC scheme. Comparing errors in z_b versus errors in z_w, these are comparable in Test B but errors in z_w are larger in Test A. This difference is attributed to the relative range of the z_b and z_w values in these test cases.

Test A was repeated using Δx=0.8, 0.4, and 0.2 m and $Cr = 0.95$ to again verify that the LHLLC scheme converges with grid refinement. Fig. 2.11 shows that errors (L_1 norms) are geometrically reduced with refinement, and thus the scheme is again shown to converge in a classical sense.

2.4.6 Experimental Dam-Break Test

Testing now moves on to cases involving experimental data from Université Catholique de Louvain (UCL), Belgium [Spinewine and Zech, 2007] which have been used for previous DFM studies (e.g. [Zech et al., 2008]). The UCL experiments included a number of different scenarios, and four considered here are shown in Table 2.5. For each UCL scenario, available observation data includes profiles of the free surface elevation z_w, sediment layer elevation z_m, and the bed elevation z_b extracted from imagery collected from cameras mounted alongside the experimental apparatus Spinewine and Zech [2007].

The LHLLC and LHLL models are applied to solve the Two-Phase and Two-Layer DFMs using a grid resolution of Δx=0.01 m, a Courant number 0.9, and parameters shown in Table 2.5. The Two-Phase DFM does not predict z_m, so this is computed using the transformation given by Eq. 2.25 for comparison to the experimental data.

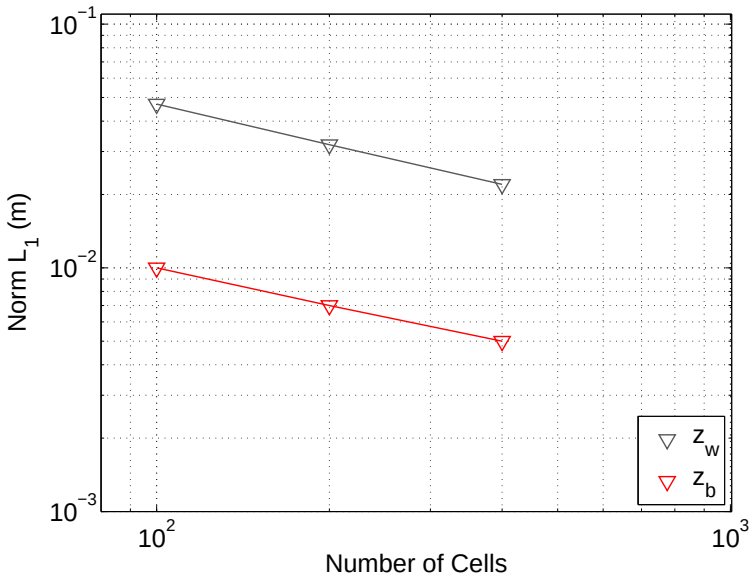

Figure 2.11: LHLLC scheme errors in Test A are shown to geometrically decay with grid refinement.

Table 2.5: Initial condition and parameters for UCL experimental dam-break test cases

UCL Test ID	Bed material	h_w-left (m)	h_w-right (m)	z_b-left (m)	z_b-right (m)	c_b	ρ_s/ρ	β	f
a	PVC	0.35	0	0	0	0.58	1.580	0.0125	0.024
a	Sand	0.35	0	0	0	0.53	2.683	0.0025	0.004
d	PVC	0.25	0.10	0.10	0	0.58	1.580	0.0125	0.024
d	Sand	0.25	0.10	0.10	0	0.53	2.683	0.0025	0.004

UCL Test (a)

First Test (a) is considered. Fig. 2.12 shows Two-Layer LHLLC predictions and measurements of z_w, z_m and z_b at t=0.5 s (left) and 1.0 s (right) for PVC bed material, and Fig. 2.13 shows the same results for sand bed material. Two-Phase LHLLC predictions, Two-Phase LHLL predictions, and Two-Layer LHLL predictions are not shown because they closely track LHLLC predictions. However, errors for all off these predictions are shown in Table 6.

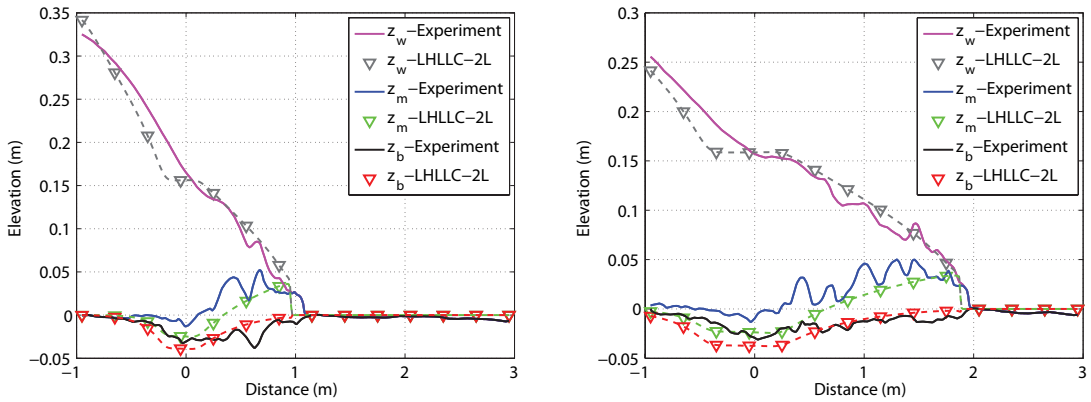

Figure 2.12: LHLLC Two-Layer DFM predictions of UCL Test (a) with PVC bed material at 0.5 s (left) and 1.0 s (right).

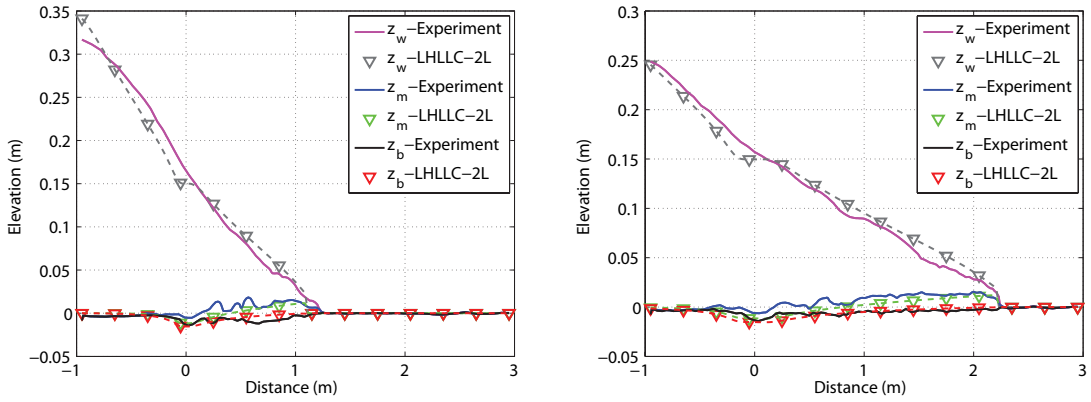

Figure 2.13: LHLLC Two-Layer DFM predictions of UCL Test (a) with sand bed material at 0.5 s (left) and 1.0 s (right).

The model predictions shown in Figs. 2.12-2.13. are qualitatively good, because the general

shape, width and depth of the water and sediment profiles are accurately captured. Clearly, there are small scale features that the model does not resolve, but this reflects complexities of the physical problem that are not resolved by the mathematical model, and not limitations of the numerical method.

Table 2.6: Error norms L_1 computed for UCL Test (a) at 1 s. †Indicates z_m computed using Eq. 2.25.

Scheme	Variable	Reference Solution	L_1(m) - PVC	L_1 (m) - Sand
LHLLC-2L	z_w	Experimental	0.0095	0.0070
LHLLC-2P	z_w	Experimental	0.0093	0.0066
LHLL-2L	z_w	Experimental	0.0095	0.0070
LHLL-2P	z_w	Experimental	0.0092	0.0066
LHLLC-2L	z_w	LHLLC-2P	5.08×10^{-4}	4.41×10^{-4}
LHLL-2L	z_w	LHLL-2P	8.12×10^{-4}	6.95×10^{-4}
LHLLC-2P	z_w	LHLL-2P	1.82×10^{-4}	9.32×10^{-5}
LHLLC-2L	z_m	Experimental	0.0127	0.0045
LHLLC-2P†	z_m	Experimental	0.0126	0.0046
LHLL-2L	z_m	Experimental	0.0127	0.0045
LHLL-2P†	z_m	Experimental	0.0126	0.0046
LHLLC-2L	z_m	LHLLC-2P†	1.99×10^{-4}	2.08×10^{-4}
LHLL-2L	z_m	LHLL-2P†	2.92×10^{-4}	2.69×10^{-4}
LHLLC-2P†	z_m	LHLL-2P†	1.14×10^{-4}	2.51×10^{-5}
LHLLC-2L	z_b	Experimental	0.0073	0.0022
LHLLC-2P	z_b	Experimental	0.0074	0.0021
LHLL-2L	z_b	Experimental	0.0073	0.0022
LHLL-2P	z_b	Experimental	0.0073	0.0022
LHLLC-2L	z_b	LHLLC-2P	3.37×10^{-4}	1.25×10^{-4}
LHLL-2L	z_b	LHLL-2P	4.09×10^{-4}	3.50×10^{-4}
LHLLC-2P	z_b	LHLL-2P	7.88×10^{-5}	1.92×10^{-5}

Errors shown in Table 2.6 indicate that the LHLLC and LHLL schemes are similarly accurate, when compared to laboratory measurements, and that the differences between predictions are about an order of magnitude smaller than the absolute errors. Further, for the case of PVC bed material, absolute errors in z_m are larger than errors in z_w which are larger than errors in z_b. On the other hand, for the case of sand bed material, absolute errors in z_w are larger than z_m which are larger than z_m errors.

These results show that accuracy in these test cases is not limited by the chosen DFM formulation (Two Phase vs. Two Layer), by the numerical method (LHLLC vs. LHLL), or by the bed material (PVC vs. sand). The sensitivity of errors to the numerical model

formulation and scheme is considerably smaller than the absolute error. The implication is that accuracy is limited by the basic assumptions of the governing equations: hydrostatic flow and our limited understanding of sediment entrainment. Nevertheless, it is important to stress that the numerical solutions are well behaved and qualitatively correct. Furthermore, the only obvious weakness of the numerical method, numerical diffusion, is not the factor limiting accuracy in this case.

UCL Test (d)

UCL Test (d) is now considered, a scenario that involves an initial discontinuity in the bed where purely gravitational effects (avalanching) can be expected to play a role in the evolution of the bed profile, in addition to hydrodynamic processes. As before, the model is applied using previously reported parameters shown in Table 5 (no parameter tuning or calibration), a grid resolution of Δx=0.01 m, and a Courant number of 0.9. Here, only the LHLLC scheme is used since little difference from LHLL predictions can be expected under high Fr conditions. Further, LHLLC scheme is applied with, and without, avalanching to illuminate the potential importance of this process. The critical slope S_c for sand bed is set to 0.3 based on recommended values for wet sand (e.g. [Roelvink et al., 2009]), and to 0.15 for PVC bed.

Fig. 2.14 and 2.15 show predictions for the case of PVC and sand material, respectively, and in comparison to the measured profiles. In both cases, predictions without (left) and with (right) avalanching are shown, illustrating that the avalanching scheme improves accuracy in both cases. Table 2.7 shows that errors of the LHLLC scheme with avalanching are 20-25% smaller than errors of the LHLLC scheme without avalanching, which points to a significant accuracy advantage.

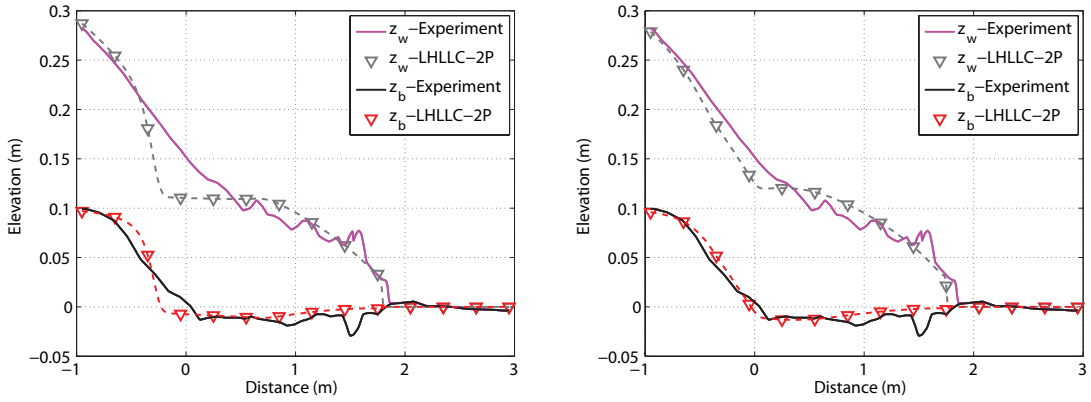

Figure 2.14: LHLLC Two-Layer DFM predictions of an erosional dam-break flow with PVC bed material at 1 s without avalanching (left) and with avalanching (right).

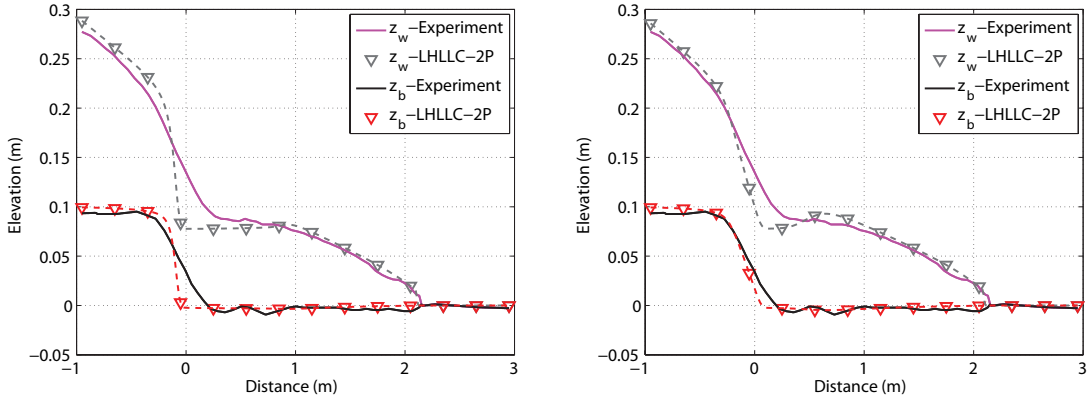

Figure 2.15: LHLLC Two-Layer DFM predictions of an erosional dam-break flow with sand bed material at 1 s without avalanching (left) and with avalanching (right).

2.4.7 Aggradation Test

The flume experiments of Soni et al. [Soni et al., 1980] have been used for previous modeling studies of sediment transport (e.g. [Cao et al., 2002]) and are used here to further evaluate the LHLLC scheme. In this test, the laboratory flume is 0.2 m wide and 30 m long. The flume is sloped at 0.00356 and sediment is supplied at a baseline rate of 1.5×10^{-5} $m^3/s/m$ with a flow depth of 0.05 m and an inflow velocity of 0.4 m/s, producing a sediment profile that is essentially uniform and parallel to the flume bottom slope. Next, the sediment inflow was increased by a factor of four while maintaining an inflow depth and velocity of 0.05 m and 0.4 m/s, respectively. This load exceeds the flows carrying capacity, so deposition occurs

Table 2.7: Error norms L_1 computed for UCL Test (d) at 1 s.

Scheme	Variable	Reference Solution	Avalanching	L_1(m) - PVC	L_1(m) - Sand
LHLLC-2P	z_w	Experimental	Off	0.0121	0.0088
LHLLC-2P	z_w	Experimental	On	0.0095	0.0066
LHLLC-2P	z_b	Experimental	Off	0.0062	0.0045
LHLLC-2P	z_b	Experimental	On	0.0049	0.0032

in the flume and the sediment profile changes over time. The Two-Phase LHLLC DFM is applied to examine its performance in modeling the deposition of sediment and subsequent aggradation of the channel bed. The model is applied with a grid resolution of Δx=1 m, a Courant number of 0.95 s, $\beta = 0.0004$ and $f = 0.01$. The parameters β and f were calibrated to minimize the L_1 norm of water surface and bed elevation predictions at t=30 min, and predictions at t=40 min are used to assess predictive skill. The avalanching scheme is irrelevant in this test case because of the mild slopes.

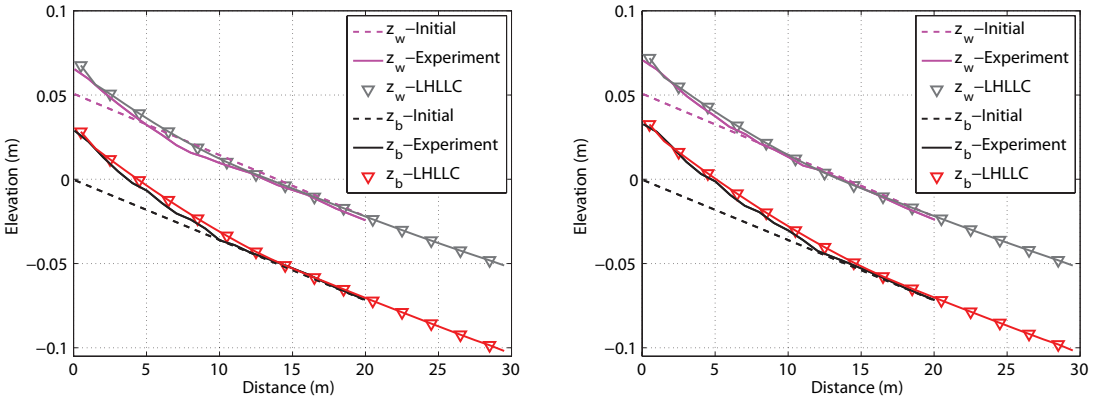

Figure 2.16: LHLLC Two-Phase DFM predictions of water surface and bed profile in Aggradation Test: t=30 min (left) and 40 min (right).

Fig. 2.16 shows model predictions of z_w and z_b at t=30 and 40 min. Errors are shown in Table 2.8. Qualitatively, model predictions compare very well with the experimental data. The length of the aggradation profile and concave-up curvature are correctly captured at t=30 and 40 min, respectively. Since the accuracy of the model does not appear to change over time, the model is found to offer a good representation of aggradation dynamics.

Table 2.8: Error norms L_1 computed for Aggradation Test.

Variable	Reference Solution	Time	L_1(m)
z_w	Experimental	30 min	0.0240
z_b	Experimental	30 min	0.0259
z_w	Experimental	40 min	0.0214
z_b	Experimental	40 min	0.0208

2.4.8 Knickpoint Test

A "knickpoint" refers to a change in channel slope and is associated with changes to a channel's carrying capacity [Brush and Wolman, 1980, Goutire et al., 2008]. Thus, dynamic perturbations of a channel profile can be expected to originate from knickpoints, and the focus of this test is on ability of the LHLLC scheme to capture these dynamic phenomena. A knickpoint experiment conducted at Université Catholique de Louvain (UCL), Belgium is the basis of this test [Goutire et al., 2008]. The laboratory flume is 7.6 m long and 0.5 m wide, and at the knickpoint, the slope transitions from 0.0057 to 0.024 at a distance of 6.3 m from the upstream boundary. Flow is supplied at a rate of 0.0098 m^3/s and at a depth of about 0.028 m. No sediment is supplied at the upstream boundary. The expected response is downcutting in the vicinity of the knickpoint, and the gradual extension of this perturbation in both the upstream and downstream directions. The Two-Phase DFM is applied to this problem using a grid resolution of Δx=0.1 m, a Courant number of 0.95, $\beta = 0.00045$ and $f = 0.01$. The values of β and f were manually calibrated to minimize the L_1 norm of the predictions at an initial time, 108 s, and the performance of the model is assessed based on its accuracy at a later time, 831 s. As in the previous test case, the avalanching scheme is irrelevant in this test case because the slopes do not approach the critical slopes for stability. Fig. 2.17 shows model predictions of z_w and z_b at t=108 and 831 s. Errors are shown in Table 2.9. As in previous tests, model predictions are qualitatively good, with the schemes correctly prediction the rounding (or diffusion) of the knickpoint at t=108 s and the rate of knickpoint downcutting at t=831 s but it slightly overestimates erosion upstream of the knickpoint at t=831 s. Also, the scheme is not able to reproduce

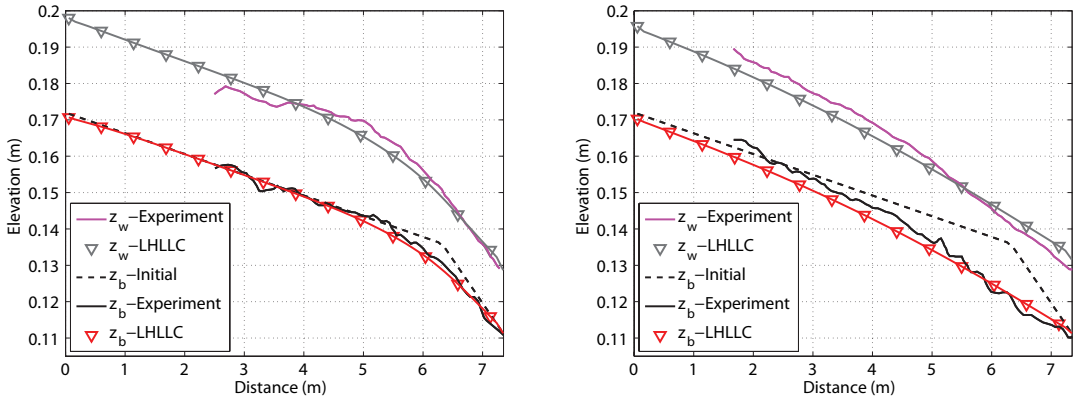

Figure 2.17: LHLLC Two-Phase DFM predictions of water surface and bed profile in Knickpoint Test: t=108 s (left) and 831 s (right).

the small-scale variability that is present in the measured bed profiles. However, this can be attributed to complex non-linear fluid/sediment feedback processes that are not captured by the mathematical model, and thus should not be misinterpreted as a drawback of the LHLLC scheme.

Table 2.9: Error norms L_1 computed for Knickpoint Test.

Variable	Reference Solution	Time	L_1(m)
z_w	Experimental	108 s	1.7055×10^{-4}
z_b	Experimental	108 s	1.011×10^{-4}
z_w	Experimental	831 s	0.0014
z_b	Experimental	831 s	1.3068×10^{-4}

2.4.9 Lake Deposition

The LHLL scheme was also applied to the two previous test cases (Aggradation Test and Knickpoint Test) but it performed poorly. Predictions deviated far from the experimental observations leading to errors that were orders of magnitude larger than the LHLLC scheme. This was attributed to the overly diffusive nature of the LHLL scheme's mass flux, which is accentuated by increasing slopes in z_b and z_w. Conversely, the UCL dam-break test problems do not reveal this problem with the LHLL scheme, presumably because of supercritical flow

conditions where the diffusive error is negligible.

One final application is presented to illustrate this potentially important advantage of LHLLC over LHLL. The test case involves a channel that flows into a lake with variable bathymetry, where sediment is deposited, as shown in Fig. 18. Here, flow is from right to left. The depth in the river is 4 m and the depth in the lake increases to 20 m. For simplicity, the bed of the system is horizontal except for the linear break in elevation between x=30 and 40 m. The initial condition corresponds to z_w=0 m and u_m=0 m/s. For boundary conditions, a liquid discharge of 0.6 m^3/s/m (flow is right to left) is specified at the upstream boundary, the sediment volumetric concentration in the influx at the upstream boundary is set to 0.00001, and $z_w = 0$ is specified at the downstream boundary. The correct solution to this problem is a filling of the lake bed over a time scale of years, a consequence of the deposition of river sediment within the lake (deep water). The Two-Phase DFM is applied using both LHLL and LHLLC, a grid resolution of Δx=1 m, a Courant number of 0.95, and the avalanching scheme not activated. The model is applied using $\beta = 0.0025$ and $f = 0.01$. Fig. 2.18 shows LHLL and LHLLC predictions after 100 s (top right), 1,000 s (bottom left), and 36,000 s (bottom right). The indicates that the LHLLC scheme predicts a stable lake bathymetry, whereas the LHLL scheme incorrectly predicts at flattening of the lake bottom as if the deep part of the lake were quickly filled with sediment from the shallow part of the lake. Clearly, the excessive dissipation of the LHLL scheme makes it unsuited to this type of practical application, whereas the LHLLC scheme performs far better. Granted, DFMs were developed primarily to model flows with high concentrations of suspended sediment, and this corresponds to a problem with low sediment concentration. Nevertheless, it is desirable to have models that can be successfully applied to a wide range applications and the LHLLC is advantageous for this reason.

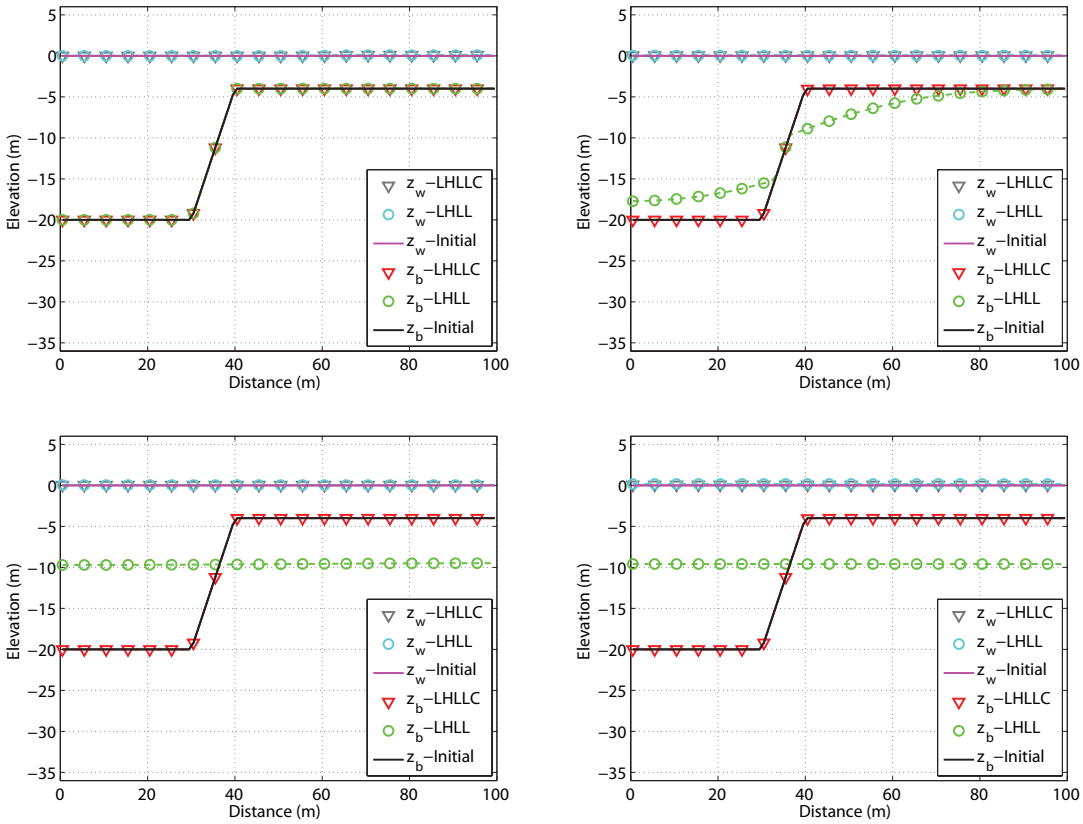

Figure 2.18: Change in cross section; left top panel results at 5 s, and right top panel shows the results at 100 s. Lower left panel shows the results at 1000 s and lower right panel shows the results at 36000 s.

2.5 Conclusions

An LHLLC scheme is presented to solve either Two-Phase or Two-Layer DFMs, and it is shown that for the specific DFMs considered here, the solution to one can be recovered from the other without solving a separate set of equations. The DFMs resolve key flow attributes such as the depth of fluid and sediment mixture layers and speed of fluid and sediment fronts, but do not resolve small scale variability associated with non-hydrostatic flow processes. In practice, it is recommended that the Two-Layer model be applied to applications with strong bed load transport and the Two-Phase model be applied to applications with strong suspended load transport so the most appropriate sediment transport (entrainment) model can be used.

The LHLLC scheme can be viewed as an enhanced version of the LHLL scheme with several advantages and broader applicability compared to the LHLL scheme, as described below.

1. The LHLLC scheme can be applied to test problems with steep, submerged slopes whereas the LLHL scheme will erroneously predict massive terrain slumping. This is attributed to use of the contact wave speed for sediment mass flux computations.

2. The LHLLC predicts significantly less numerical diffusion of sharp sediment fronts under subcritical flow conditions, compared with the LHLL scheme.

3. The LHLLC scheme will preserve stationary solutions involving wet/dry interfaces, whereas the LHLL scheme does not. This results from the introduction of a wet/dry tolerance and a modified flux under "dry" conditions.

4. The LHLLC scheme includes an avalanching scheme that accounts for gravity-driven slumping of steep slopes. This is shown to offer improved accuracy in a channel flow test problem and is expected to be important in field applications to account for slumping of near vertical channel features common to incised channels.

Chapter 3

Terrestrial Laser Scanning of Anthropogenic Beach Berm Erosion and Overtopping

This Chapter has been published in Journal of Coastal Research. Citation: Schubert, J.E.,Gallien,T.W., Shakeri Majd, M. and Sanders, B.F. (2015), Terrestrial Laser Scanning of Anthropogenic Beach Berm Erosion and Overtopping, *Journal of Coastal Research*, *31(1)*, *47-60*, http://dx.doi.org/10.2112/JCOASTRES-D-14-00037.1.

3.1 Introduction

Anthropogenic berms refer to a mechanically constructed ridge of sand positioned on the crest of the natural beach profile. Sand (0.2-0.5 m) is typically scraped from the foreshore and deposited on the beach crest [Bruun, 1983].Anthropogenic berms may be constructed in the days and hours before an anticipated marine flood event such as an extreme high tide or an energetic swell event, on a seasonal basis in anticipation of the storm season, and on a continual basis to maintain or strengthen persistent berms. The practice originated primarily as an erosion control strategy(e.g.,[Bruun, 1983, Tye, 1983, McNinch and Wells, 1992, Wells and McNinch, 1991]) , and has been widely deployed as a coastal management technique along the US eastern and Gulf coasts [Wells and McNinch, 1991, Clark, 2005, Kratzmann and Hapke, 2012], in Australia [Carley et al., 2010], and in Europe [Rogers et al., 2010, Harley and Ciavola, 2013]. Gallien et al. [2014] report three distinct types of berming in the southern California bight based on deployment duration: event, seasonal and persistent. Event berms are triangular in cross-section, extend 60-600 m in the alongshore direction, and exhibit both the lowest volume (4 m3/m) and average crest elevations (5 m NAVD88) of all berms studied. Seasonal berms extend 70-980 m alongshore, are 6 m3/m to 28 m3/m in volume and average crest elevation varies from 5.3 to 6.4 m NAVD88. The largest, longest and highest of all berms in southern California bight protects the Naval Amphibious Base Coronado in San Diego and averages 48 m3/m, 1.2 km in length and nearly 7 m NAVD88 in mean crest elevation. Note that event berms and seasonal berms in the region are considerably smaller in length, height and width than those constructed along the Atlantic and Gulf coasts [Gallien et al., 2014]. Examples of event type berming at Newport Beach are shown in Fig. 3.1. Note from Fig. 3.1. that berms are sometimes constructed from the shoreward side, particularly if access to the beach foreshore is restricted. Berms are constructed in southern California primarily to guard against coastal flooding into urban lowlands, where significant damages would follow. Here, coastal flooding is driven by a combination of factors such as high

Figure 3.1: Anthropogenic berm such as these are constructed in the days and hours before an anticipated flood event in Southern California, and have been termed event-type berms by [Gallien et al., 2014].

astronomical tides, waves, storm surge, and other fluctuations such as those caused by the El Nio Southern Oscillation (ENSO) [Cayan et al., 2008]. More frequent and damaging storms resulting from the combination of higher sea levels, storm surge, high tides, and waves are expected to test the limits of coastal flood defenses [Strauss et al., 2012]. Tebaldi and Zervas [2012] conclude that Southern California is among the most sensitive areas of the United States: today's 100 year coastal flood will become an annual occurrence by the year 2050. Additionally, a statewide impact assessment indicates a wide range of critical infrastructure including 5,600 kilometers of roadways, 450 kilometers of railways, 29 wastewater treatment facilities and countless buildings and contents valued at over 100 billion dollars will be at risk of coastal flooding by 2100 based on 1-1.4 m in sea level rise [Heberger and et.al., 2009]. Globally, over 20 million people reside below present high tide levels and as many as 200 million are vulnerable to flooding during extreme events [Nicholls, 2010, 2011]. Globally, concomitant pressures of urbanization and climate change point to significant increases in the vulnerability of major port cities to flooding. Population exposure is expected to triple, whereas a tenfold increase in asset exposure totaling 9% of global gross domestic product is anticipated [Hanson et al., 2011].

In the short term, accurate mapping of coastal flooding is critical for anticipating and mitigating flood vulnerabilities and responding to emergencies [National Research Council, 2009]. In urban lowlands, hydraulic models have been successfully used to map flood impacts driven by extreme high tides and storm surge [Bates et al., 2005, Brown et al., 2007, Purvis et al., 2008, Dawson et al., 2009, Knowles, 2010, Martinelli et al., 2010, Smith et al., 2012, Wadey

et al., 2012] but predictive skill has been limited by uncertainties in wave-driven overtopping volumes [Wadey et al., 2012]. Recent research suggests that wave statistics including significant wave height and period can be combined with relatively simple beach parameters such as slope and freeboard to empirically estimate the overtopping flows [Laudier et al., 2011, Gallien et al., 2014], data which can then be input to hydraulic models as a line source (along the inland crest of a beach berm) to simulate resulting patterns of urban flooding as shown by [Gallien et al., 2014]. Alternatively, coupled hydromorphological models (e.g., [Roelvink et al., 2009, van Rijn, 2009, Figlus et al., 2011, Vousdoukas et al., 2012, Zhu and Dodd, 2013, Harley and Ciavola, 2013]) may prove capable of describing beach change and overwash volumes sufficient for coastal flood prediction. Flood mapping by planar extrapolation of wave runup heights, while far easier and proven for mapping flood zones along many shorelines, is unfortunately inadequate for urban lowlands [Bates et al., 2005, Gallien et al., 2013, 2014]. Generally, there is a lack of field data characterizing berm performance during storms and the impacts of berm failure on the timing and distribution of coastal flooding.

This paper presents the results of a field campaign to document the initial conditions and dynamic erosion of anthropogenic berms using terrestrial laser scanning (TLS). TLS is increasingly applied for studies of beaches [Feagin et al., 2014] and has been combined with video analyses for wave-by-wave studies of morphodynamics [Vouskoukas et al., 2014]. On three occasions in February and March of 2012, a prototype berm was constructed on the foreshore of Newport Beach at low tide, scanned to document its initial shape, and then scanned in near-continuous fashion with the rising tide to document subsequent erosion. The purpose is two-fold: (1) to measure the performance of the TLS system relative to accuracy and assess strengths and drawbacks that are likely to bear on the suitability of this technology to support flood prediction, and (2) to obtain a better understanding of the resilience of anthropogenic berms to erosion and overtopping when exposed to a rising tide and waves. In particular, we seek an understanding of basic mechanisms by which the berm is eroded, and a deeper understanding of the rate of erosion and the factors controlling it.

More broadly, we seek to promote improved predictions of coastal flooding in urban lowlands.

3.2 Newport Beach Site Description

The study site is adjacent to Newport Pier in the City of Newport Beach, CA, approximately 70 km southeast of central Los Angeles (see Figure 2). The Pier is located on Balboa Peninsula separating the Pacific Ocean from Newport Bay, and is located at a break in the strike of the shoreline. Upcoast of the pier, where berm experiments are performed, the beach faces West-South-West (236 °from North) and downcoast the beach faces South-South-West (196 °from North). Lower Newport Bay is densely developed featuring an active pleasure craft harbor, as shown in Fig. 3.2, while the upper bay is a nature preserve with extensive salt water wetlands (not shown in Figure 2). Areas bordering the lower bay are vulnerable to flooding, particularly Balboa Island and Balboa Peninsula. Sheltered from significant wave action, Balboa Island floods when high embayment levels overtop concrete flood defenses, while the Peninsula may flood from high embayment levels or wave runup and overtopping of the beach [Gallien et al., 2011, 2013, 2014]. Temporary event-type berms are deployed along the ocean facing portion of Newport Beach to mitigate flooding threats from the coincidence of high tides and long period swell. Ocean levels at Newport are influenced by astronomical tides ranging between 1-2.7m (NAVD88, tidal epoch 1983-2001 at Newport Bay entrance), storm surge, El Nio thermal expansion and wave setup, which under extreme conditions may superelevate astronomical tide water levels by a further 0.5 m [Flick, 1998].

3.3 Methods

Prototype berms were constructed on three dates: February 21st, 2012 (Berm 1), March 7th, 2012 (Berm 2) and March 20th, 2012 (Berm 3). These dates correspond to the availability

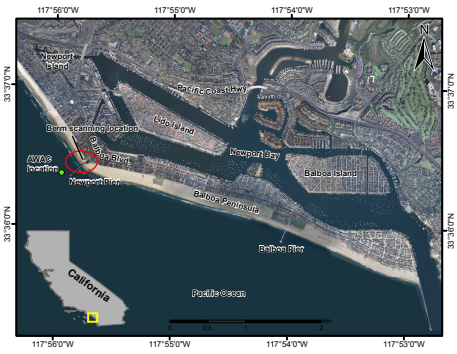

Figure 3.2: Berm experiments were conducted adjacent to Newport Pier in Newport Beach, California. Berms were constructed at low tide, and exposed to run up and waves. The location of a wave and pressure measurements (AWAC) is shown.

of City personnel and a sufficiently large intertidal range to facilitate berm construction, i.e., a low tide that creates access to the foreshore and a high tide that ensures complete erosion of the berm. In practice, berms may be constructed over several kilometers of shoreline in advance of a storm, but only a berm of limited length was possible here due to construction and scanning limitations. The prototype design is modeled after event-type berms used throughout the region and consisted of a central section parallel to the shoreline, ca. 16 m long and 2 m high, and flanked by 8 m long angled walls as shown in Figure 3. This design guards the back side of the berm from flooding during the initial stages of attack, and prolongs the duration over which the berm is eroded exclusively from its ocean-facing side. The berm was constructed with a front-end loader (Model 624J, John Deere, Moline, IL) operated by a City of Newport Beach employee. The loader scraped sandy material immediately inland (Berm 1 and 2) or seaward (Berm 3) of the berm. Survey stakes around the intended footprint of the berm guided placement of the sand. Similar to berm erosion field experiments conducted by Fisher, Overton ad Chisholm (1986) at Duck, NC, the berm toe was placed at approximately mean sea level (MSL, 0.8 m above NAVD88). During low tide, initial front and back TLS scans were performed and the digital camera was positioned on Newport Pier. A RTK-GPS receiver provided real time elevation data for accurate vertical positioning of the berm on the beach face, as described in the next section. No compaction or profiling of the berm was attempted. The deposited material was left unconsolidated with

front and back slope angles ranging from 32-37, which are typical values for damp sand. The median grain size of the sandy beach material was analyzed for each constructed berm and found to be uniformly D50=0.42 mm. Resulting berm heights and cross-shore widths for the central berm section (parallel to the shoreline) were as follows: Berm 1 (1.3 m high, 3.0 m wide), Berm 2 (1.4 m high, 3.7 m wide) and Berm 3 (1.8 m high, 4.5 m wide).

3.3.1 RTK-GPS Survey

A ProMark3 geodetic survey receiver using the global positioning system (GPS) (Magellan, Santa Clara, CA, US) was used to georeference the TLS, guide berm construction, measure beach slopes, and provide control points to measure the accuracy of the TLS data. In stand-alone mode the ProMark3 has point accuracy of 3 m. When receiving corrections, however, the unit can operate in real-time-kinematic (RTK) mode and produce centimeter accuracies both in the horizontal and vertical. To receive real-time corrections, the GPS unit was linked wirelessly to base station FVPK of the Orange County Real Time Network (OCRTN), with baseline length of 5 km. The real time network provides corrections better than 2 cm in the horizontal and 4 cm in the vertical [OCPW, 2009]. Each RTK-GPS observation consists of X,Y and Z information referenced to NAD83 and NAVD88. Survey points were collected on the relatively flat foreshore around the perimeter of the berm, and additional points were collected on the foreshore and in waist deep water at low tide to measure the foreshore beach slope.

3.3.2 Berm Scanning

Terrestrial laser scanning (TLS) or lidar has emerged as a valuable technology for capturing the three dimensional geometry of complex objects ranging from forests to industrial facilities [Vossman and Maas, 2010]. Aerial laser scanning (ALS) has yielded high resolution digital

terrain models (DTMs) that support a new class of detailed and accurate flood models [Bates, 2012] as well as numerous studies of beach dynamics (e.g., [Brock et al., 2002, Sallenger and et al., 2003, Yates et al., 2008]). TLS data has been shown to enhance the local precision of urban flood predictions by mapping features such as sidewalks and street surface camber [Sampson et al., 2012] and could prove invaluable for coastal flood prediction by quickly mapping beach topography before an imminent flood threat and reducing uncertainties. TLS systems can be used for more detailed morphodynamic studies (e.g., [Feagin et al., 2014]) and TLS systems on mobile platforms (e.g,. [Barber and Mills, 2007, Bitenc et al., 2011, Sampson et al., 2012]) could enable a beach scan over the scale of a city in a matter of hours, although extreme care would be required for a high level of accuracy, e.g., 1-5 cm. Topographic accuracies in this range have proven necessary to predict the onset of overtopping for weir-like overflow events [Gallien et al., 2011].

A GX3D (Trimble, Sunnyvale, CA, US) TLS was used for berm scanning. The system relies on a pulsed laser to sample the three-dimensional (3D) properties of surfaces and objects. The Trimble unit allows for 360 horizontal and 60 vertical continuous scanning and has a maximum optimal scan range of 200 m. Scanned relative point accuracy is dependent upon scan range, and for this project laser scanning was undertaken at a distance of less than 100 m, allowing for a best system scan accuracy of ¡7 mm. During station setup the GX3D was manually leveled within 0.001 and an in-built, dual-axis tilt compensation system with automatic leveling allows for correction of level drift, that may occur from system vibration or settling, within a 0.25 range. The measured output consists of a data point-cloud, where each point is attributed with an easting, northing, orthometric elevation as well as a pulsed laser reflection intensity. The GX3D uses a pulsed 532 nm (green) laser which is not designed to penetrate through water, and thus measurements over water surfaces such as the swash zone may be difficult to interpret. While the reflection intensity depends on many factors, it is inversely related to the presence of water and thus can help to identify water lines on the beach.

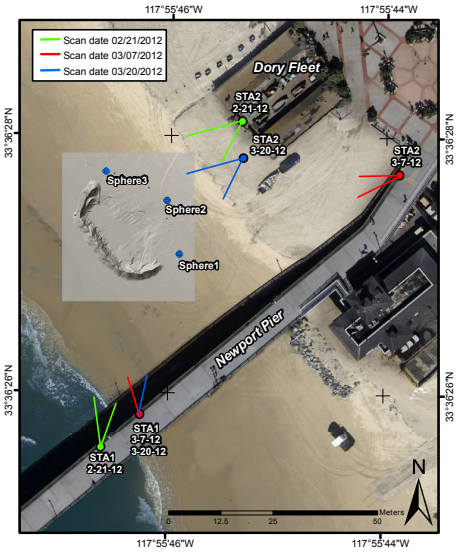

Figure 3.3: Berms were constructed next to Newport Pier to enable continuous scanning and time-lapse photography with an on-shore perspective (front scan). Scans with an off-shore perspective (back scans) were also completed to build a three-dimensional point cloud of each berm, and survey spheres (shown) were deployed to merge front- and back-scans in a post-processing step.

Front (STA1) and back (STA2) TLS scans were completed immediately after berm construction on each of the three test dates to characterize the initial berm geometry. Locations for STA1 and STA2 were varied across the three study dates for the best possible scan coverage, considering the location of the berm and line-of-sight obstructions such as maintenance vehicles. Locations of (STA1) and (STA2) and approximate survey sphere placements used for automatic georeferenced merging of front- and back-scans are also shown in Fig. 3.3. The geodetic locations of STA1 and the survey spheres were surveyed using RTK-GPS and converted to NAD83 and NAVD88. While an assessment of the GPS vertical accuracy was not conducted on each survey day, a previous test at this site with the same equipment yielded a vertical accuracy of 1.4 cm [Gallien et al., 2011]. All point clouds were georeferenced using STA1 and survey spheres corrected RTK coordinates as control points. The TLS was set to scan using a maximum resolution of 7.5 cm at the furthest distance (STA1), and the scan interval was proportionally smaller at shorter distances. This resolution was chosen so each scan would take 3-5 minutes.

Following the initial front and back scans, front scanning with the TLS continued with the

rise of the tide and the progressive erosion of the berm. Actual scan times varied between 3-16 min with an average scan interval of 6 min. Variability in the scan interval was due to scanner self-calibration, which occurred automatically when heavy wind gusts unsettled the TLS.

3.3.3 Time Lapse Photography

A Powershot G12 (Canon USA, Melville, NY) photocamera was used during each geodetic survey to capture digital images of the beach berm at one minute time intervals. The camera was tripod mounted and the shutter was triggered automatically using a shutter release unit. The images were time stamped and used to produce an optical time-lapse of the berm erosion process. An example of the captured photos can be seen in Fig. 3.4.

Figure 3.4: Photographs of Berm 2 at (left to right) 17:00, 18:00, and 18:30 shows the progressive rise of the tide and erosion of the berm that occurred in each of the three experiments.

3.3.4 Berm Data Processing

The georeferenced point clouds of merged front- and back-scans were combined into a single point cloud representative of the initial conditions. Subsequent front scans combined with the initial back scan characterize the time-dependent geometry of the berm, however eroded portions of the berm visible in the back scan must be removed. This primarily affects point clouds corresponding to advanced stages of erosion. A processing workflow was established using ESRI's ArcMap 10.0 (ESRI, Redlands, CA) to eliminate eroded back-scan points based on the intersection of the coverage area of front-scan points. After creating a series of point

clouds corresponding to different times, a 7.5 cm resolution DTM was created using inverse distance weighting (IDW) interpolation. Examples of the generated berm DTMs for each survey day are shown in Fig. 3.5. Reflected TLS intensity was recorded and processed along with surface elevations to study beach surface characteristics under rising tide and wetting berm surface conditions. The uncalibrated reflectance intensity was also interpolated to a 7.5 cm resolution raster grid using IDW interpolation and an example of berm reflected intensity in intensity units (iu) over time is shown in Fig. 3.6.

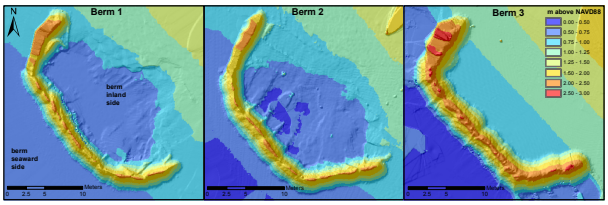

Figure 3.5: DTMs show that the geometry and orientation of Berms 1, 2 and 3 were similar, and that Berm 3 was the highest of the three.

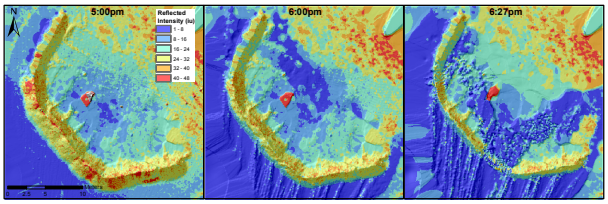

Figure 3.6: The lidar intensity reveals the interface between water and sub-aerial sand because the return from water corresponds to low intensity.

Sand volumes for each berm scan were calculated using a raster model of the berm height, measured relative to the sloping foreshore. A DTM of the sloping foreshore was created by removing berm object points from each lidar point cloud and again applying IDW interpolation onto the same 7.5 cm resolution raster grid. The berm height model was computed by subtracting the foreshore DTM from the original DTM. Volumes were then calculated in ArcMap 10.0 above the zero elevation reference plane. Percent erosion was computed by subtracting the berm volume of each scan from the initial volume, and normalizing by the initial volume. The berm height raster models were also used to extract cross-sectional and alongshore profiles of the berms at each time step. Alongshore profiles of the berm crest

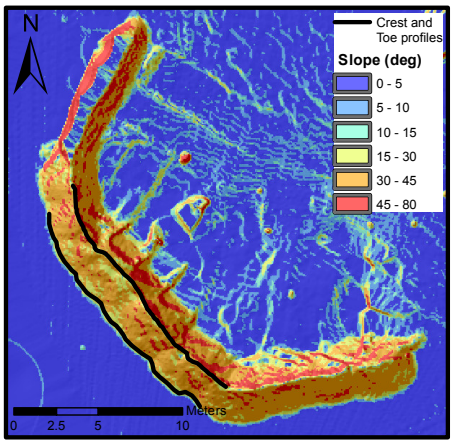

Figure 3.7: Polylines were etched along the toe and crest of each berm to extract average toe and crest elevations, as well as minimum crest elevations, as shown here for Berm 2.

and berm toe were identified by computing a raster model of the berm slope and contouring slope values, which clearly showed the crest and toe position as shown in Fig. 3.7. Crest and toe polylines were then traced manually, and elevations along the line were extracted at approximately 10 cm intervals. Separate polylines were saved for each time step where a noticeable change occurred in toe or crest shape. The average toe elevation, the average crest elevation, and the minimum crest elevation were saved for each time step for subsequent analysis. It is noted that the reported berm toe elevation may be higher than the actual toe elevation toward the end of each berm experiment because the pulse lidar cannot penetrate water and see measure a submerged toe elevation. Toward the end of each experiment, errors in the reported toe elevations may be in the 5-10 cm range, while errors during the initial stages of berm erosion are likely less than 3 cm.

The preceding polylines were also used to extract crest-averaged and toe-averaged lidar intensity data at each time step. An advantage of this averaging is the removal of "salt and pepper" noise caused by a combination of scan pattern, receiver automatic gain adjustments, laser reflection angle as well as material properties of the reflecting surface [Nobrega et al., 2007, Chust et al., 2008].

3.3.5 Wave and Pressure Measurements

An AWAC wave/current gage (Nortek AS, Oslo, Norway) was deployed in approximately 10 m of water and 300 m directly offshore of the berm to measure directional wave properties and pressure. The instrument was deployed in early January, 2012 and collected data for a period exceeding three months. The AWAC operates in stand-alone mode with an external battery for power and internal memory for data recording. Wave height accuracies are stated to be less than 1%, and pressure resolution and absolute accuracies are less than 0.005 and 0.1% of the total depth. This corresponds to a resolution and accuracy of 0.05 and 1 cm based on the 10 m water depth. The AWAC measured waves at the top of every hour using a 17 minute burst window at a rate of 4 Hz. Pressure was sampled at 1 Hz every 10 minutes for a two minute period. Wave measurements were processed using Storm commercial processing software (Nortek USA, Boston, MA), results are shown in Table 3.1.

Table 3.1: Attribute of hourly wave data during erosion experiments. Local Standard Time (LST). † Stockdon et al. (2006) formula. ‡ Guza and Thornton (1981) formula.

Survey Date	Time(LST)	H_{mo}(m)	T_p(s)	ξ	$<\eta>(m)^{\dagger}$	$<\eta>(m)^{\ddagger}$	$R_2(m)^{\dagger}$
21 February 2012	1800	0.52	11.5	0.30	0.054	0.088	0.426
21 February 2012	1900	0.50	11.4	0.30	0.053	0.085	0.414
21 February 2012	2000	0.58	11.8	0.29	0.059	0.099	0.462
7 March 2012	1700	1.13	11.5	0.27	0.107	0.192	0.664
7 March 2012	1800	1.22	11.4	0.26	0.110	0.207	0.684
7 March 2012	1900	1.09	11.4	0.27	0.104	0.185	0.647
20 March 2012	1600	0.59	11.5	0.37	0.077	0.100	0.480
20 March 2012	1700	0.63	11.4	0.36	0.079	0.107	0.492
20 March 2012	1800	0.52	12.4	0.43	0.078	0.088	0.486

Pressure data was processed to fill hourly data gaps, remove high frequency variability, and reference the resulting time series to NAVD88. Data gaps were filled using piecewise cubic Hermitian interpolation (Matlab, Natick, MA) and the resulting time series was low-pass filtered in the frequency domain to resolve variability at periods longer than two hours including the dominant modes at diurnal and semidiurnal periods. Six-minute NOAA tide measurements at Los Angeles (35 km to the Northwest) were used to reference the pressure

data to NAVD88. A variable offset (correction) was computed by subtracting a running, fortnightly-average pressure (depth) from a running, fortnightly-average Los Angeles tide height referenced to NAVD88, and resampled every 10 min by interpolation for consistency with the 10 min pressure data. The offset/correction was then added to the low-pass filtered pressure data to yield a local time series of water height relative to NAVD88. A variable offset was used to account for settling of the instrument over time by 5-10 cm, which was revealed by an increasing trend in the fortnightly pressure averages over the deployment period when fortnightly tide averages at Los Angeles and La Jolla (130 km to the Southeast) exhibited a weaker but decreasing and coherent trend. That is, the fortnightly tide height average at Los Angeles and La Jolla tracked very closely with maximum differences of 2.35 cm, and average differences of 0.58 cm. Hence, we have assumed that the running (every 10 min) fortnightly average of the Newport Pier and Los Angeles tide remain equal, giving a Newport tide record referenced to NAVD88 with a maximum error of 2.35 cm based on the Los Angeles/La Jolla comparison. The offset/correction was -10.78, -10.80 and -10.79 m coincident with Berm 1, 2 and 3 experiments, respectively.

3.3.6 Wave Setup and Runup Estimates

Wave setup and runup were calculated to characterize water levels at the berm face in relation to datum-referenced water heights outside the surf zone, as described above. Based on the beach slopes and wave properties shown in Table 1, the Iribarren number ξ, setup $< \eta >$, and runup R_2 (2% exceedance probability) were computed in accordance with [Stockdon et al., 2006] as follows,

$$\xi = \frac{\beta_f}{(H_0/L_0)^{1/2}} \tag{3.1}$$

$$< \eta >= 0.35\beta_f (H_0 L_0)^{1/2} \tag{3.2}$$

$$R_2 = 1.1(0.35\beta_f(H_0L_0)^{1/2} + \frac{1}{2}[H_0L_0(0.56{\beta_f}^2 + 0.004)^{1/2}]) \tag{3.3}$$

where β_f is the foreshore beach slope, and H_0 and L_0 represents the deep water wave height and length, respectively. An additional setup estimate was computed as follows [Guza and Thornton, 1981],

$$< \eta >= 0.17H_s \tag{3.4}$$

where H_s represents the significant wave height at the 10 m depth. The shoaling coefficient, $K_s = H_s/H_0$, was computed to be 1.028 (nearly unity) based on the wave periods shown in Table 3.1 using the University of Delaware on-line wave calculator (R. Dalrymple), so for this study, wave heights at 10 m depths were used for all setup and runup calculations. Additionally, linear wave theory was used to compute the deep water wavelength. Average wave attributes corresponding to the time of berm erosion are shown in Table 3.2.

Table 3.2: Wave attributes associated with the time of berm erosion. † Stockdon et al. (2006) formula. ‡ Guza and Thornton (1981) formula.

Survey Date	Time(LST)	H_{mo}(m)	T_p(s)	ξ	$< \eta > (m)^{\dagger}$	$< \eta > (m)^{\ddagger}$	$R_2(m)^{\dagger}$
21 February 2012	1800-1900	0.51	11.5	0.30	0.054	0.087	0.420
7 March 2012	1700-1800	1.18	11.5	0.26	0.109	0.200	0.674
20 March 2012	1600-1700	0.61	11.5	0.37	0.078	0.104	0.486

3.3.7 Wave Runup Observations

Time lapse photography and georeferenced TLS intensity data enabled direct observation of wave runup, because wetted beach sand produces a low signal intensity. By visually matching time lapse photography with TLS data, a threshold of 10 iu was found to outline the wet/dry interface indicative of the maximum runup over the time scale of the scan. The reflected laser intensity for dry sand was found to be generally greater than 12 iu. Hence, the maximum

elevation of beach face TLS points (the scan region immediately upcoast and downcoast of the berm) with an intensity less than 10 iu was taken as an indicator of maximum runup elevation which we denote R_0. Measurement uncertainty is estimated to be $< 3cm$ based on differences in runup measurements achieved by varying the intensity cutoff by 4 iu around the 10 iu limit.

3.4 Results

The fit of front-scan to back-scan data was evaluated by comparing point elevations in the region of overlap between the two scans, generally on the beach inland of the berm. These data correspond to initial conditions prior to berm erosion. Beach elevations were sampled at 30 points within the overlap zone. For berm survey 1, height differences average 6 mm. For surveys 2 and 3 height differences average 9 and 7 mm, respectively. These values correspond to the expected TLS instrument scanning accuracy at 100 m distances.

Table 3.3: DTM errors (VRMSE) for each scan day.

Survey Date	GPS Points	Relative Error (m)	GPS Error (m)	Absolute Error (m)
21 February 2012	23	0.025	0.014	0.029
7 March 2012	50	0.022	0.014	0.026
20 March 2012	25	0.027	0.014	0.030
Average	33	0.025	0.014	0.028

Relative and absolute vertical root mean square errors (VRMSE) of the full TLS returns are presented in Table 3.3 for each of the three berms. These data show that performance of the TLS scanner was consistent across the three scanning dates, with relative and absolute errors in the range of 2-3 cm, despite significant differences in environmental conditions. Specifically, windy conditions on March 7, 2012 (9.4 m/s) caused visible aerosols and occasional vibrations of the pier with strong gusts. Both of these effects may alter light transmission and reception however, the accuracy data provide strong evidence that adverse environmental conditions did not degrade the quality of the scans. Table 3.2 shows that the three berms

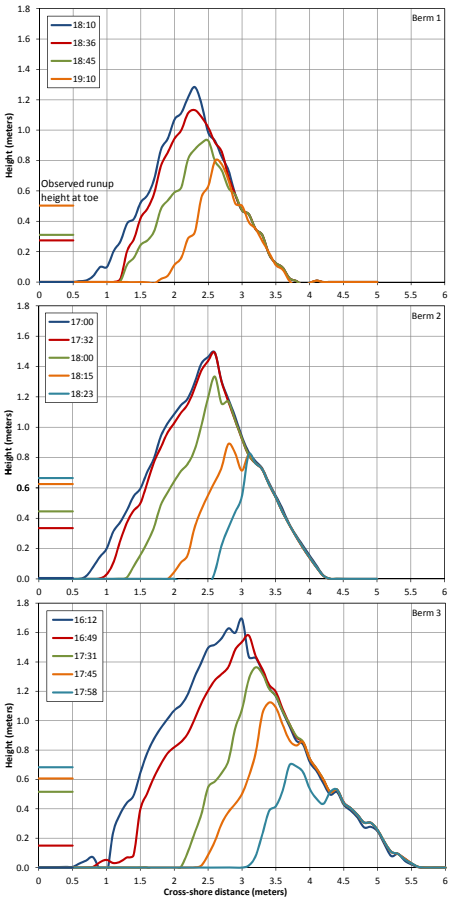

Figure 3.8: The berm cross-sectional geometry maintained a consistent shape as it was eroded. The height of the observed runup, relative to the initial height of the berm toe, indicates that the berm was eroded while only its toe was initially exposed to the rising tide and waves.

experienced a consistent wave period of 11.5 s but the wave height for Berm 2 (1.2 m) was approximately two times Berm 1 and 3 (0.5-0.6 m). Table 3.2 also shows that the Iribarren number was less than 0.4 for each case which corresponds to spilling breakers in the surf zone. Observations and time-lapse photography reveal a basic, qualitative description of berm erosion. Wave breaking occurred ca. 50-100 m offshore of the berm, resulting in irregular bores moving through the swash zone and running up and down the foreshore similar to the swash regime as described by Sallenger [2000]. With the rise of the tide, runup eventually reached the toe of the berm, analogous to the collision regime [Sallenger, 2000], causing localized soil saturation and slumping. The slumping process began slowly and accelerated as the berm was increasingly exposed to wave energy (shallow bores) and toe inundation from the rising

tide. In turn, avalanching of relatively dry sand down the angle of repose was observed as the toe was eroded. Hence, over time, the face of the berm retreated and the crest height was lowered with every avalanche that extended to the berm crest. Fig. 3.8 presents cross-shore profiles of the berm height at overtopping locations from the gridded TLS data. The height of the observed runup is also shown in Fig. 3.8, relative to the height of the berm toe. Note that the dynamic evolution of berm cross-sectional shape was consistent across all three berm prototypes: a gradual reduction in size of a triangular geometry whereby the side-slopes remained constant and the left base was translated inland. Fig. 3.9 presents the

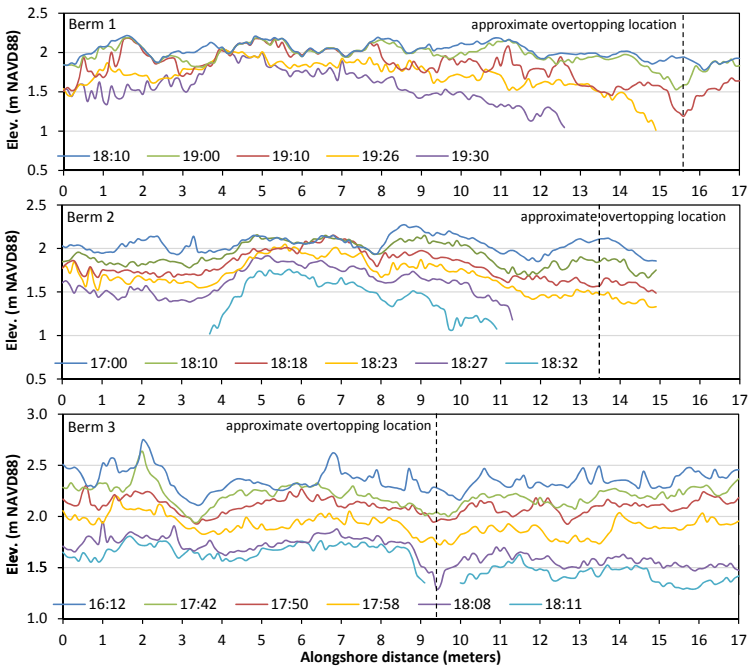

Figure 3.9: The alongshore variability in the berm crest elevation shows that Berms 1 and 2 were first overtopped near the end of the central berm section, while Berm 3 was overtopped near the center. The location of initial overtopping does not correspond to an initial low point in the berm.

along-shore profiles of the central portion of the berm crest. These profiles reveal the irregular initial shape that results from the construction process, and the downward progression of the berm height resulting from the rising tide and wave action. The alongshore patterns of erosion differed across the three berm experiments. With Berms 1 and 2, the ends of the central berm section lowered faster than the middle portion of the central section. In contrast, the central berm crest of Berm 3 was lowered relatively uniformly in the alongshore

direction. Fig. 3.9 denotes the location of initial overtopping in all three cases, as determined by a review of time-lapse photography. It is noted that overtopping does not occur at the initial berm minima (i.e., following construction), the overtopping point is an emergent feature. Fig. 3.10 shows the co-evolution of numerous system attributes. Fig. 3.10a, b and c

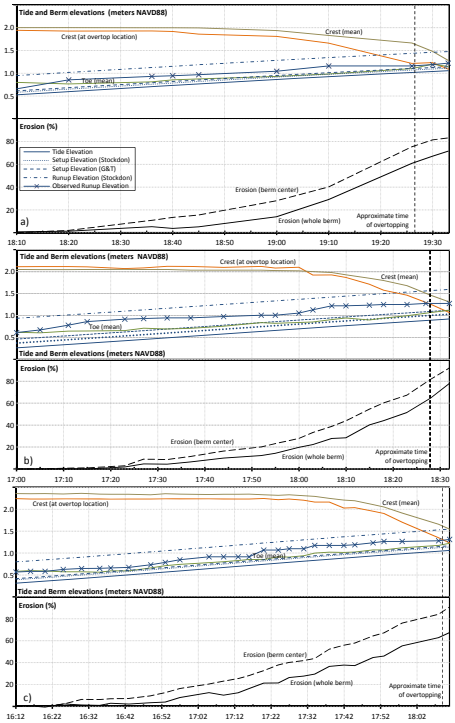

Figure 3.10: With the rising at a steady rate, the rate of berm erosion progressively increases. The pattern is repeated over three experiments as shown for a) Berm 1, b) Berm 2, and c) Berm 3. The central berm section erodes faster than the whole berm since the wings of the berm are further ashore as shown in Figure 2. Note that the observed runup (blue line) matches the crest elevation (red line) at the moment of initial overtopping.

correspond to Berm 1, 2, and 3, and each shows data on elevation (top) and berm erosion (bottom). The elevations shown include the average crest elevation, the crest elevation at the observed location of overtopping, the average toe elevation, the offshore tide elevation h, the setup elevation estimate ($< \eta > +h$), the 2% runup elevation estimate ($R_2 + h$), and the observed runup elevation ($R_0 + h$). Cumulative erosion is shown for the central berm section and whole berm (including berm wings) as measured by the berm DTM. The time of initial overtopping is indicated by a vertical dashed line. Several basic observations can be reported that apply to all three berm experiments:

- The tide rise is nearly linear in time, while the berm crest elevation and cumulative erosion are non-linear. Both respond slowly at first, and then more rapidly approaching the moment of failure.

- Setup and runup estimates rise nearly linearly in time with the tide, but observed beach runup exhibits variability that departs from a simple linear trend. The observed runup is consistently lower than estimated runup based on Eq. 3. The average deviation of computed vs observed runup is 23, 26 and 23 cm for Berms 1, 2 and 3 respectively.

- The separation between the average crest elevation and elevation at the overtopping location increases over time, indicating an accelerating breaching process similar to other types of embankment failures (e.g., Wu et al. [2011]).

- Overtopping occurred ca. 60-90 minutes before the observed beach runup elevation attains the elevation of the initial average berm crest (not shown, outside of scale), and 30-60 minutes before the estimated runup elevation attains the initial average berm crest elevation. Average berm crest elevation is lowered by erosion of the berm toe and avalanching, suggesting that berm erosion may be more highly dependent on water level than overtopping.

- Overtopping occurred when the central berm is 75-80% eroded and the whole berm is 60-65% eroded by volume.

- Eroded sediment was visually observed slumping in the seaward direction, and it appeared to spread out smoothly based on time-lapse photography. However, a precise characterization of foreshore sediment redistribution was not possible because the flooded conditions prevented TLS measurements.

3.5 Discussion

The TLS system and time-lapse photography are clearly valuable for investigations of berm dynamics. However, the TLS system used here required an hour or two to set up (including spheres, RTK-GPS ground control points, etc.), and two scans were required to characterize the initial conditions (front and back). Assuming a rapid scan using a mobile platform would be of interest, to assess initial beach profile and inform coastal flood models, and that access to the ocean side of berms is typically not possible, two issues are explored further:

- Is a single back-scan sufficient for mapping the berm crest elevation (recognizing that berm slopes are approximately equal on opposite sides)?
- Could a coarser point spacing be used to minimize the required scanning time without sacrificing overall accuracy?

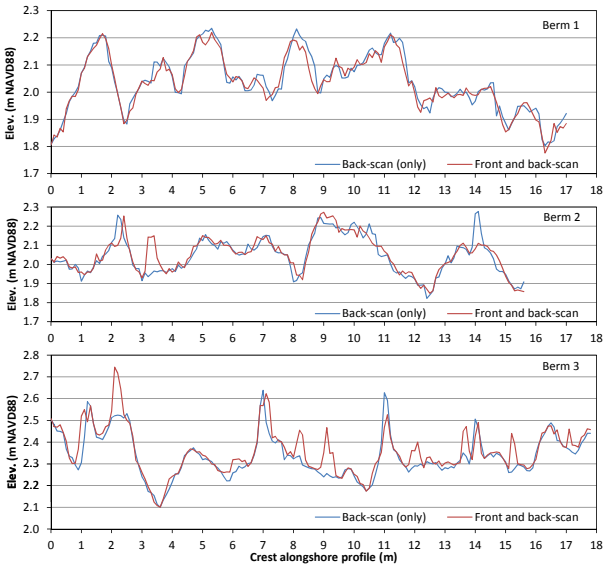

Figure 3.11: The alongshore characterization of the berm crest elevation is closely approximated by a back-scan (blue line), compared with a point cloud based on front and back scans (run line).

Fig. 3.11 presents initial berm crest elevations as determined by the back scan versus the combined (front-back) scans, and reveals a high degree of coherency. The average vertical

error between the two profiles was 0.03, 0.04 and 0.03 m (RMSE) for Berms 1, 2 and 3, respectively, which is within the absolute error of the TLS measurements. Original point cloud data contained occasional spikes in berm elevation from birds on the berm crest. If the TLS data were filtered to remove false hits, the errors would decrease even further. To answer

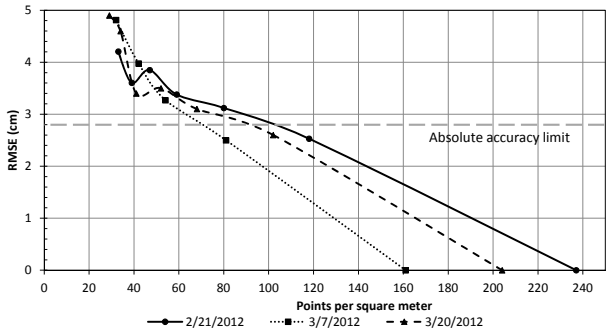

Figure 3.12: The accuracy of the DTM depends on the density of point cloud data, and by using a minimum of 100 points per square meter, the DTM error associated with the point density remains smaller than the absolute accuracy of the elevation data.

the second question, additional 7.5 cm resolution berm DTMs were computed using the same interpolation procedure (IDW) but with fewer lidar points. DTMs were computed by thinning the original lidar point clouds using a modulo operation leaving only every second, third, fourth, fifth or sixth point in the lidar point cloud. Analysis of the thinned point clouds showed the sampling of points was evenly distributed. Height differences between the undersampled and original DTMs were then measured to compute the undersampling error (VRMSE) which is shown in Fig. 3.12. This shows that the undersampling error is increased as the point density decreases, which is the expected response. We note that the total point density varies from ca. 160 to 240 m-2 across the three prototype berms due to differences in the distance between the scanner and the berm. Fig. 3.12 also shows the absolute error associated with the TLS data, 2.9 cm VRMSE, indicating that a point density of ca. 70-100 m-2 or greater is required for the undersampling error to be equal or less than the absolute error of the TLS data. Hence, the TLS scanner setting (7.5 cm) could only be increased to about 10 cm before the berm DTM errors increased beyond the accuracy of individual TLS point heights. Thus, a point spacing of 10 cm or finer is recommended for future berm

scanning studies.

In the next section, a regression analysis of erosion is presented with respect to several alternative (dimensionless) water heights. The heights include the Newport tide height, the Los Angeles tide height, the setup elevation based on [Stockdon et al., 2006] (Eq. 2) and [Guza and Thornton, 1981] (Eq. 4), the runup elevation based on [Stockdon et al., 2006] (Eq. 3), and the elevation corresponding to the observed runup.

3.5.1 Regression of Berm Erosion Data

Several dimensionless water heights were computed for erosion regression analysis. Dimensional water heights are measured relative to the initial toe elevation Z_0 and non-dimensionalized by the initial berm height B_0, which represents the difference between the initial crest and toe elevations. Each dimensionless water height can be interpreted as the fractional height by which the berm is flooded. The dimensionless tide height is based on tide elevation h as follows,

$$h^* = \frac{h - Z_0}{B_0} \tag{3.5}$$

where the superscript * denotes a dimensionless variable. The dimensionless wave setup is given by,

$$< \eta >^* = \frac{h + < \eta > - Z_0}{B_0} \tag{3.6}$$

the dimensionless wave runup is given by,

$$R_2^* = \frac{h + R_2 + Z_0}{B_0} \tag{3.7}$$

and a similar expression is used for the dimensionless observed runup,

$$R_0^* = \frac{h + R_0 + Z_0}{B_0} \tag{3.8}$$

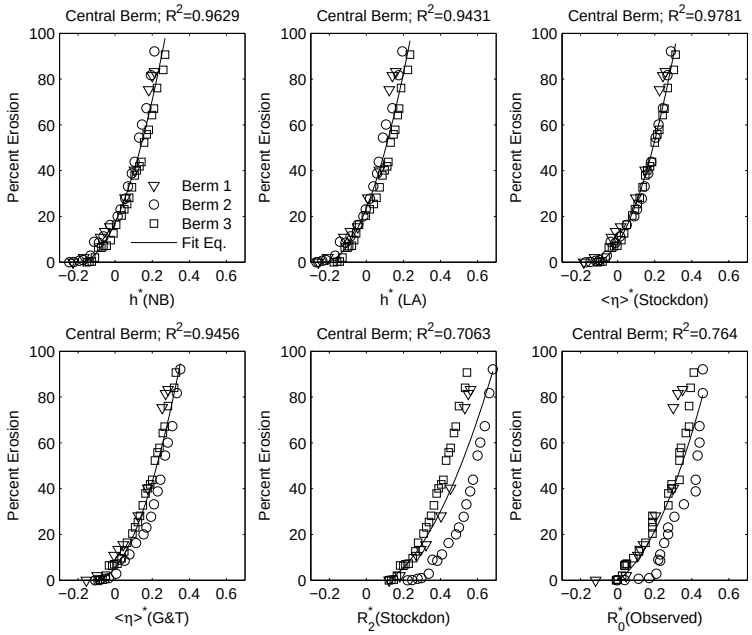

Figure 3.13: Cumulative erosion of the berm over three experiments correlates well (R2 ¿ 0.94) with dimensionless tide and setup elevations, and is poorly correlated R2 ¡ 0.77) with dimensionless runup elevations. Cumulative erosion correlates best with the dimensionless set up elevation based on the formula by Stockdon et al. [2006].

Fig. 3.13 shows the erosion data for the central section of each berm. Cumulative erosion is shown versus each of the dimensionless heights, and also shown is the least-squares fit of a quadratic model of the following form,

$$y = \{a(x - x_0) + b(x - x_0)^2 \qquad if \quad x \geq x_0 \quad ; or \quad 0 \qquad if \quad x \geq x_0\} \tag{3.9}$$

where x represents the abscissa (dimensionless water level) and y represents the ordinate (cumulative berm erosion expressed as a percentage). The quadratic model given by Eq. 9 is fit subject to the constraint, $y \geq 0 \ \forall x$, to guarantee a monotonic increase in cumulative erosion with increasing water levels.

Table 3.4: Quadratic model parameters and coefficient of determination. † Stockdon et al. (2006) formula. ‡ Guza and Thornton (1981) formula.

	Central Berm				Whole Berm			
Predictor	x_o	a	b	R^2	x_o	a	b	R^2
$h^*(NB)$	-0.193	2.510	453.0	0.963	-0.138	-0.320	467.5	0.918
$h^*(LA)$	-0.230	-0.302	447.2	0.943	-0.175	0.624	447.9	0.889
$<\eta>^*$ †	-0.131	0.000	484.4	0.978	-0.0681	-0.463	526.0	0.948
$<\eta>^*$ ‡	-0.113	-0.906	441.6	0.946	-0.044	-0.850	490.3	0.943
R_2‡	-0.159	-54.32	193.6	0.706	0.074	-10.10	213.7	0.713

Fit parameters are shown in Table 4 and the results are plotted in Fig. 3.13. All of the regressions yield a high value for the coefficient of determination ($R^2 > 0.7$), and the fit is generally better for the central berm data than the whole berm data. The dimensionless Stockdon setup ($<\eta^*>$) represents the best fit for both the central berm ($R^2 = 0.978$) and whole-berm data ($R^2 = 0.948$), but the fit based on all tide and setup heights is excellent ($R^2 > 0.89$). On the other hand, poorest fit (R^2 0.7) is associated with dimensionless runup heights ($R_2^* and R_0^*$). Fig. 3.13 suggests the relatively poor fit is attributable to Berm 2, which is offset from the other two berms in the panels corresponding to observed runup height, predicted runup height and the Guza and Thornton setup height. Berm 2 experienced the largest waves of the three test cases, so the comparatively weak regression with runup may indicate that waves are not controlling erosion. Instead, these results suggest that berm erosion is controlled by its degree of submergence indicated best by the Stockdon et al. [2006] setup height, and leave open the possibility that wave action is important for agitating or destabilizing the berm toe and moving material away down the shore face. Previous work has also indicated that erosion is linked to water level [Basco and Shin, 1996].

The berms were observed to be stable after construction, and erosion only began after water came in contact with the berm. Therefore, the fit model given by Eq. 9 is designed with a parameter representing the threshold for erosion, x_0. Depending on the regression, x_0 was found to vary from -0.23 to 0.074 which can be interpreted as a water level 23% below or 7.4% above the toe of the berm, relative to the initial height of the berm. Using the scaled

[Stockdon et al., 2006] water level, x0=-0.131 indicating that berm erosion begins when the setup elevation is about 13% below the berm toe elevation, relative to the initial berm height. Previously it was noted that berm overtopping occurred when the central berm section was 75-80% eroded. Based on Figure 10, this occurs when the scaled [Stockdon et al., 2006] water level is in the range 0.25-0.30. This indicates that the erosion is initiated and completed as the water level rises from 13% below to 25-30% above the initial toe elevation, respectively, relative to the height of the berm.

This simple scaling was exceptionally consistent over all three berms and may represent a rapid method of predicting triangular berm failure onset and by extension, flood risk, for a specific site under similar wave conditions. However, it is important to note however that the regression equations may not be applicable at other locations, to other berm geometries, or even to the same site under different wave conditions. For example, the Iribarren number was less than 0.4 for all experiments which corresponds to spilling breaker types, and the erosion mechanism may be different when other breaker types are present.

3.6 Conclusion

TLS delivers an accurate model of the berm geometry. A comparison with ground control points reveals an average error of 2.5 cm (VRMSE) over three berm prototypes, and a high level of consistency across prototypes despite one case of strong, gusty winds that represent more challenging scanning conditions. TLS also provides signal intensity data that is strongly linked to moisture content.

The TLS was operated with a point spacing of 7.5 cm at a distance of 100 m, leading to average point densities of 160-240 m-2. Differences across the three berms were the result of slightly different scanner and berm positions across the three prototypes. Analysis of the

TLS data suggests that berm geometry could be mapped at the same level of accuracy with a resolution as large as 10 cm. At this resolution, uncertainty in the berm elevation associated with under-sampling would be equal to the expected error of the TLS data compared with the ground control points. This result suggests that there is relatively little margin for increasing the lidar point cloud spacing without increasing the absolute error of the berm height data beyond ca. 3 cm.

Berm crest elevations estimated using only back scan data compare favorably with berm crest elevations estimated from combined front and back scans. Recognizing that a rapid scan of beach berms could help to inform coastal flood prediction models, scanning from the back-side may represent an efficient proxy for berm elevation or maximum beach crest for rapid overtopping probability assessment.

Continuous lidar scanning and time-lapse photography of anthropogenic beach berms exposed to a rising tide and waves leads to a four dimensional empirical model of berm dynamics. For the site considered and the three days tested, a relatively simple erosion pattern was observed: As runup first strikes the toe of the berm, berm sediment saturates and begins to slump. With continued slumping and offshore sediment transport by wave action, avalanching occurs down the angle of repose causing the retreat of the berm face inland and a progressive loss of sand and lowering of the crest elevation. The rise of the tide was nearly linear in time over the duration of berm erosion, and the erosion and lowering of the beach crest was non-linear with time and characterized first by a gradual and then by a rapid change. A dimensionless setup elevation representing the fractional submergence of the berm is identified as a good predictor of cumulative berm erosion under the test conditions. Across the three berm experiments, erosion of the central berm section begins when the setup elevation is about 13% below the toe of the berm, relative to the initial berm height, and the berm is overtopped when the setup elevation is 25-30% of the initial berm height and the berm is 75-80% eroded by volume.

Chapter 4

Multi-Phase Shock-Capturing Model of Beach Hydromorphodynamics

This Chapter has been submitted to Journal of Coastal Engineering. Citation: Majd, M.S., Gallien,T.W., Schubert, J.E. and Sanders, B.F. (2015), Multi-Phase Shock-Capturing Model of Beach Hydromorphodynamics, *Journal of Coastal Engineering*, *In Review*.

4.1 Introduction

Human coastal migration and sea level rise acceleration are increasing flood and erosion risks at an alarming rate [Nicholls, 2011, Hanson et al., 2011]. Many communities are currently guarded from flooding by beaches that are enhanced with anthropogenic berms [Wells and McNinch, 1991, Clark, 2005, Carley et al., 2010, Rogers et al., 2010, Kratzmann and Hapke, 2012, Harley and Ciavola, 2013, Gallien et al., 2015], so understanding beach and berm response to storm waves is critical to adapting and mitigating climate change effects. Calibrated swash-zone models initialized with timely beach profile measurements and forced by tide, storm surge and wave predictions could offer valuable information for flood preparedness, mitigation and emergency response: predictions of the timing, location and magnitude of overtopping flows.

Beaches present numerous hydromorphodynamic modeling challenges including wave dynamics, sediment transport and shoreline movement [Larson et al., 2004, Brocchini and Dodd, 2008, Briganti and Dodd, 2009a]. The non-linear shallow-water (NLSW) equations offer a reasonable approximation of swash zone flows from the mid- to inner-surf zone shoreward [Brocchini and Dodd, 2008], and form the basis of contemporary beach morphodynamics models such as XBeach [Roelvink et al., 2009] and XBeach-G [McCall et al., 2014]. Recent NLSW models include non-hydrostatic terms, improving wave dispersion characteristics in intermediate and deep water [Zijlema et al., 2011, McCall et al., 2014, Masselink et al., 2014], but at significant computational expense. Consequently, practical coastal flood prediction applications often favor use a spectral wave model such as SWAN [Booij et al., 1999] to predict the wave spectrum at a shallow depth, which is in turn transformed into a time series of water surface height that is specified as the boundary condition of a hydrostatic NLSW model [McCabe et al., 2011]. By coupling the NLSW model to an Exner equation through a Bagnold-type sediment transport equation, the horizontal and temporal distribution of the instantaneous water surface height, depth-averaged velocity, sediment concentration, and

sediment bed height can be predicted. This approach can be contrast with models designed to predict wave-group averaged flow and sediment transport [e.g., Roelvink et al., 2009], and also with probabilistic models that are based on wave energy balance concepts [e.g., van Rijn, 2009]. XBeach-G [McCall et al., 2014, 2015] is an example of a mechanistic model for instantaneous flow and sediment prediction in shallow and intermediate depths that can be forced by a time series of water level, as conceived by [McCabe et al., 2011], based on the wave energy spectrum [Roelvink et al., 2009]. McCall et al. [2014] refer to mechanistic modeling of instantaneous conditions in the swash zone as *wave by wave* modeling, although this terminology was historically used to describe models that followed the trajectory of individual waves progressing through the swash zone and used empirical models to account for wave transformation [e.g., Dally, 1992]. Mechanistic wave by wave modeling is the focus of this paper.

Shock-capturing numerical methods have proven very successful for mechanistic wave by wave modeling in the swash zone [Hubbard and Dodd, 2002, Briganti and Dodd, 2009a]. The most robust shock-capturing shallow-water models for hydromorphodynamics, sometimes known as shock-capturing debris flow models, are derived from vertically integrated multi-phase flow equations that account for the effects of suspended sediment on inertia and momentum fluxes and are therefore valid for hyperconcentrated flows [e.g., Fraccarollo et al., 2003]. Shock-capturing capability is the result of using a Godunov-based finite volume scheme with an approximate Riemann solver to compute fluid mass, sediment mass, and momentum fluxes. A conditionally stable monotone solution update is achieved using a semi-implicit corrector step that synchronizes predictions of velocity, sediment concentration, and sediment bed height [Armanini et al., 2009, Soares-Frazao and Zech, 2011, Majd and Sanders, 2014]. Several lines of evidence suggest that a multi-phase shock-capturing model could be advantageous in swash zone applications. For example, there is the persistent occurrence of shock waves (bores) and transient wet/dry fronts [Brocchini and Baldock, 2008], and field and laboratory studies show that sediment concentration spikes occur on beaches

during uprush and downrush [Puleo et al., 2003]. Additionally, McCall et al. [2015] recently reported improved predictions after considering the effect of sediment on inertia. There are also reports that dike/dune failure models need to cope with high sediment transport rates [Van Emelen et al., 2012].

This paper presents a Multi-Phase, Shock-Capturing (MPSC) numerical model for mechanistic wave by wave modeling of flow, sediment transport, and beach profile change in shallow depths and the capacity to simulate rapid beach erosion and overtopping which is important for coastal flood prediction. The model accounts for the effect of sediment on inertia and momentum fluxes in a systematic way and can describe hyperconcentrated flows, spikes in sediment concentration, and shocks in the flow and sediment profile. The MPSC model solves vertically integrated multi-phase flow equations using a Godunov-type numerical method known as the LHLLC (Lateralized Harten, Lax and van Leer + Contact discontinuity) scheme, and similar to other models developed for beaches [e.g., Roelvink et al., 2009], the MPSC model includes an avalanching scheme for gravitational slumping of steep slopes [Majd and Sanders, 2014]. A diffusive sediment flux that was initially developed for debris flow modeling is also used here to increase or decrease sediment transport rates depending on whether flow is in the downslope or upslope direction, respectively [Rosatti and Begnudelli, 2013]. The diffusive flux is termed Slope Assisted Transport (SAT) because it mimics gravitational effects that preferentially move suspended sediment in the downslope direction [Rosatti and Begnudelli, 2013]. This paper also describes how the MPSC model is coupled to a spectral wave model to account for neashore wave transformations, and the sensitivity of the model to placement of the MPSC offshore boundary is examined as well as stochastic variability introduced when wave spectrum are converted to time series of water height. The objective of this paper is to present the MPSC model equations and numerical methods (Section 2 and 3), evaluate model performance in one-dimensional (1D) applications (Section 4), and report on model suitability for coastal applications based on factors such as accuracy, stability and computational cost (Sections 5 and 6).

4.2 Governing Equations

The MPSC model conceptualizes the swash zone as a one layer fluid-sediment mixture with depth h_m, velocity u_m and concentration by volume c which sits upon a sediment bed with concentration by volume c_b and a height of z_b above an arbitrary datum, as shown in Fig. 4.1. Note that the height of the mixture surface above an arbitrary datum is given by z_w=z_b+h_m.

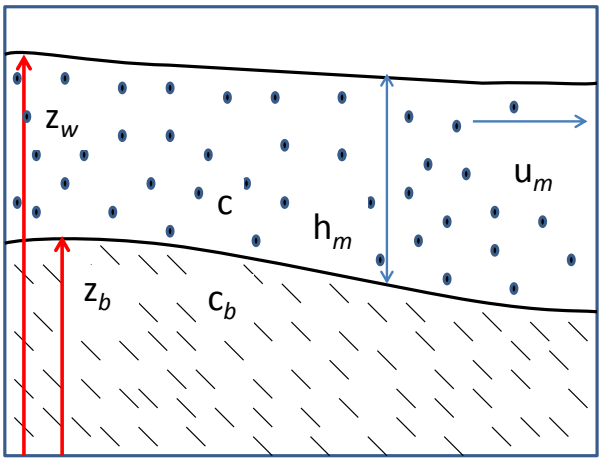

Figure 4.1: The MPSC model assumes a fluidized layer of thickness h_m, sediment concentration c, and velocity u_m over an erodible sediment bed with height z_b and concentration c_b. Note that z_w=z_b+h_m.

Debris flow models have also been developed with multiple layers of fluid and sediment [e.g., Chen and Peng, 2006b], but this introduces more parameters and requires the solution of more equations which increases both model complexity and computational costs [Majd and Sanders, 2014], motivating the relatively simple formulation presented here. An attractive feature of the model is that hyperconcentrated near-bed sediment layer (bed load) thickness can be recovered from the numerical solution using an analytical transformation [Majd and Sanders, 2014].

The governing equations consist of three partial differential equations and an algebraic sediment transport equation. The partial differential equations account for continuity of the fluid mixture, continuity of sediment, and momentum of the mixture and are presented in a

compact, matrix form,

$$\frac{\partial \mathbf{U}}{\partial t} + \frac{\partial \mathbf{F}}{\partial x} + \mathbf{H}\frac{\partial z_b}{\partial x} = \mathbf{S} \tag{4.1}$$

where

$$\mathbf{U} = \begin{pmatrix} h_m + z_b \\ ch_m + c_b z_b \\ (c\Delta + 1)u_m h_m \end{pmatrix}, \mathbf{F} = \begin{pmatrix} u_m h_m \\ cu_m h_m \\ (c\Delta + 1)(u_m^2 h_m + \frac{1}{2} g h_m^2) \end{pmatrix}, \tag{4.2}$$

$$\mathbf{H} = \begin{pmatrix} -k|u_m|h_m \\ -\alpha c_b k|u_m|h_m \\ (c\Delta + 1)gh_m \end{pmatrix}, \mathbf{S} = \begin{pmatrix} 0 \\ 0 \\ -f|u_m|u_m \end{pmatrix} \tag{4.3}$$

where $\Delta = (\rho_s - \rho_w)/\rho_w$, ρ_s and ρ_w represent solid and water densities, respectively, f is a dimensionless friction factor, k is a dimensionless SAT parameter, and α represents the ratio of the near bed to packed bed sediment concentration. The appearance of sediment concentration, c, in the momentum equation reflects a tight coupling between sediment transport and wave action, which makes the model valid for applications involving hyperconcentrated sediment mixtures. Eqs. 4.1 assume that shear stress at the sediment-water interface is given by,

$$\tau = f\rho_w u_m^2 \tag{4.4}$$

which implies that f is related to the Darcy-Weisbach friction factor f_{DW} by $f = f_{DW}/8$ [Henderson, 1966]. The algebraic sediment transport equation describes the total sediment load q_s under the assumption of instantaneous energetics as follows [Bailard, 1981, Rosatti et al., 2008, Armanini et al., 2009],

$$q_s = cu_m h_m = c_b \beta u_m^3 \tag{4.5}$$

where β is an empirical entrainment factor. Note that Eq. 4.5 is an approximation that has been found adequate for many beach applications despite theoretical limitations [Masselink and Russell, 2006]. For example, field experiments show that uprush and downrush may be characterized by different values of β [Larson et al., 2004]. Additionally, Masselink and Russell [2006] suggest that β values are sensitive to experimental measurement methods and data analysis techniques and Puleo et al. [2005] report that β values are sensitive to calibration procedures. Here as in many previous studies, β is treated as a constant for a particular beach and is viewed as a calibration parameter. It is expected that the calibrated value will fall close to the range of experimentally measured values.

Note that the first two terms in the vector $\mathbf{H}$ correspond to fluxes of the mixture and sediment, i.e., SAT terms, that are scaled by the local beach slope (Eq. 1), while the third term accounts for the traditional beach slope source term in the momentum equation. Rosatti and Begnudelli [2013] recommend use of α=0.9 for SAT, which is adopted for this study. The SAT dimensionless parameter k scales the magnitude of the SAT flux which is expected to be much smaller than the advective flux, i.e., $k \ll 1$. The purpose of SAT, as will be shown in the results, is to smooth out overly steep sediment fronts that are predicted to occur under the assumption of instantaneous energetics when beach sediments are eroded and transported in the offshore direction by the model. Hence, SAT may partially compensate for limitations associated with instantaneous energetics and the layer-averaged approximation of the flow. It is also noted that f can be informed by grain size, but it is difficult to precisely estimate and therefore may also be used as a calibration parameter that is constrained by a range of physically reasonable values dictated by the beach material.

Eqs. 4.1 are hyperbolic with three characteristic wave speeds (or eigenvalues) corresponding to forward and backward moving gravity waves, λ_1 and λ_3, and a contact discontinuity, λ_2. The wave speeds cannot be expressed in a simple analytical form like the classical shallow-water equations which have a Jacobian matrix with eigenvalues given by $u+\sqrt{gh}$, u, and

u-$\sqrt{gh}$. Rather, the wave speeds are defined by the three roots of a cubic characteristic polynomial and must be computed numerically [Majd and Sanders, 2014]; fortunately, an explicit routine avoids the need for a costly iterative search algorithm [Majd and Sanders, 2014]. For this model, the wave speeds are calculated under the assumption that k=0, since in practice the model uses small k values and this assumption leaves the characteristic polynomial unchanged compared to proven debris flow models [Majd and Sanders, 2014]. The wave speeds are important for implementing the numerical solver, as shown in the next section.

4.3 Numerical Solver

The MPSC model uses the LHLLC scheme previously developed for debris flow modeling [Majd and Sanders, 2014] and is modified here to account for SAT fluxes and an oscillatory boundary condition representative of wave dynamics. The spatial domain is discretized into N cells of size Δx, the solution is evaluated at the center of each cell, $\mathbf{U}_i$, for $i = 1, \ldots, N$, and fluxes are evaluated at the edges between cells as is customary with finite volume schemes.

The LHLLC scheme sequentially updates U_1, U_2 and U_3 in each computational cell, i.e., the three elements of the solution vector $\mathbf{U}$. Hence, each step is presented in turn. The fluid mixture continuity equation is updated as follows,

$$(U_1)_i^{n+1} = (U_1)_i^n + \frac{\Delta t}{\Delta x}\left[(F_1)^*_{i-1/2} - (F_1)^*_{i+1/2}\right] \tag{4.6}$$

where $(F_1)^* = F_1 + H_1 \partial z_b/\partial x$ and is computed by applying the HLL scheme for F_1 and a central difference approximation for $\partial z_b/\partial x$ as follows,

$$(F_1)^* = \frac{S_R F_{1L} - S_L F_{1R} + S_R S_L (U_{1R} - U_{1L})}{S_R - S_L} + H_1 \Delta z_b/\Delta x \tag{4.7}$$

where S represents wave speed, the subscripts L and R denote the cells to the left (i) and right ($i+1$), respectively, of an arbitrary edge index ($i+1/2$). The wave speeds are computed as follows [Fraccarollo et al., 2003],

$$S_L = \min(\lambda_{1L}, \lambda_{1R}) \tag{4.8}$$

$$S_R = \max(\lambda_{3L}, \lambda_{3R}) \tag{4.9}$$

where λ_{1L} and λ_{1R} represent values of λ_1 in the left and right cells, respectively. The same convention applies to λ_3. It is noted that at the beginning of each time step, wave speeds are computed in each cell by solving for roots of a cubic polynomial [Majd and Sanders, 2014]. This enables flux calculations to proceed using Eq. 4.7. The SAT mixture flux is computed by evaluating elements of H_1 at the interface between cells as the average of values in neighboring cells, e.g., $(u_m)_{i+1/2} = \frac{1}{2}[(u_m)_{i+1} + (u_m)_i]$, and by computing $(\Delta z_b)_{i+1/2} = (z_b)_{i+1} - (z_b)_i$. Note that the source term in the mixture continuity equation is zero (cf. Eqs. 4.3), so discretization is not required.

The sediment continuity equation is updated in a similar fashion to the mixture continuity equation as follows,

$$(U_2)_i^{n+1} = (U_2)_i^n + \frac{\Delta t}{\Delta x}\left[(F_2)^*_{i-1/2} - (F_2)^*_{i+1/2}\right] \tag{4.10}$$

but instead of using an HLL solver to compute the flux, an HLLC scheme similar to Goutire et al. [2008] is used to minimize numerical diffusion [Majd and Sanders, 2014]. Using HLLC, the flux equation depends on whether the mixture flux is positive or negative. When $(F_1)^* \geq 0$, flow is in the positive x direction and the solid flux is computed as,

$$(F_2)^* = \frac{S_S F_{2L} - S_L F_{2R} + S_S S_L (U_{2R} - U_{2L})}{S_S - S_L} + H_2 \Delta z_b / \Delta x \tag{4.11}$$

where S_L is computed as before and S_S is computed from the speed of contact discontinuities (λ_2) in neighboring cells as follows,

$$S_S = \text{maxmod}(\lambda_{2L}, \lambda_{2R}) \tag{4.12}$$

and the function maxmod() returns the signed argument with the largest absolute value. Additionally, H_2 is computed with the same scheme used for H_1 in Eq. 4.7. On the other hand, when $(F_1)^* < 0$, the solid flux is computed as follows Majd and Sanders [2014],

$$(F_2)^* = \frac{S_R F_{2L} - S_S F_{2R} + S_R S_S (U_{2R} - U_{2L})}{S_R - S_S} + H_2 \Delta z_b / \Delta x \tag{4.13}$$

where S_S and S_R are computed as before.

Before the solid flux is used to update Eq. 4.10, a limiting function is applied to prevent the magnitude of the solid flux F_2^* from exceeding the magnitude of the mixture flux F_1^*, as this would give non-physical predictions [Majd and Sanders, 2014]. The limiting is expressed as follows,

$$(F_2)^*_{i+1/2} = \text{maxmod}[(F_1)^*_{i+1/2}, (F_2)^*_{i+1/2}] \tag{4.14}$$

Finally, the momentum equation is updated using the LHLL scheme [Fraccarollo et al., 2003] in a two-step process as follows [Majd and Sanders, 2014],

$$(U_3)^*_i = (U_3)^n_i + \frac{\Delta t}{\Delta x}\left[(F_3)^{*R}_{i-1/2} - (F_3)^{*L}_{i+1/2}\right] \tag{4.15}$$

$$(U_3)^{n+1}_i = (U_3)^*_i + \Delta t (S_3)^{n+1}_i \tag{4.16}$$

In the first step given by Eq. 4.15, the superscripts L and R represent adjustments to the

fluxes F_3 that account for bed slope effects expressed by $H_3 \partial z_b / \partial x$ in Eq. 4.1. The adjusted fluxes include so-called lateralization terms and are given by,

$$(F_3)^{*L} = (F_3)^* - \delta_L \qquad (F_3)^{*R} = (F_3)^* - \delta_R \tag{4.17}$$

where the lateralization terms are given by,

$$\delta_{L,R} = \frac{S_{L,R}}{S_R - S_L} \frac{1}{2} (H_{3L} + H_{3R}) \left(z_{bR} - z_{bL} \right) \tag{4.18}$$

and the standard HLL flux is computed as follows,

$$(F_3)^* = \frac{S_R F_{3L} - S_L F_{3R} + S_R S_L (U_{3R} - U_{3L})}{S_R - S_L} \tag{4.19}$$

The second step of the momentum update, Eq. 4.16, is solved after rearranging it into a cubic equation for $(u_m)_i^{n+1}$, which is in turn solved using an explicit cubic equation solver precisely as shown for the LHLLC scheme [Majd and Sanders, 2014]. This represents the semi-implicit feature of the solution update, because here the model simultaneously solves for velocity, sediment concentration and friction. This key step promotes a stable and monotonic solution update without requiring costly iterations typically associated with implicit schemes.

4.3.1 Offshore Boundary Implementation

The MPSC model domain is restricted to relatively shallow depths along the shoreline as conceived by McCabe et al. [2011], and the location of the offshore boundary deserves careful consideration. On the one hand, the boundary should be in relatively shallow water where wave action is reasonably approximated by a hydrostatic flow model. On the other hand, the boundary needs to be in relatively deep water to implement a non-reflecting boundary

condition which requires subcritical flow that is free of shock waves [Hu et al., 2000]. A relatively deep offshore boundary is also needed to ensure that the model domain encompasses the region where sediment is mobile within the time frame of interest. Hu et al. [2000] found that a NLSW model successfully predicted wave runup and overtopping of structures with the offshore boundary placed outside the point of wave breaking, i.e., at an intermediate depth, so there is limited evidence to suggest that NLSW models can be extended outside the limits of hydrostatic flow without overly sacrificing predictive skill. Here, placement of the offshore boundary is approached on a case by case basis and the product $k_w h_m$, where k_w is the wave number, is used to indicate the shallowness of wave conditions. "Shallow" depths correspond to $k_w h_m$ values significantly less than unity.

Numerical implementation of the offshore boundary condition follows previous approaches for hyperbolic equations, i.e., consideration of wave characteristics, and is also designed to prevent non-physical reflections when waves exit the domain [Ozkan-Haller and Kirby, 1997, Hu et al., 2000, Sanders, 2002]. A non-reflecting boundary flux function designed for Godunov-type schemes is used, specifying the shoreward moving waves while permitting wave reflections to freely exit the domain [Sanders, 2002]. The flux function assumes the solution state at the boundary is defined by the interaction of incoming and outgoing Riemann invariants [Sanders, 2002]. The incoming Riemann invariant is calculated by assuming that the specified wave enters a region of undisturbed fluid, and the outgoing Riemann invariant is based on the solution state in the first interior cell. The boundary water surface height and velocity are thus computed from the interaction of the incoming and outgoing Riemann invariants [Sanders, 2002]. Furthermore, the initial sediment height at the offshore boundary is specified when the inflow velocity is positive, while the sediment height at the boundary is based on the first interior cell when the velocity is negative (offshore). Simplified Riemann invariants based on the classical shallow water equations (not multi-phase flow equations) are used at the offshore boundary because here sediment concentrations are small and have little impact on wave dynamics.

4.3.2 Stability Condition

The MPSC model is first order accurate in space and time and stability is contrained by a Courant-Friedrichs-Lewy condition as follows,

$$Cr = \frac{\lambda_{\max}\Delta t}{\Delta x} \leq 1 \tag{4.20}$$

where Cr represents the Courant number and $\lambda_{\max}$ represents the maximum wave speed magnitude of the solution. The explicit discretization of the SAT terms also introduces a second stability constraint which is not easily determined analytically but can be approximated as follows,

$$k|u_m|h_m\frac{\Delta t}{\Delta x^2} \leq \frac{1}{2} \tag{4.21}$$

based on the well-known stability limit of a first order in time, second order in space, explicit scheme for solving the diffusion equation. In the test cases considered here, Eq. 4.20 was found to be more restrictive than Eq. 4.21 and therefore sufficient for ensuring numerical stability. Note that because friction and sediment are discretized in a semi-implicit way when the momentum equation is updated, these effects do not control the stability of the model.

4.3.3 Avalanching Scheme

Avalanching schemes accounting for gravitational slumping of overly steep and unstable slopes are common in coastal morphodynamic modeling [e.g., Roelvink et al., 2009], and in river morphodynamic modeling [Swartenbroekx et al., 2010a]. These schemes test for critical slope (angle of repose) exceedances at each time step. When overly steep slopes are detected, sediment is redistributed along the angle of repose. A scheme that allows for two separate

critical slopes corresponding to subaerial (or dry) and subaqueous (wet) sediment is used in this study [Majd and Sanders, 2014].

4.4 Applications

Several applications involving relatively rapid erosion are presented to examine MSPC model performance including an assessment of accuracy and sensitivity to parameters. First, the Carrier and Greenspan [1958] long-wave test problem is presented for model *verification*, i.e., to show that the model converges to the exact solution of the differential equations at the expected rate based on the formal, first order accuracy of the scheme. This test case is then repeated assuming highly mobile sediment to qualitatively examine coupled solutions of the water surface, velocity, sediment concentration, and sediment profiles.

Next, focus turns to *validation* of the model for rapid erosion. Here, *validation* refers to the process by which a numerical model is shown to adequately represent experimentally observed dynamics. This involves contending with structural model errors, such as limitations of instantaneous energetics theory, in addition to numerical errors. Validation of the model is addressed first using large-scale Delta Flume experimental results [van Gent et al., 2008] with a prominent beach scarp (near vertical face). This test case measures the ability of the model to predict shoreward migration of the beach scarp and the offshore transport of eroded sediment. Secondly, the model is validated with a set of three field-scale tests involving the erosion of anthropogenic berms constructed on the foreshore of Newport Beach, California [Schubert et al., 2014]. In southern California, berms made of unconsolidated beach sand roughly 1-3 m high are routinely used to guard against coastal flooding [Gallien et al., 2015], so this test has flood risk implications in this region in addition to scientific value. The Newport Beach tests are also used to study the sensitivity of model predictions to the placement of the offshore boundary and the sample-to-sample variability arising from the

stochastic water level time series specified at the offshore boundary of the MPSC model.

4.4.1 Carrier and Greenspan Problem

The long wave runup and rundown solution presented by Carrier and Greenspan [1958] is a classic test case for shallow-water hydrodynamic models that has been used for model verification [e.g., Bradford and Sanders, 2002]. The problem is defined by a mound of water with zero horizontal velocity on a sloping but frictionless and non-erodible bottom profile, as shown in Fig. 4.2, which leads to runup and rundown in succession and allows the performance of the model to be examined in the presence of wetting and drying, strong pressure gradients and inertial effects.

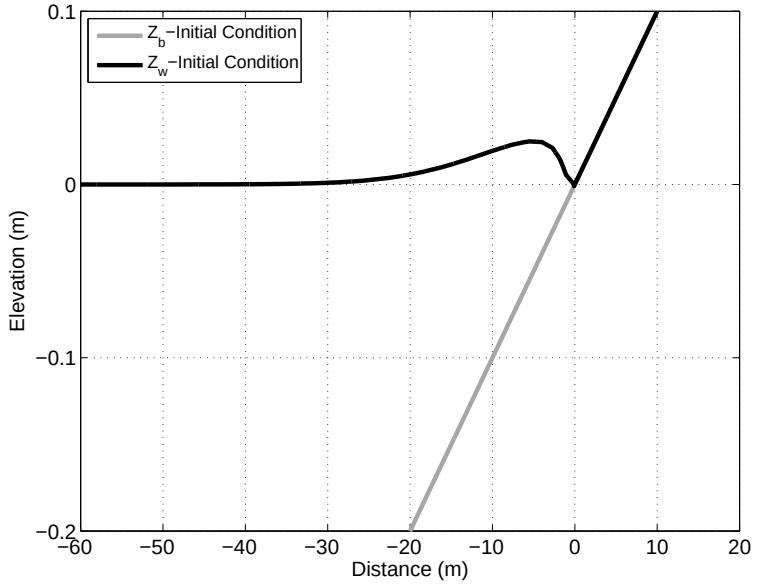

Figure 4.2: Initial condition for the Carrier and Greenspan [1958] long wave runup test case.

The test case is set up with a domain length of 100 m and a beach slope of 0.01. The model is applied with a uniform grid resolution of Δx=0.125 m and a time increment of Δt=0.0125 s. The non-erodible bed is modeled by setting $\beta = 1.25 \times 10^{-9}$ (a very small number) and the frictionless bed is achieved by setting $f = 0$. Model errors are measured using an L_1 norm which computes the difference between a discrete model prediction v_i and a reference

solution $\hat{v}_i$, as follows,

$$L_1(v) = \frac{1}{N} \sum_{i=1,N} |v_i - \hat{v}_i| \tag{4.22}$$

where v_i represents the numerical solution and and $\hat{v}_i$ is the reference solution, in this case the exact solution.

Table 4.1: Model errors in Carrier and Greenspan [1958] test case.

Water Surface Prediction at	L_1(m)
t=10 s	6.7057×10^{-5}
t=20 s	1.4580×10^{-4}
t=30 s	2.7335×10^{-4}
t=40 s	3.7504×10^{-4}

Fig. 4.3 compares water surface height predictions with the exact solution at four times, t=10, 20, 30 and 40 s, and L_1 norms are presented in Table 4.1. The accuracy of the model is qualitatively excellent; tracking the wet/dry interface (shoreline) is arguably the most challenging aspect of the test problem and at each time the prediction compares very closely with the exact solution. The largest errors appearing in 4.3 occur where the wave profile is steepest ($x \sim$ -5 m at 30 s and $x \sim$ -10 m at 40 s).

The convergence of the scheme is measured by successively halving the grid size and time step and computing the L_1 error norm in water surface height at t=40 s for each case. Fig. 4.4 shows that model errors geometrically decay with grid refinement, which is the desired result of a numerical model. The convergence rate is estimated to be 0.8 based on the linear slope of the errors on the log-log scale, which is close to the ideal value of unity for a first order scheme, and typical of a test problem with a wet/dry interface.

The Carrier and Greenspan verification test builds confidence that the MPSC model has good convergence properties in the absence of sediment mobility, but in the presence of wave uprush and downrush and a relatively steep wave front. Further confidence in the

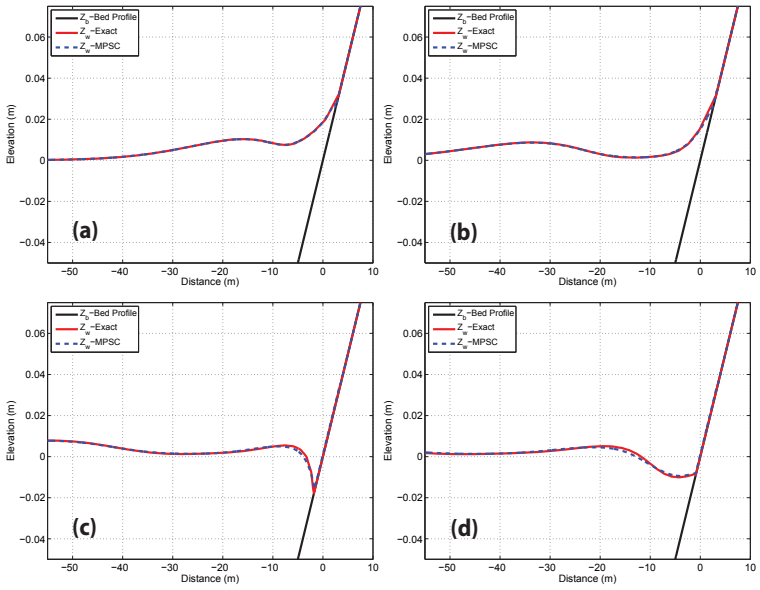

Figure 4.3: Comparison of model prediction and exact solution to Carrier and Greenspan [1958] test case at: (a) t=10 s, (b) t=20 s, (c) t=30 s, and (d) t=40 s.

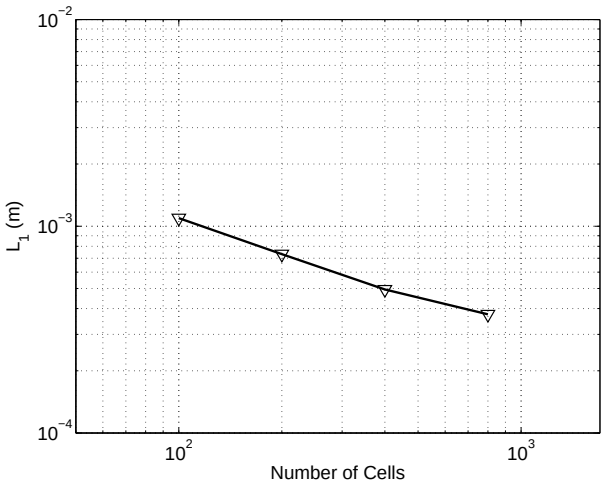

Figure 4.4: Numerical errors in Carrier and Greenspan [1958] test case geometrically decay with grid refinement (based on solution at t=40 s).

convergence properties of the model can be drawn from classical dam-break tests presented by Majd and Sanders [2014].

4.4.2 Carrier and Greenspan Problem with Mobile Sediment

The Carrier and Greenspan problem is now repeated under the assumption of a frictional beach with mobile sediment. This is achieved with the following parameter values: β=0.5, f=0.024, $k = 0$, Δ=1.60, and c_b=0.50 while the domain length, grid spacing and time increment are the same as the previous case. An unrealistically high value of β for beach sands is used here to demonstrate that the model can easily cope with high sediment concentrations and rapid changes in the beach profile.

Fig. 4.5 shows predictions of the free surface and sediment level, mixture velocity and sediment concentration at four times: 15, 30, 45 and 60 s. This result shows dramatic changes in bed profile over a very short period of time. At 15 s, the uprush phase is nearing its end with positive (shoreward) velocities between x=0 and 2 m, and negative velocities elswhere. A small spike in sediment concentration is predicted to occur near the sediment/water interface. Additionally, a small amount of sediment deposition (difference between dashed and solid gray line) is predicted between x=0 and 2 m while a relatively small amount of erosion is predicted between x=-10 and 0 m. At 30 s, downrush is occurring and the fluid mixture is nearly saturated with sediment near the sediment/water interface, i.e., $c/c_b \approx 1$. The model predicts significant erosion, but it is important to note that this represents the height of the immobile sediment beneath a slurry of mobile sediment. At 45 s, the downrush phase is coming to an end and deposition is shown between x=-10 and -2 m, a region where 15 seconds earlier erosion had been predicted. By 60 s, a bench-like feature in the bed profile has formed near the still water level and the next uprush phase is predicted to occur.

This result is qualitative but interesting. It shows that the model predicts a slow down in the cycle of uprush and downrush based on the increased sediment load, which is the expected response based on the added inertia of the fluid brought on by the solid material. Whereas uprush commenced a second time between 30 and 40 s in the frictionless, immobile bed test

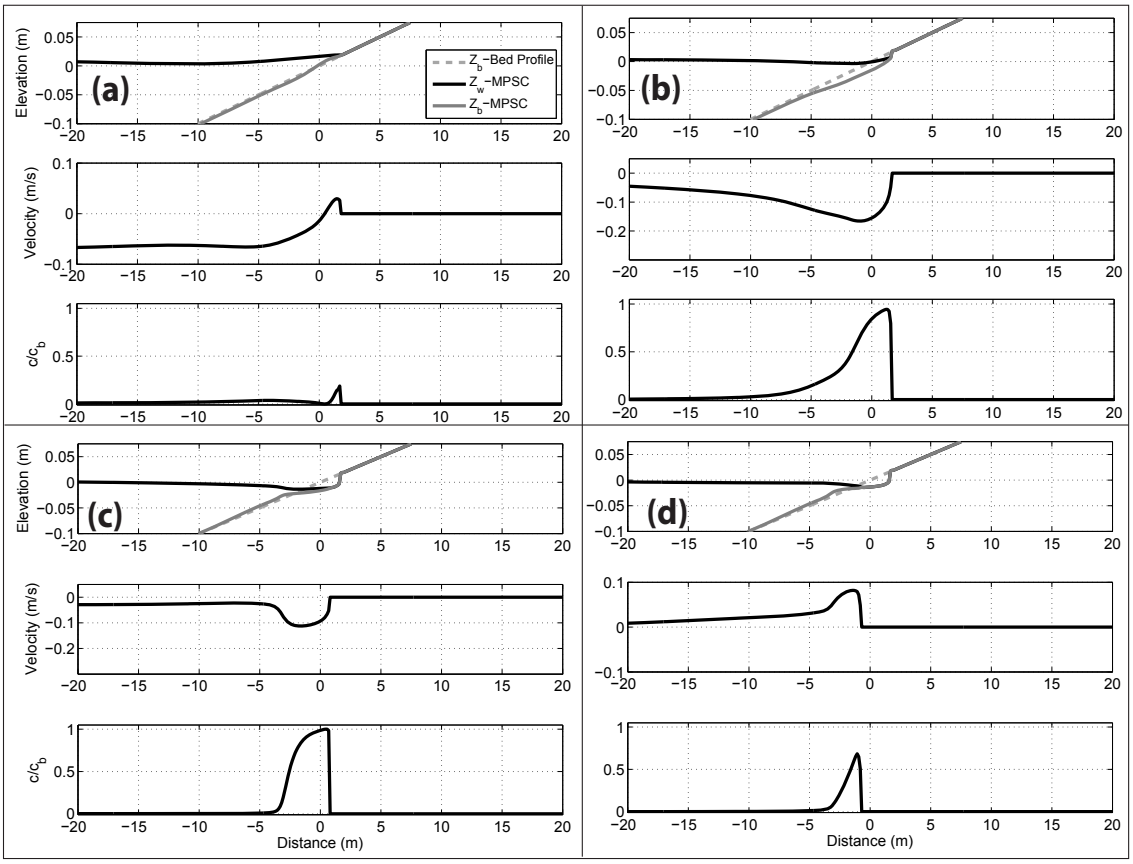

Figure 4.5: Numerical solution of a erodible-bed version of the Carrier and Greenspan [1958] test case based on β=0.5, f=0.024, Δ=1.60 and c_b=0.50. The solution is shown at four times: (a) t=15 s, (b) t=30 s, (c) t=45 s, and (d) t=60 s. For each time, z_w and z_b are shown in the top panel, u_m is shown in the middle panel, and c/c_b is shown in the bottom panel. Note that the model predicts a hyperconcentrated flow ($c \approx c_b$) based on the chosen parameters.

case, uprush commenced a second time between 45 and 60 s in the mobile bed test case. This result also shows that it is possible to predict significant changes in the bed profile over very short time scales, and to predict features like benches that have been observed to occur in natural systems.

4.4.3 Delta Flume Experiment

A large scale flume study of wave-driven beach dune erosion was conducted in the Delta Flume in The Netherlands [van Gent et al., 2008] and the resulting data have been used for several numerical modeling studies of wave-driven beach profile adjustment [van Rijn,

2009, Roelvink et al., 2009]. The Delta Flume is equipped with a wave board capable of generating irregular waves and initiating sediment mobility. Scenario T01 is the focus of this study and the bed profile is shown in Fig. 4.6 and described in detail by van Rijn [2009]. The wave forcing corresponds to a Pierson–Moskowitz spectrum with a significant wave height H_{m0}=1.5 m and a peak period T_p=4.9 s. Under these conditions, waves quickly steepen and break close to the wave board. The offshore boundary of the MPSC model is placed at the wave board, x_b=0 m, and the stochastic water level time series is calculated using an Inverse Fourier Transform (IFT) technique [WAFO, 2000]. The MPSC model was also tested at shoreward coordinate as large as x_b=150 m but the nonreflecting boundary condition did not perform well here, presumably because of very steep waves and high velocities [Hu et al., 2000]. At the wave board, $k_w h_m$=1.0 which corresponds to an intermediate depth. Roelvink et al. [2009] modeled a similar Delta Flume test case with x_b=41 m where $k_w h_m$=0.85.

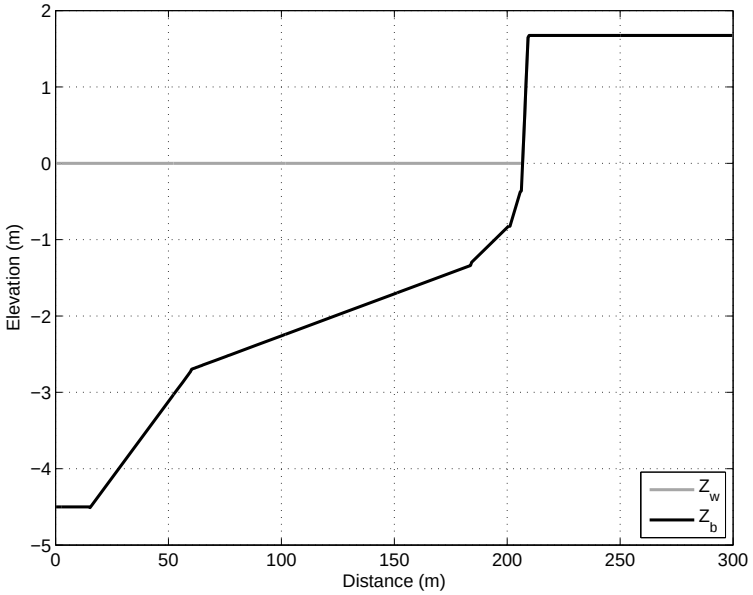

Figure 4.6: Initial condition for the Delta Flume test case T01 [van Gent et al., 2008] .

The MPSC model is applied with a uniform grid resolution of Δx=0.125 m and a time step of Δt=0.0125 s following grid convergence checks to confirm that uncertainty associated with numerical diffusion was negligible compared to other sources of model uncertainty. Model parameters were identified by a manual calibration process leading to f=0.024, β=0.01,

$\Delta = 1.50$, c_b=0.65 and k=0.01. Additionally, the critical slopes for avalanching are set to 0.70 and 1.5 for subaqueous and subaerial sediment, respectively.

Fig. 4.7 compares calibrated model predictions of the sediment profile with measurements at t =0.1, 0.3, 1, 2 and 6 hrs. The MPSC model reproduces the retreat of the berm face as well as the steepness of the berm face, although the level of accuracy varies over time with a better prediction at 6 hrs compared with 2 and 3 hrs. The model also predicts the observed pattern of offshore sediment transport, and again the prediction at 6 hrs is slightly better than the predictions at 2 and 3 hours. Overall, the model captures four important aspects of the observed sediment dynamics: the inland migration of the berm face, the steepness of the berm face, height of sediment at the toe of the berm, and the transport of sediment in the offshore direction.

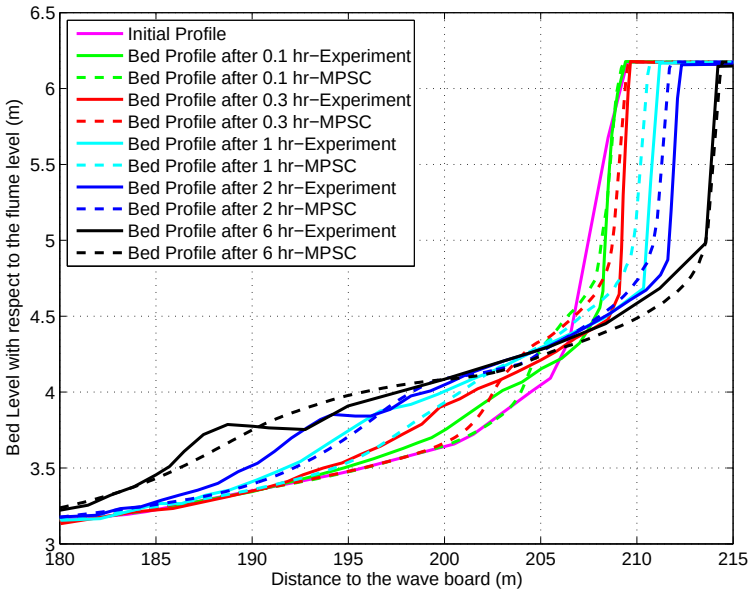

Figure 4.7: Calibrated model predictions and measurements for Delta Flume test case. The model captures the retreat of the beach scarp and the offshore transport of eroded material.

The sensitivity of model predictions to the stochastic water level boundary condition was examined by repeating the previous simulation three times with different IFT water level samples. Table 4.2 presents errors in sediment height z_b for each case, which vary from 5 to 9 cm, but the errors differ by less than 6 mm as a function of the stochastic water level

Table 4.2: Errors in z_b predictions (L_1 norm in meters) in Delta Flume test cases: Sensitivity to stochastic boundary water level time series.

Sample	0.1 hour	0.3 hour	1 hour	2 hour	6 hour
1	0.0567	0.0841	0.0918	0.0821	0.0588
2	0.0599	0.0839	0.0927	0.0758	0.0617
3	0.0587	0.0858	0.0874	0.0781	0.0628

sample. On average, the sensitivity of z_b predictions to the randomness of the boundary condition is about 2-3 mm.

Model structure was also examined as a source of model uncertainty by repeating simulations without SAT (k=0) and without avalanching. Table 4.3 presents model errors in z_b for these cases, and in this case the differences are on the order of several cm for SAT and as much as 48 cm for avalanching.

Table 4.3: Errors in z_b predictions (L_1 norm in meters) in Delta Flume test cases: Sensitivity to model structure.

Model Structure	0.1 hour	0.3 hour	1 hour	2 hour	6 hour
MPSC Model	0.0567	0.0841	0.0918	0.0821	0.0588
MPSC w/o SAT	0.0604	0.0921	0.1054	0.1134	0.0940
MPSC w/o Avalanching	0.0630	0.1212	0.2394	0.3203	0.4826

Fig. 4.8 shows that without SAT (k=0), the MPSC model predicts an overly steep front of sediment moving offshore which nearly doubles the errors for t=6 hrs (Table 4.2). Previous model studies of this test case also produced an overly steep front of sediment moving offshore [van Rijn, 2009], and errors in offshore sediment transport predictions have been reported in other studies [Orzech et al., 2011, Cox et al., 2013]. When the avalanching scheme is deactivated, the model (prediction not shown) does not predict retreat of the beach scarp and therefore no sediment is delivered to the foreshore for offshore transport. These results show that accounting for model structure is much more important than uncertainty associated with the stochastic offshore boundary condition in this test case. In particular, these results show the importance of both avalanching and SAT.

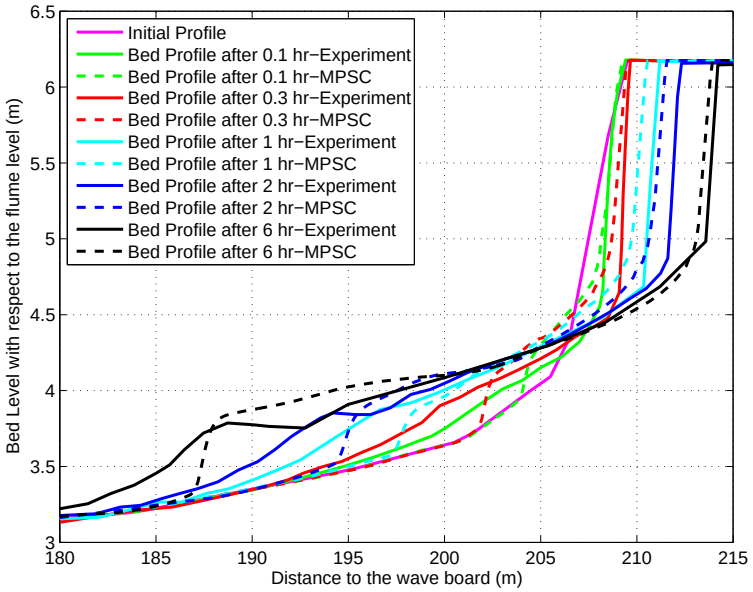

Figure 4.8: Model predictions with k=0 (no SAT) for the Delta Flume test case. The model predicts an overly steep front of material moving offshore.

4.4.4 Newport Beach Experiments

The City of Newport Beach on the coast of southern California surrounds a natural embayment, Newport Bay, and contains densely developed lowlands that are susceptible to flooding from extreme high tides [Gallien et al., 2011] and open ocean waves [Gallien et al., 2014] and are vulnerable to an increase in the frequency and severity of flooding with accelerating sea level rise [Tebaldi and Zervas, 2012]. A regional practice to guard against wave-driven flooding is construction of seasonal or event-based sand berms (anthropogenic berms) which are typically 1-3 m high and can span alongshore distances of up to several kilometers [Gallien et al., 2015]. Berms are constructed by scraping a thin layer of sediment off the foreshore of the beach, during low tides when the beach is accessible to motorized equipment, and depositing the sediment on beach crest.

Test berms were constructed at Newport Beach on three occasions in 2012, as shown in Fig. 4.9, and instrumentation was deployed to simultaneously characterize wave conditions and erosion dynamics [Schubert et al., 2014]. Instrumentation included an AWAC wave

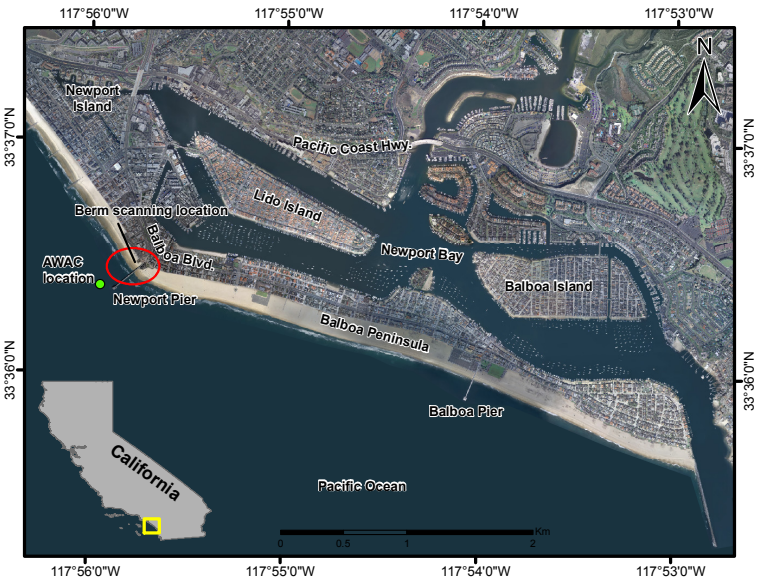

Figure 4.9: Location of Newport Beach berm erosion experiments.

gauge (Nortek USA, Boston, Massacchussetts) deployed about 300 m directly offshore in 10 m of water and a Terrestrial Laser Scanner (TLS) mounted on Newport Pier as shown in Fig. 4.9. A typical berm configuration, with a central berm section parallel to the coast and flanked by two wings, is shown in Fig. 4.10. Table 4.4 provides a summary of berm properties and wave conditions. The berms were placed at roughly Mean Sea Level to ensure failure during a single tide cycle and minimize disturbances to recreational activities on the beach, which is a popular tourist destination. The TLS scanned the berms several times per hour to monitor berm erosion. The data were processed to establish a set of Digital Elevation Models (DEMs) characterizing berm dynamics [Schubert et al., 2014]. The TLS scanner did not register returns from sediment that is saturated with water or submerged by water, so available data are limited to subaerial sediments. This capability is consistent with the goal of monitoring erosion of the berm including the duration over which it withstands overtopping.

The three tests corresponded to dissipative wave conditions and revealed a consistent erosion pattern [Schubert et al., 2014]: wave runup into the berm face triggers slumping of the toe material and steepening of the berm face causes avalanching of berm material down the angle

Table 4.4: Berm and wave properties for Newport Beach berm experiment.

Test	Date	Berm Height (m)	Berm Width (m)	H_s (m)	T_p (m)
1	02/21/2012	1.3	3	0.51	11.5
2	03/07/2012	1.4	3.7	1.18	11.5
3	03/20/2012	1.8	4.5	0.61	11.5

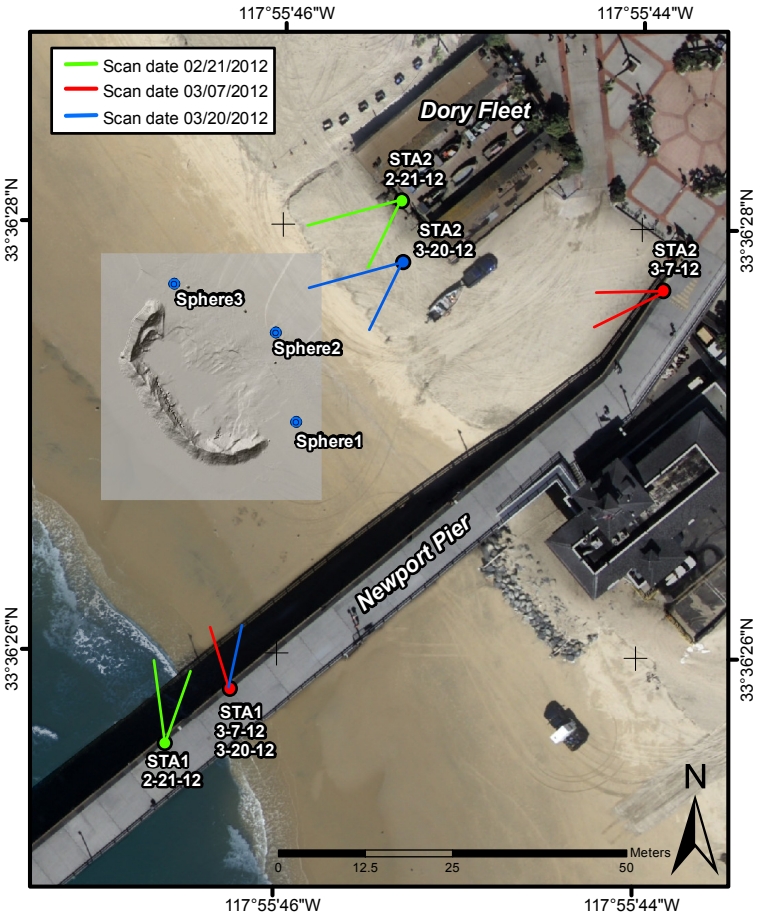

Figure 4.10: Typical berm configuration on the foreshore of Newport Beach. Erosion data from the central berm section (shown) are used to evaluate model performance.

of repose, typically 32-37 degrees. Sediment that slumps down the berm face is moved away relatively quickly with no noticeable change in the beach slope (e.g., foreshore mounding) based on visual observations. With the retreat of the berm face, the crest height of the berm is lowered due to its triangular cross-sectional profile. The rate of crest height reduction was observed to increase over time.

DEMs were processed to create a time-dependent, 1D model of cross-shore berm height in

the central berm section, shown in Fig. 4.10, suitable for 1D modeling under the assumption of alongshore uniformity. A set of five cross-shore transects were evenly spaced through the central berm section and berm height was interpolated from the DEM as a function of cross-shore distance along each transect. Data from the side wings of the berm shown in Fig. 4.10 were ignored. The mean and standard deviation of berm height was then computed as a function of cross-shore position by sampling the five transects. This process was repeated for each of the three berms and all of the scan times. An overall standard deviation in berm height was also computed as an index of berm height variability and found to be 18, 14 and 11 cm for Tests 1, 2, and 3, respectively.

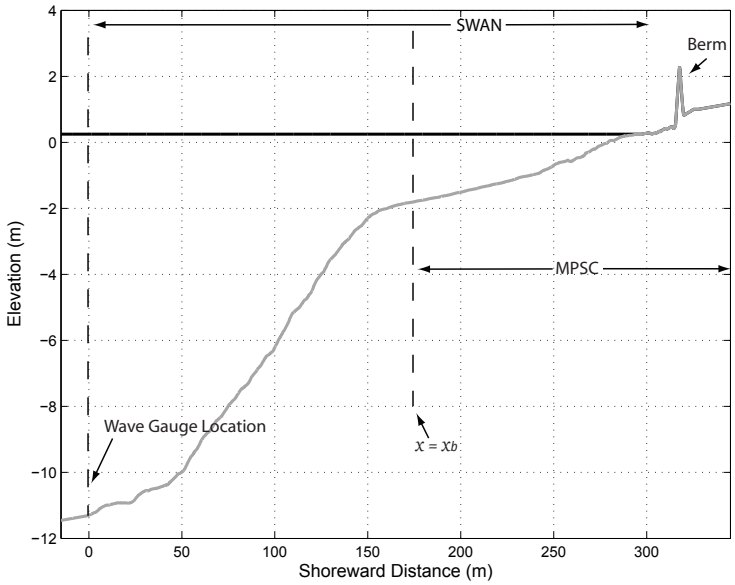

Figure 4.11: Cross-shore profile between wave gauge and test berms at Newport Beach. Note that SWAN [Booij et al., 1999] is applied to predict the wave energy spectrum shoreward of the wave gauge, and the MPSC model is forced by a stochastic time series of water level at an offshore location x_b corresponding to the wave energy spectrum predicted by SWAN. As shown, the MPSC model domain spans subaequeous and subaerial sediment.

Fig. 4.11 shows the cross-shore bathymetry and topography between the wave gauge and beach berm. Note that the wave gauge defines the origin of the shoreward coordinate, x, and that distance is positive shoreward. Spectral wave models such as SWAN [Booij et al., 1999] predict bulk wave parameters in shallow water with relatively good accuracy [Gorrell et al., 2011, McCabe et al., 2011, Gonçalves et al., 2015], and here SWAN is applied to predict the

spatial transformation of the wave energy density shoreward of the wave gauge, as indicated in Fig. 11. Fig. 12 shows JONSWAP wave energy spectrum based on measurement of H_s and T_p at the wave gauge, and SWAN predictions at two shoreward locations. This indicates that energy at the peak frequency increases as waves progress over the relatively steep (0.06 slope) between x=0 and 150 m, and then peak energy either remains constant or decreases with increasing shoreward distance over a relatively mild slope (0.016 slope) between x=150 and 275 m. SWAN also predicts the onset of high frequency (*ca.* 0.17 Hz) energy between x=135 and 165 m, depending on the test case. Fig. 4.12 shows high frequency wave energy at x=200 m for all three berm tests, and at x=150 m for Test 2.

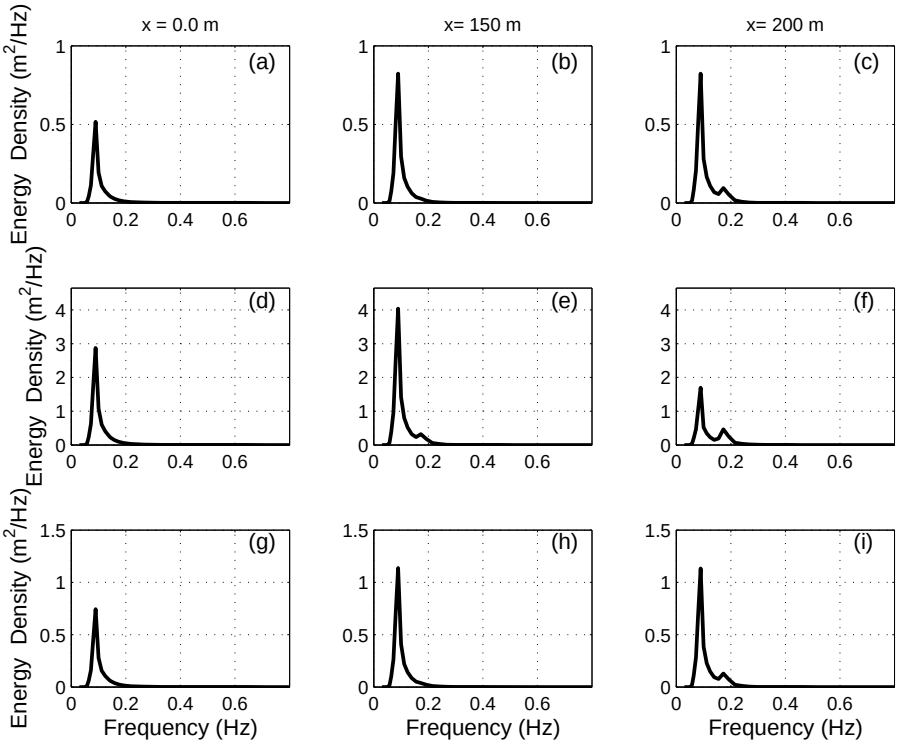

Figure 4.12: Cross-shore transformation of wave energy at Newport Beach for Test 1 (a-c), Test 2 (d-f) and Test 3 (g-i). Left column of panels correspond to JONSWAP wave energy spectrum based on measurements of H_s and T_p at the wave gauge, and center and right columns correspond to SWAN [Booij et al., 1999] predictions.

The MPSC model was applied to each berm test with three different offshore boundary locations. For Test 1 and 3, the boundary location was x_b=0, 150 and 200 m. For Test 2, the boundary location was x_b=0, 125 and 200 m. The intermediate boundary location

was set just outside the point of wave breaking, as recommended by Hu et al. [2000], and the onset of high frequency energy was taken as an indicator of breaking. The most inshore boundary location was set to ensure shallow conditions based on $k_w h_m$. Table 5 shows the values of $k_w h_m$ and H_s/h_m for Tests 1-3, depending on the MPSC boundary location. At the most shoreward boundary location, $k_w h_m$=0.2 and H_s/h_m varies from 0.3-0.8 across the three test cases. At the most offshore boundary location, $k_w h_m$=0.6 and H_s/h_m varies from 0.04-0.11.

The MPSC model was applied with grid resolution of Δx=0.1 m which was found to have a negligible numerical truncation error. Time step was set to Δt=0.005 for cases involving x_b=0 m and 0.01 s otherwise. A manual, iterative process was used to find the optimal parameter set based on the L_1 norm of the bed profile. This lead to uniform set of parameters for all three berm tests: $\Delta = 1.60$, $c_b = 0.55$, f=0.024, β=0.001, k=0.01 and critical slopes for avalanching of 0.35 and 0.90 for wet and dry soil, respectively.

Fig. 5.3 shows MPSC model predictions of water surface and berm heights (top panel), cross-shore velocity (middle panel) and sediment concentration (bottom panel) for Test 1 based on the intermediate boundary location, x_b=150 m. The solution is shown at 10 minute intervals labeled (a)-(h) which reveal the gradual rise of the tide over time, bore-like waves moving through the swash-zone with the classic saw-tooth velocity profile, spikes in sediment concentration at the berm toe up to about 0.1, and the erosion and ultimate overtopping of the berm. This result shows that the model remains stable and does not predict any spurious oscillations throughout the simulation despite the complexity of mobile wet/dry interfaces, shock waves in the swash zone, spikes in sediment concentration, and avalanching. Note also that the model is calibarated with physically reasonable parameter values which compare closely with the parameter values that were optimal for the Delta Flume test case.

Fig. 5.4, 5.5, and 4.16 compare MPSC model predictions for Tests 1, 2 and 3, respectively, with measured berm profiles. These results correspond to x_b=150, 125 and 150 m for Ex-

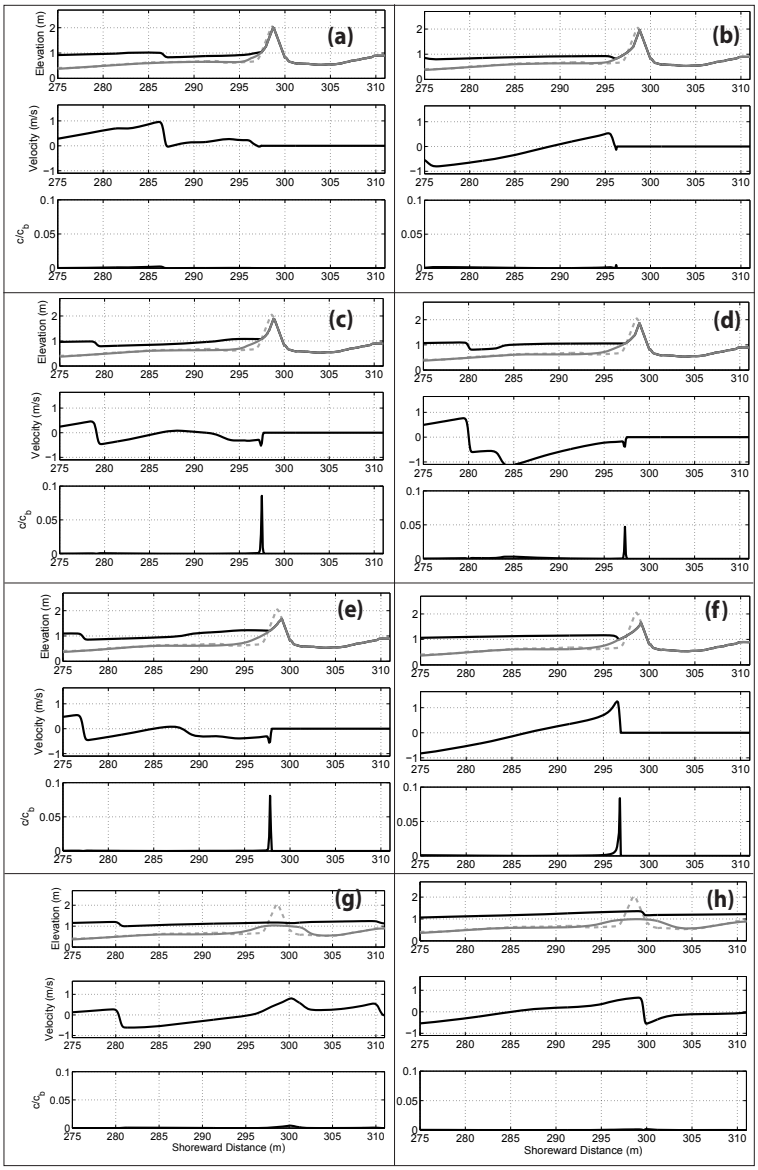

Figure 4.13: Model prediction of Newport Beach foreshore at: (a) 19:00 ,(b) 19:10, (c) 19:20, (d) 19:30, (e) 19:40,(f) 19:50, (g) 20:00, and (h) 20:10. Note the occurrence of shock waves, wet/dry interfaces, and spikes in sediment concentration.

periments 1, 2 and 3 respectively. The whiskers in these plots represent the alongshore variability in the profile of the central berm section, as measured by the standard deviation across transects through the central berm section.

Fig. 5.4a shows that the MPSC model closely tracks the mean profile over time, and Figs. 5.4b, c, and d show that the error in the model is much less than the along shore variability in the berm profile. Note that the model predicts accumulation of sediment at

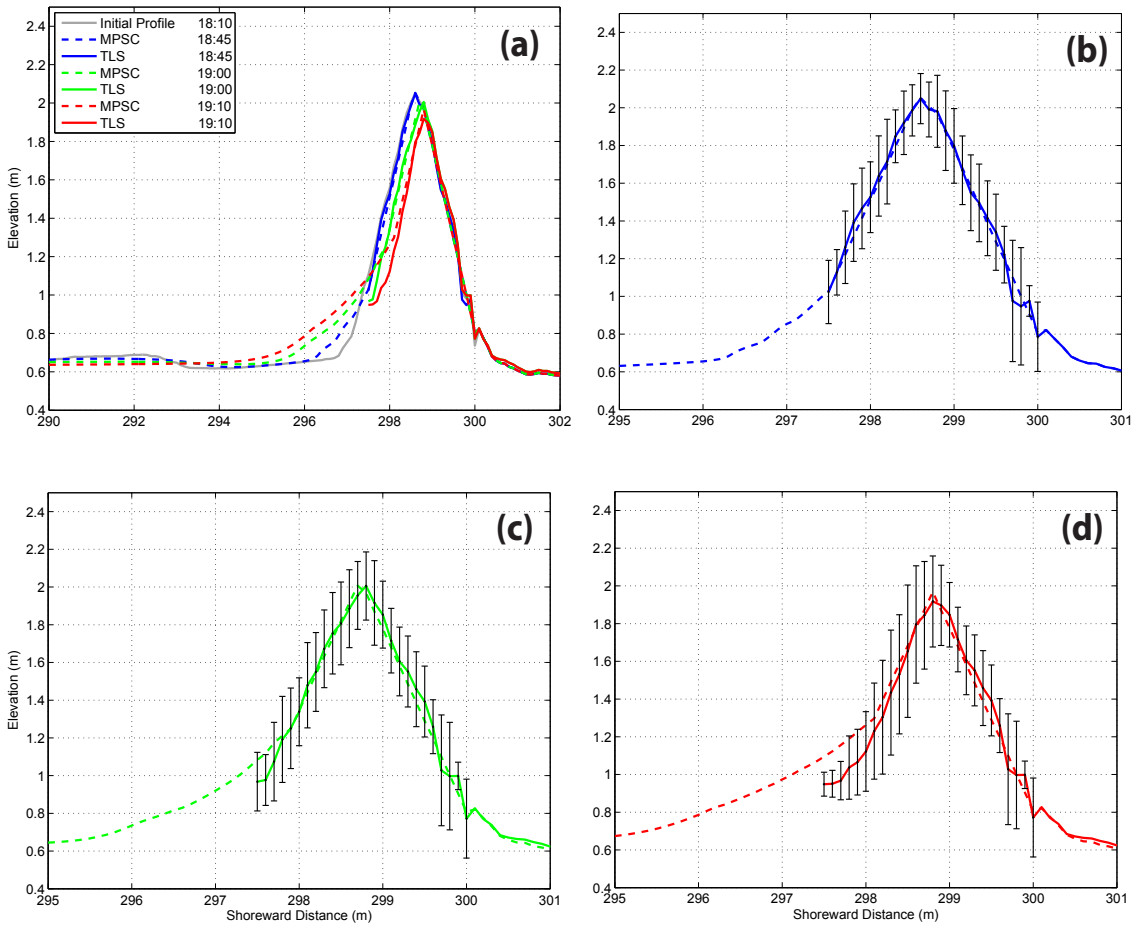

Figure 4.14: Newport Beach Test 1 predictions: (a) comparison of predicted sediment profile to alongshore average profile, and magnified view at (b) 18:45, (c) 19:00 and (d) 19:10. Whiskers represent the standard deviation in measured berm height based on 5 transects through central berm section.

the foreshore toe of the berm but experimental data to verify this prediction are limited because the TLS is only able to scan subaerial sediment. Between 297 and 298 m, there is overlap in measurements and predictions that suggest the model is overpredicting the foreshore berm toe elevation. The berm crest is predicted within 1-2 cm of the alongshore average height, hence model error is much smaller than the alongshore variability.

Fig. 5.5 shows that the model overpredicts berm height in Test 2, and thus underpredicts berm erosion, and Fig. 4.16 shows that the model accurately predicts the berm crest elevation in Test 3 but overpredicts the berm toe elevation.

Fig. 4.17 presents the effect of varying the MPSC model boundary on berm erosion predic-

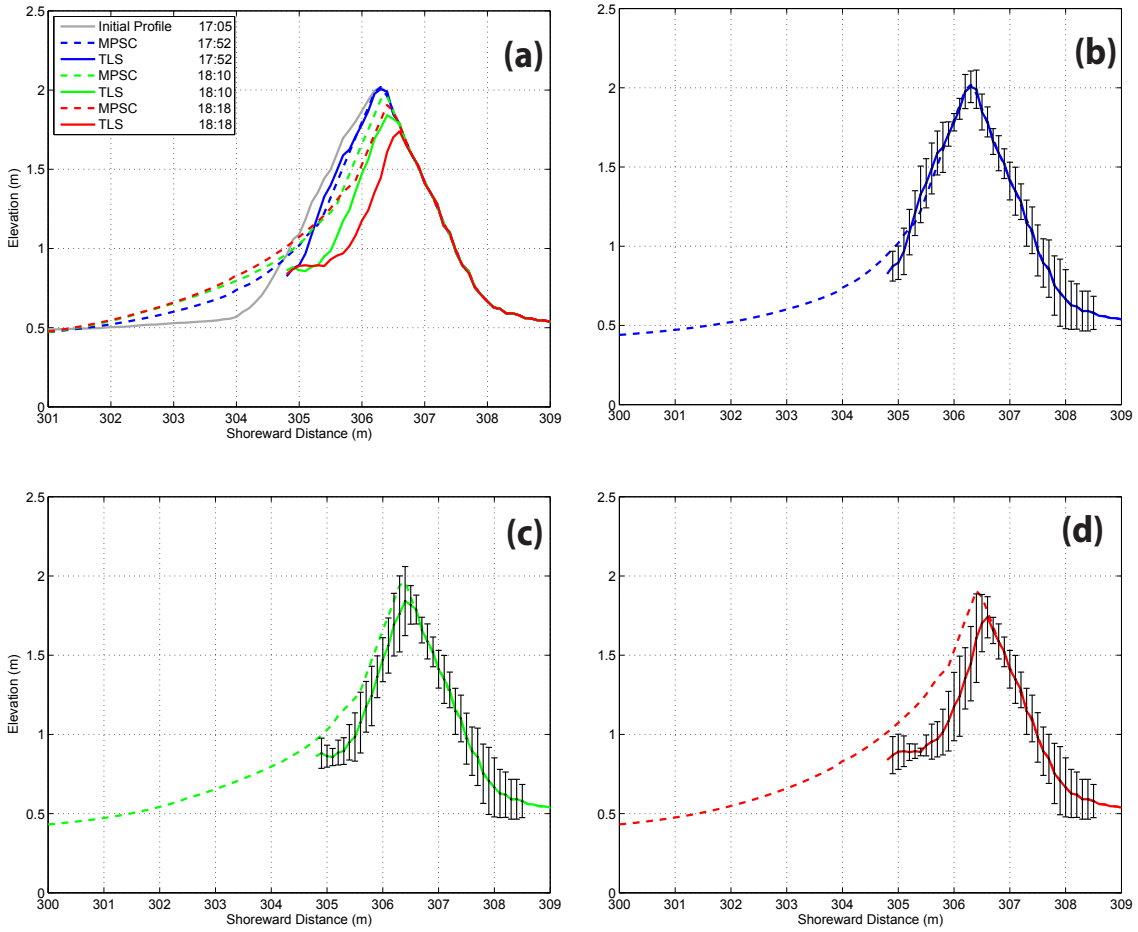

Figure 4.15: Newport Beach Test 2 predictions: (a) comparison of predicted sediment profile to alongshore average profile, and magnified view at (b) 17:52, (c) 18:10 and (d) 18:18. Whiskers represent the standard deviation in measured berm height based on 5 transects through central berm section.

tions, and also the effect of stochastic variability from the boundary water level time series. Errors (L_1 norms) in the berm profile and berm crest height are shown for Tests 1, 2 and 3 and the three different boundary locations. Test 1 corresponds to Fig. 4.17 (a)-(c), Test 2 is (d)-(f), and Test 3 is (g)-(i). Focusing first on stochastic variability, these results indicate that profile errors may differ by as much as 6 cm at a given time but that on average the profile errors differ by about 2 cm. Similarly, berm crest height errors may differ by up to 15 cm as a result of stochastic variability, but on average the berm crest errors differ only by 2-3 cm. Furthermore, the differences in predicted berm profiles arising from stochastic variability are small compared to alongshore variability in the measured berm profile, which is 10-25 cm based on the whiskers shown in Fig. 4.17.

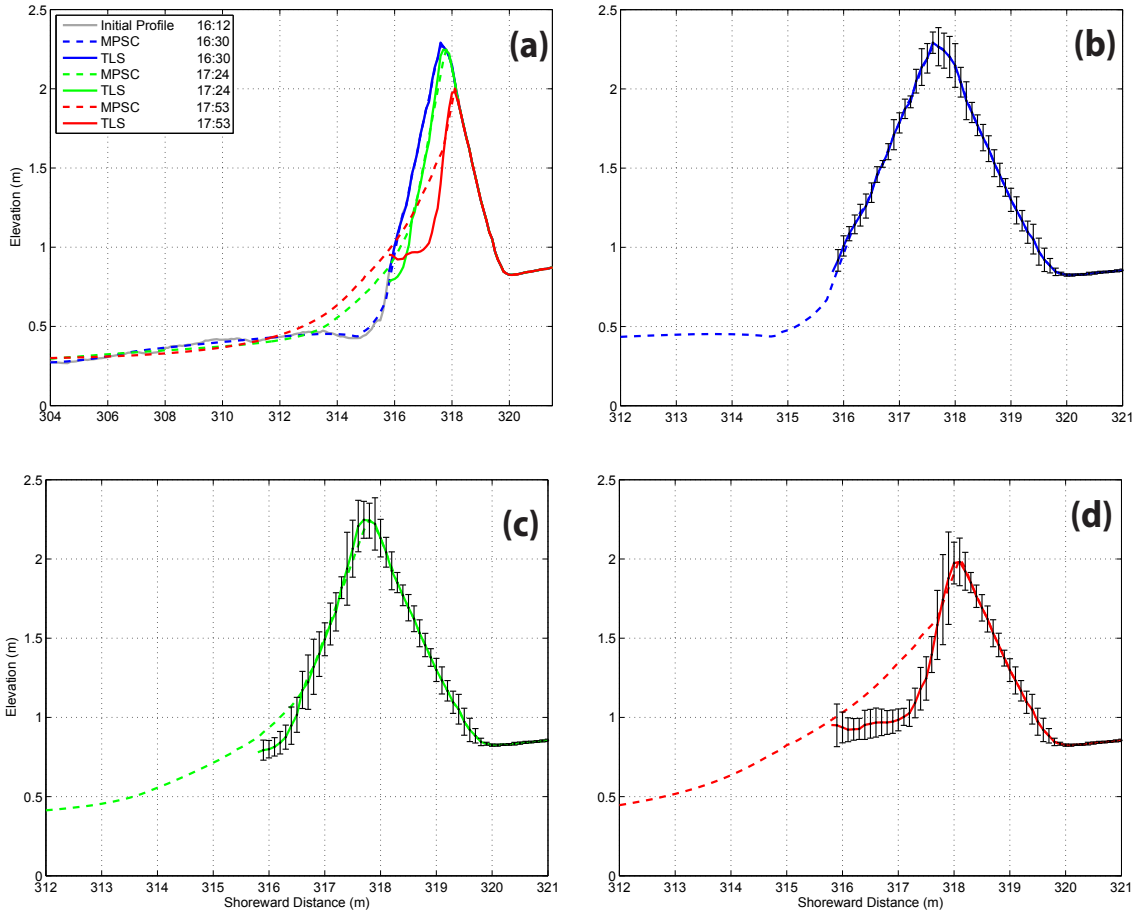

Figure 4.16: Newport Beach Test 3 predictions: (a) comparison of predicted sediment profile to alongshore average profile, and magnified view at (b) 16:30, (c) 17:24 and (d) 17:53. Whiskers represent the standard deviation in measured berm height based on 5 transects through central berm section.

Focusing now on the effect of the boundary location, results shown in Fig. 4.17 indicate a suprisingly weak sensitivity. Changing the boundary location yielded less than 1 cm change in berm height errors, on average. Profile errors were not strongly affected by the boundary location, but in Tests 1 and 3 where the model performed best, the most offshore boundary location yielded a larger crest error at the final measurement time compared to the the most shoreward boundary location.

The sensitivity of the model to wave height was also examine. The MPSC model was applied to Test 1 using half of the measured wave height, H_s=0.25 m, and using each of the three boundary locations, x_b=0, 150, and 200 m. As before, SWAN was applied to compute the

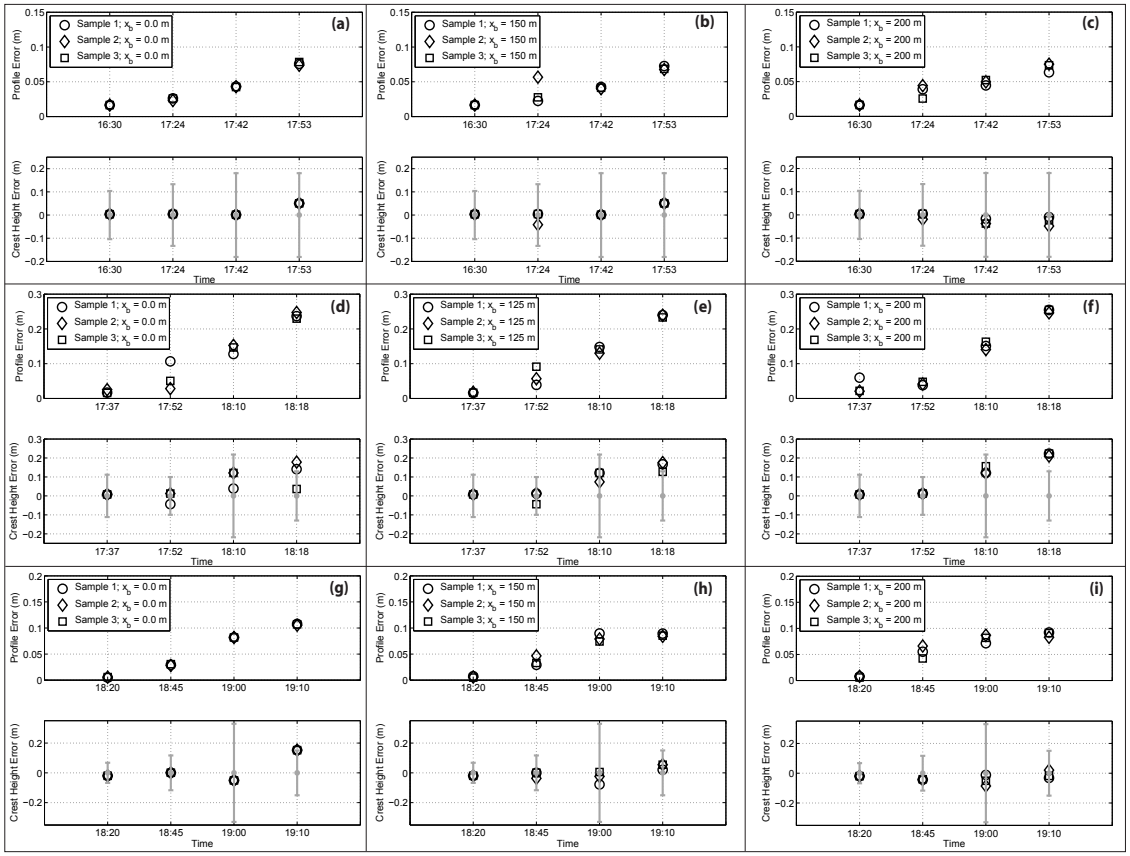

Figure 4.17: Errors (L_1 norms) in predictions of the berm profile (Profile Error) and berm crest height (Crest Height Error) for Test 1 (a-c), Test 2 (d-f) and Test 3 (g-i). Three boundary locations are shown for each test, and sample 1, 2 and 3 correspond to different randomly generated water level time series. Whiskers shown in the Crest Height Error plot indicate the standard deviation of height across five berm transects which reflects alongshore variability.

energy spectrum for each boundary location. Fig. 4.18 shows profile errors and crest height errors for H_s=0.25 m alongside predictions based on the measured wave height H_s=0.5 m. This shows that decreasing the boundary wave height increases errors in the berm profile and berm crest height. As would be expected, the reduction in wave height leads to an underprediction of berm erosion that has a cumulative effect on berm errors leading to the largest errors at the latest times.

In the Delta Flume test case, the SAT flux and avalanching scheme exhibited a strong influence on model predictions. The influence of SAT is also investigated for the Newport Beach experiment. Fig. 4.19 compares Test 1 berm height predictions with (k=0.01) and

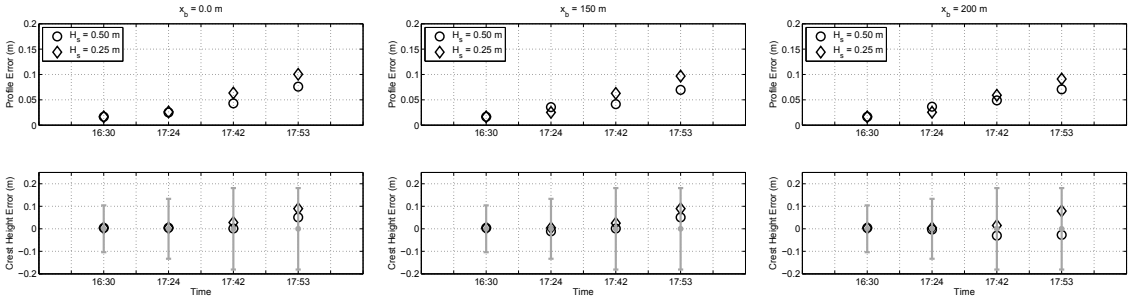

Figure 4.18: Comparison of errors in the berm profile (Profile Error) and berm crest height (Crest Height Error) for Test 1 with H_s=0.25 m versus H_s=0.5 m.

without SAT (k=0). Similar to the Delta Flume test case, sediment moving offshore forms a steep front using k=0 compared to k=0.01. Similar trends are observed in Test 2 and 3, so these results are not presented. When the avalanching scheme is not activated, results are inaccurate because the berm does not erode, as in the Delta Flume test case, so these results are not shown.

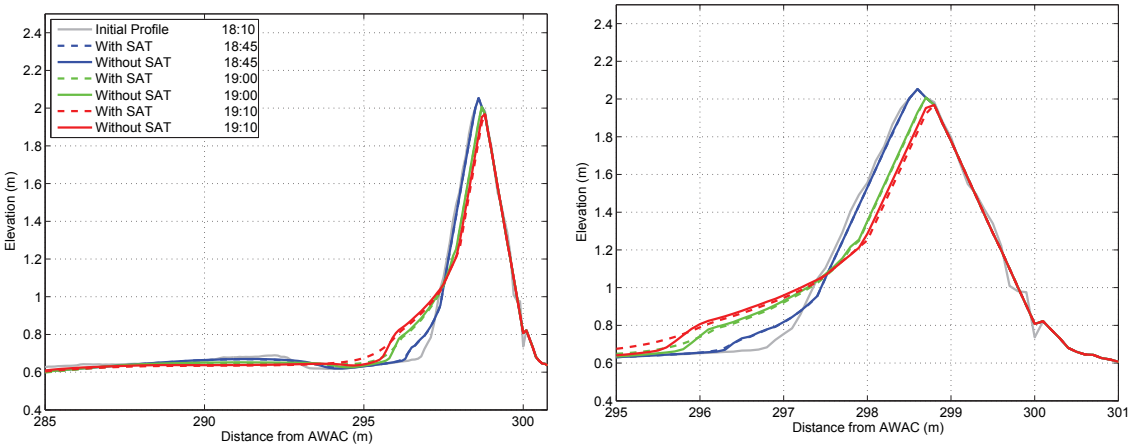

Figure 4.19: Comparison of Test 1 beach profile predictions with (k=0.01) and without (k=0) SAT, showing its effect diffusing sharp fronts of sediment moving offshore.

4.5 Discussion

Several limitations of the model are identified that could affect its performance in practical applications. First, the 1D formulation limits the model to situations with alongshore uniformity. In the Newport Beach test case, the MPSC model overpredicts sediment heights at

the berm toe which suggests that offshore transport is underpredicted. However, the short length of the test berm, *ca.* 30 m, is an important consideration. At the later stages of berm erosion when the berm toe was inundated, wave uprush penetrated past the berm and around its sides, and this may have acted to disperse foreshore sediment in the alongshore direction and thus lower the berm toe elevation faster than by offshore transport alone. Multidimensional modeling is needed to better understand the role of alongshore and cross-shore transport on the evolution of sediment heights at the berm toe.

Underprediction of Newport Beach berm erosion in Test 2 could be related to infragravity energy or slope toe prediction errors. No infragravity energy was prescribed at the boundary. Although explicit inclusion of infragravity energy is outside the scope of the present study, this is a limitation of the current model formulation. In its present form, the model successfully predicted berm erosion where infragravity energy was minimal, suggesting suitability for applications where berms are constructed for flood threats characterized by high tides but relatively low wave energy. This weakness could potentially be addressed by specifying infragravity energy at the MPSC model boundary or implementing a non-hydrostatic momentum balance similar to [McCall et al., 2014] whereby infragravity wave energy becomes an emergent feature of the solution based on forcing at higher frequencies. Another contributing factor could be overprediction at the toe as described previously, which in turn retards avalanching down the berm face. This possibility was explored by repeating the Test 2 simulation with a larger value of k=0.075, which enhances SAT in the offshore direction, and improves the accuracy of the model as shown in Fig. 4.20. This result may suggest that berm crest prediction is linked berm toe accuracy. However, this level of diffusion may not be physically reasonable and individual berm calibration is unsatisfying from a predictive skill perspective.

An important attribute of numerical models is the ability to conserve mass, and finite volume schemes generally possess excellent conservation properties because they discretize conserva-

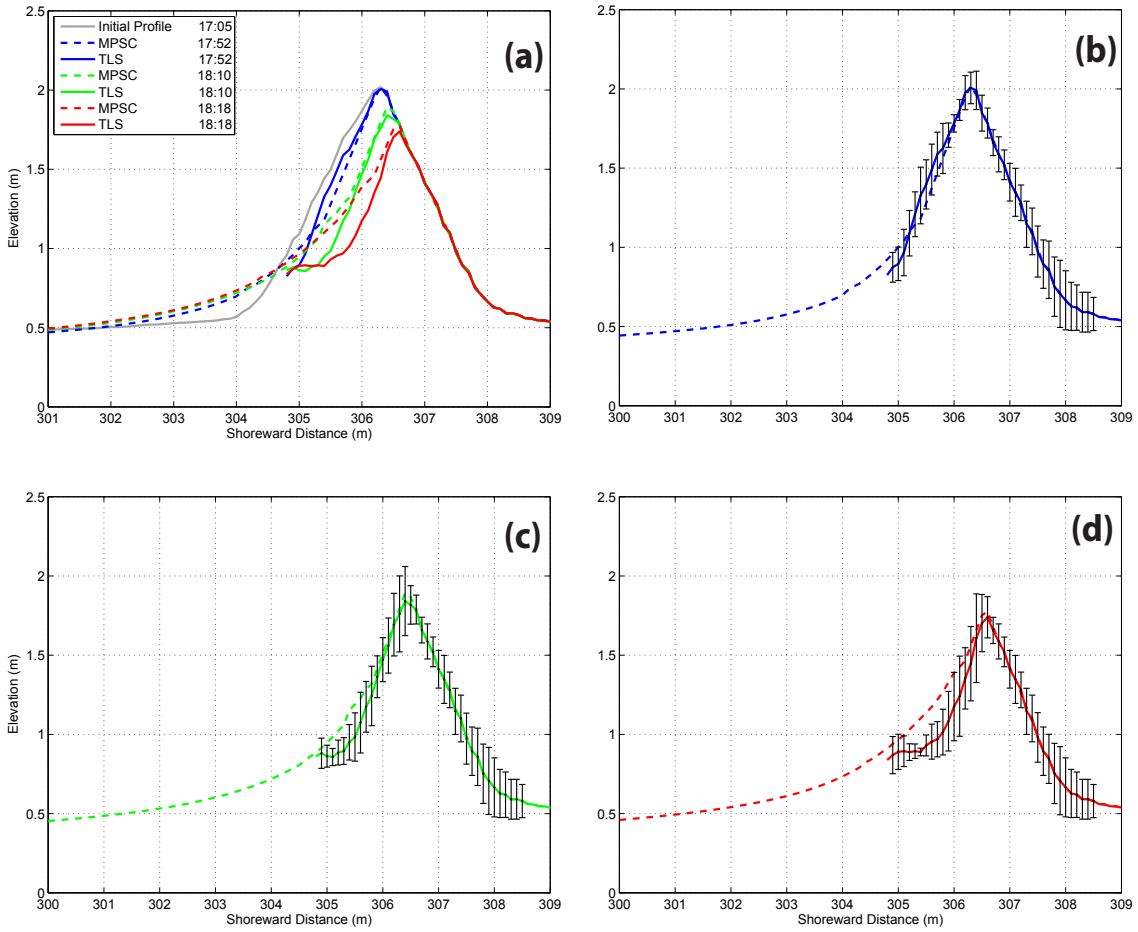

Figure 4.20: Newport Beach Test 2 predictions using a high level of SAT (k=0.075): (a) comparison of predicted sediment profile to alongshore average profile, and magnified view at (b) 17:52, (c) 18:10 and (d) 18:18. Whiskers represent the standard deviation in measured berm height based on 5 transects through central berm section.

tive, integral forms of the governing equations which are precise statements of conservation. Global mass conservation errors were measured for each the three Newport Beach experiments and found comparable to numerical precision, as shown in Table 5 which includes both solid phase and liquid phase errors. Ironically, Rosatti and Begnudelli [2013] originally discretized SAT as a source term, an approach that was initially followed by the authors in the development of the MPSC model presented here. However, the source term discretization was abandoned when it was found to cause mass conservation errors of approximately 1% for both fluid and sediment volume.

Models were executed on a desktop workstation with an Intel®Xeon®W3550 quad-core

processor with a base frequency of 3.07 GHz and 20 GB RAM. The models were set up for sequential execution in the background using one core, so other tasks could be performed on the computer simultaneously. The Delta flume test involving a 6 hr run time completed execution in 30 min. The Newport Beach test case involving a 2 hr run time completed execution in about 60, 12 min, and 8 min with the boundary placed at x_b=0, 150 or 200 m. The most offshore boundary position demanded a longer simulation time as a result of more cells and a smaller time step resulting from increased depth (and gravitational wave speed). Considering both accuracy and computation cost, the most shoreward boundary location (x_b=200 m) appears optimal. However, the performance of the non-reflecting offshore boundary condition, which relies on simplified wave dynamics, may restrict the position of the boundary for numerical reasons as was observed in the Delta Flume test case. Similar to the work of Hu et al. [2000], results here indicate that model accuracy with respect to berm erosion and overtopping does not immediately decline as a result of a model boundary that extends beyond shallow conditions to an intermediate depth [Hu et al., 2000].

4.6 Conclusions

A wave by wave model of swash zone hydromorphodynamics capable of simulating hyperconcentrated flows, wetting and drying, and erosion and overtopping of anthropogenic beach berms is presented for modeling rapid erosion of beaches and protective berms that guard against coastal flooding. The Multi-Phase Shock-Capturing (MPSC) model is based on vertically integrated, multi-phase, hydrostatic flow equations that are solved by a Godonov-type shock capturing scheme. The model formulation systematically incorporates the effect of sediment entrainment on inertia and momentum fluxes in the swash zone, which can be important to the momentum balance. The model is shown to remain stable and conserve both fluid and solid mass to numerical precision, to geometrically converge with grid refinement,

and to calibrate with physically reasonable parameter values in laboratory and field test cases.

The MPSC model includes a diffusive flux of sediment transport that can be used to smear out predictions of overly sharp sediment fronts that form when beaches are quickly eroded and material is moved offshore. The diffusive flux is termed Slope Assisted Transport because it enhances transport of suspended sediment in the downslope direction. The diffusive flux can be scaled by a user specified parameter, k, and a value of 0.01 was found to perform well in test cases presented here.

The MPSC model is forced by a stochastic time series of water level derived from the wave energy spectrum predicted at a shallow to intermediate depth. Testing at Newport Beach indicates that predictions of beach berm erosion are not strongly sensitive to the location of the offshore boundary over a range of positions characterized by $k_w h_m$ values between 0.6 and 0.2, but run times increased as the boundary was placed further offshore as a result of more computational cells and a smaller time step for stability. Average height errors based on the boundary location were about 1-2 cm. Additionally, predictions were not found to be strongly sensitive to stochastic variability which also accounts for 1-2 cm change in average height errors. Future application of the model should be accompanied by sensitivity checks on the boundary location and stochastic variability as this may be more important under different circumstances.

The Newport Beach test cases show that the MPSC model accurately predicts the erosion and overtopping of an anthropogenic berm with the same set of model parameters in two of three cases with different wave heights and berm heights; in these test cases overall berm height errors are less than 10 cm. In the third case, the berm height error is about 20 cm or about 15% of the initial berm height. This test case corresponds to twice the signficant wave height as the two other cases where the model performed well, a likely explanation for the error is infragravity wave energy that is not captured by the model.

To summarize, this study points to a promising numerical modeling framework for resolving flow, sediment transport, and beach changes in a computationally manageable way to support coastal flood preparedness, mitigation and emergency response. However, additional research is needed to address model limitations and characterize uncertainties under a wide range of field conditions.

Chapter 5

Two Dimensional Multi-Phase Shock Capturing Model

5.1 Introduction

The 1D-MPSC model consists of mass conservation equations for water and sediment over a mobile bed and a momentum equation [Majd and Sanders, 2014]. The horizontal momentum balance is coupled to sediment concentration, so the 1D-MPSC can be applied to hyper-concentrated flows including granular flows, mud flows and flows with discontinuities (shocks) in the flow and sediment heights [Capart and Young, 1998, Fraccarollo et al., 2003]. Many researchers have developed two-dimensional (2D) extensions of so-called Debris Flow Models like the MPSC model presented here, and benchmark tests have revealed promising results [Armanini et al., 2008, Chen and Peng, 2006b, Murillo and Garcia-Navarro, 2012, Rosatti and Begnudelli, 2013]. A 2D formulation of the MPSC model would offer the ability to model more complex beach erosion scenarios involving alongshore variability in nearshore bathymetry, beach topography, and berm heights as well as applications involving waves

that approach the beach at an oblique angle. 2D models have also been found advantageous for modeling breaching of earthen levees [Van Emelen et al., 2011].

This chapter presents the 2D-MPSC model, including model formulation, numerical methods, and an applications which frames a computational challenge deserving of future research. The originality of the 2D-MPSC model over other 2D models is linked to unique features of the 1D-MPSC models: minimal diffusion of sediment, ability to preserve stationary solutions, and ability to resolve wet/dry fronts as shown in Chapter 2.

5.1.1 Governing Equations in 2D

The governing equations for a Two-Phase model are derived from continuity and momentum conservation laws for liquid and solid phases and can be written as follows,

$$\frac{\partial \mathbf{U}}{\partial t} + \frac{\partial \mathbf{F}}{\partial x} + \frac{\partial \mathbf{G}}{\partial y} + \mathbf{H}_x \frac{\partial z_b}{\partial x} + \mathbf{H}_y \frac{\partial z_b}{\partial y} = \mathbf{S} \tag{5.1}$$

where

$$\mathbf{U} = \begin{pmatrix} h + z_b \\ ch + c_b z_b \\ u_x h(c\Delta + 1) \\ u_y h(c\Delta + 1) \end{pmatrix} \quad \mathbf{S} = \begin{pmatrix} 0 \\ 0 \\ -f(u_x^2 + u_y^2)u_x \\ f(u_x^2 + u_y^2)u_y \end{pmatrix} \tag{5.2}$$

$$\mathbf{F} = \begin{pmatrix} u_x h \\ cu_x h \\ (c\Delta + 1)(u_x^2 h + g\frac{h^2}{2}) \\ (c\Delta + 1)u_x u_y h \end{pmatrix} \quad \mathbf{G} = \begin{pmatrix} u_y h \\ cu_y h \\ (c\Delta + 1)u_x u_y h \\ (c\Delta + 1)(u_y^2 h + g\frac{h^2}{2}) \end{pmatrix} \tag{5.3}$$

$$\mathbf{H_x} = \begin{pmatrix} 0 \\ 0 \\ gh(c\Delta + 1) \\ 0 \end{pmatrix} \qquad \mathbf{H_y} = \begin{pmatrix} 0 \\ 0 \\ 0 \\ gh(c\Delta + 1) \end{pmatrix} \tag{5.4}$$

Closure is achieved with the following entrainment law,

$$c = c_b \beta \frac{V^2}{h} \tag{5.5}$$

where $V = (u_x^2 + u_y^2)^{1/2}$.

5.2 MPSC scheme in 2D

The 2D-MPSC scheme to solve Eq. 5.1 mirrors the approach used by the 1D-MPSC scheme in that the solution is advanced by the LHLLC method [Majd and Sanders, 2014], which involves application of an HLLC to estimate fluxes and the so-called lateralization method to account for bottom slope effects on momentum fluxes. The HLLC method requires knowledge of wave speeds which motivates characteristic analysis of the governing equations.

5.2.1 Characteristic Analysis in 2D

Characteristic analysis in 2D is performed separately along the x and y directions to identify the relevant wave speeds required for the HLL-type approximate Riemann solver used to compute numerical solutions. For example, analysis of characteristics in the x direction ignores all terms in Eqs. 5.1 with gradients in the y direction, and vice-versa. There are four real and distinct eigenvalues in each case, but one eigenvalue is in the velocity the perpendicular direction, leaving only three to be computed numerically by solving for the

roots of a cubic equation. This can be accomplished with an explicit cubic equation solver [Majd and Sanders, 2014], which avoids the need for a costly iterative search algorithm.

5.2.2 Update Scheme

The 2D-MPSC scheme sequentially updates the fluid mixture, sediment volume, and momentum equations. It is therefore helpful to reference elements of solution and flux vectors defined as follows,

$$\mathbf{U} = \begin{pmatrix} U_1 \\ U_2 \\ U_3 \\ U_4 \end{pmatrix}, \qquad \mathbf{F} = \begin{pmatrix} F_1 \\ F_2 \\ F_3 \\ F_4 \end{pmatrix}, \qquad \mathbf{G} = \begin{pmatrix} G_1 \\ G_2 \\ G_3 \\ G_4 \end{pmatrix}, \tag{5.6}$$

$$\mathbf{H_x} = \begin{pmatrix} 0 \\ 0 \\ H_{x,3} \\ 0 \end{pmatrix}, \qquad \mathbf{H_y} = \begin{pmatrix} 0 \\ 0 \\ 0 \\ H_{y,4} \end{pmatrix}, \qquad \mathbf{S} = \begin{pmatrix} 0 \\ 0 \\ S_3 \\ S_4 \end{pmatrix} \tag{5.7}$$

The spatial domain is discretized into $N \times M$ cells in x and y directions, respectively, and the solution is assumed to be piecewise constant with states $\mathbf{U}_{i,j}$, for $i = 1, \ldots, N$, $j = 1, \ldots, M$. Fluxes are evaluated at cell edges facing the x direction located at $x_{i+1/2,j}$ with $i = 0, \ldots, N$ and $j = 1, \ldots, M$ and cell edges facing the y direction located at $y_{i,j+1/2}$ with $i = 1, \ldots, N$ and $j = 0, \ldots, M$. Following Armanini et al. [2008], the fluid mixture continuity equation is updated as follows,

$$(U_1)_{i,j}^{n+1} = (U_1)_{i,j}^{n} + \frac{\Delta t}{\Delta x}\left[(F_1)_{i-1/2,j}^{*} - (F_1)_{i+1/2,j}^{*}\right] + \frac{\Delta t}{\Delta y}\left[(G_1)_{i,j-1/2}^{*} - (G_1)_{i,j+1/2}^{*}\right] \tag{5.8}$$

where $(F_1)^*_{i+1/2,j}$ and $(G_1)^*_{i,j+1/2}$ represent fluxes computed with the HLL scheme as follows,

$$(F_1)^* = \frac{s_R F_{1L} - s_L F_{1R} + s_R s_L (U_{1R} - U_{1L})}{s_R - s_L} \tag{5.9}$$

and

$$(G_1)^* = \frac{s_R G_{1L} - s_L G_{1R} + s_R s_L (U_{1R} - U_{1L})}{s_R - s_L} \tag{5.10}$$

where s indicates wave speeds and the subscripts L and R represents the cells to the left i and right $i+1$, respectively. Note that the wave speeds in the x and y directions are different and follow from separate calculations. Various choices are available to estimate the wave speeds s_L, s_R [Toro, 1997], and the following was used here [Fraccarollo et al., 2003].

$$s_L = \min(\lambda_{1L}, \lambda_{1R}) \tag{5.11}$$

$$s_R = \max(\lambda_{3L}, \lambda_{3R}) \tag{5.12}$$

where λ_1 and λ_3 represent maximum and minimum characteristic wave speeds, respectively [Fraccarollo et al., 2003], in the direction of the flux.

Next, the sediment continuity equation is updated as follows,

$$(U_2)^{n+1}_{i,j} = (U_2)^n_{i,j} + \frac{\Delta t}{\Delta x}\left[(F_2)^*_{i-1/2,j} - (F_2)^*_{i+1/2,j}\right] + \frac{\Delta t}{\Delta y}\left[(G_2)^*_{i,j-1/2} - (G_2)^*_{i,j+1/2}\right] \tag{5.13}$$

where the fluxes are computed using an HLLC scheme similar to Majd and Sanders [2014]. When $(F_1)^* \geq 0$, flow is in the positive x direction and the solid flux is computed as follows,

$$(F_2)^* = \frac{s_S F_{2L} - s_L F_{2R} + s_S s_L (U_{2R} - U_{2L})}{s_S - s_L} \tag{5.14}$$

where s_L is computed as before and s_S is computed from the speed of contact discontinuities in neighboring cells. On the other hand, when $(F_1)^* < 0$, the solid flux is computed as follows for directional symmetry,

$$(F_2)^* = \frac{s_R F_{2L} - s_S F_{2R} + s_R s_S (U_{2R} - U_{2L})}{s_R - s_S} \tag{5.15}$$

Similarly, when $(G_1)^* \geq 0$, flow is in the positive y direction and the solid flux is computed as follows,

$$(G_2)^* = \frac{s_S G_{2L} - s_L G_{2R} + s_S s_L (U_{2R} - U_{2L})}{s_S - s_L} \tag{5.16}$$

and when $(G_1)^* < 0$, the solid flux is computed as follows for directional symmetry,

$$(G_2)^* = \frac{s_R G_{2L} - s_S G_{2R} + s_R s_S (U_{2R} - U_{2L})}{s_R - s_S} \tag{5.17}$$

Before the solid flux is used to update Eq. 5.13, a limiting function is applied to prevent the magnitude of the solid flux F_2^* (or G_2^*) from exceeding the magnitude of the total fluid mixture flux F_1^* (or G_1^*), as this would give non-physical predictions. The limiting is expressed as follows,

$$(F_2)^*_{i+1/2,j} = \text{maxmod}[(F_1)^*_{i+1/2,j}, (F_2)^*_{i+1/2,j}] \tag{5.18}$$

$$(G_2)^*_{i+1/2,j} = \text{maxmod}[(G_1)^*_{i,j+1/2}, (G_2)^*_{i,j+1/2}] \tag{5.19}$$

Finally, the momentum equations are updated using the LHLL scheme in a two-step process. The first step is explicit, and the second step is implicit for stability, accuracy and consistency. The x-momentum equation is updated as follows,

$$(U_3)^*_{i,j} \;=\; (U_3)^n_{i,j} + \frac{\Delta t}{\Delta x}\left[(F_3)^{*R}_{i-1/2,j} - (F_3)^{*L}_{i+1/2,j}\right]$$

$$= +\frac{\Delta t}{\Delta y}\left[(G_3)^*_{i,j-1/2} - (G_3)^*_{i,j+1/2}\right] \tag{5.20}$$

$$(U_3)^{n+1}_{i,j} = (U_3)^*_{i,j} + \Delta t (S_3)^{n+1}_{i,j} \tag{5.21}$$

and the y-momentum equation is updated similarly,

$$\begin{aligned}(U_4)^*_{i,j} &= (U_4)^n_{i,j} + \frac{\Delta t}{\Delta x}\left[(F_4)^*_{i-1/2,j} - (F_4)^*_{i+1/2,j}\right] \\ &= +\frac{\Delta t}{\Delta y}\left[(G_4)^{*R}_{i,j-1/2} - (G_4)^{*L}_{i,j+1/2}\right] \qquad (5.22)\\ (U_4)^{n+1}_{i,j} &= (U_4)^*_{i,j} + \Delta t (S_4)^{n+1}_{i,j} \qquad (5.23)\end{aligned}$$

where the superscripts L and R represent adjustments to the fluxes that account for bed slope effects expressed by the $H_{x,3}$ term and $H_{y,4}$ term in Eq. 2.22. Note that the fluxes are only adjusted when aligned with the directionality of the update equation. To update the x momentum equation, the fluxes with star superscripts are computed as follows,

$$(F_3)^* = \frac{s_R F_{3L} - s_L F_{3R} + s_R s_L (U_{3R} - U_{3L})}{s_R - s_L} \tag{5.24}$$

$$(G_3)^* = \frac{s_R G_{3L} - s_L G_{3R} + s_R s_L (U_{3R} - U_{3L})}{s_R - s_L} \tag{5.25}$$

$$(F_4)^* = \frac{s_R F_{4L} - s_L F_{4R} + s_R s_L (U_{4R} - U_{4L})}{s_R - s_L} \tag{5.26}$$

$$(G_4)^* = \frac{s_R G_{4L} - s_L G_{4R} + s_R s_L (U_{4R} - U_{4L})}{s_R - s_L} \tag{5.27}$$

where the wave speeds s_L and s_R are computed separately for the x and y direction using Eqs. 5.11 and 5.12, as before. Hence, all momentum fluxes are computed using the HLL Riemann solver method.

Fluxes in the direction of the momentum equation are modified with lateralization terms to account for bottom slope effects. For the x direction, lateralization terms are computed as,

$$\delta_{L,R} = \frac{s_{L,R}}{s_R - s_L}\frac{1}{2}(H_{x,3L} + H_{x,3R})\,(z_{bR} - z_{bL}) \tag{5.28}$$

where z_{bR} and z_{bL} represent bed elevation in the cells to the left and right, respectively, of the cell edge, and the wave speeds s_L and s_R correspond to the x-direction. The final fluxes required by Eq. 5.21 are given by,

$$(F_3)^{*L} = (F_3)^* - \delta_L \qquad (F_3)^{*R} = (F_3)^* - \delta_R \tag{5.29}$$

For the y direction, lateralization terms are computed as,

$$\delta_{L,R} = \frac{s_{L,R}}{s_R - s_L}\frac{1}{2}(H_{x,4L} + H_{x,4R})\,(z_{bR} - z_{bL}) \tag{5.30}$$

where z_{bR} and z_{bL} again represent bed elevation in the cells to the left and right, respectively, of the cell edge relative to the y direction, and s_L and s_R correspond to wave speeds in the y-direction. The final fluxes required by Eq. 5.23 follow as,

$$(G_4)^{*L} = (G_4)^* - \delta_L \qquad (G_4)^{*R} = (G_4)^* - \delta_R \tag{5.31}$$

After all of the flux terms are evaluated, the friction terms are modeled implicitly as shown by Eqs. 5.21 and 5.23. This step is extremely important because it affords a high level of numerical stability and because it ensures that sediment concentrations, fluid velocities, and sediment fluxes are synchronized consistent with the closure relation given by Eq. 5.5. Unfortunately, the solution update requires the simultaneous solution of two non-linear equations. The final solution update challenge can be expressed as follows: solve for h, z_b, c, u_x and u_y

given an intermediate solution $\tilde{\mathbf{U}}$ resulting from Eqs. 5.8, 5.13, 5.20 and 5.22 as follows,

$$h + z_b = \tilde{U}_1 \tag{5.32}$$

$$ch + c_b z_b = \tilde{U}_2 \tag{5.33}$$

$$(\Delta ch + h)u_x + \Delta t f V u_x = \tilde{U}_3 \tag{5.34}$$

$$(\Delta ch + h)u_y + \Delta t f V u_y = \tilde{U}_4 \tag{5.35}$$

This is approached by combining Eqs. 5.34 and 5.35 into the following equation,

$$V^2(\Delta ch + h + \Delta t f V)^2 = \tilde{U}_3^2 + \tilde{U}_4^2 \tag{5.36}$$

Furthermore, by combining Eqs. 5.5, 5.32 and 5.33 we can write,

$$c_b \beta V^2 - c_b h = U2 - c_b U_1 \tag{5.37}$$

Eqs. 5.36 and 5.37 are combined into a single equation with a single unknown, h, which is solved by a Newton-Raphson iterative method. Once h is computed, the remaining variables follow directly from Eqs. 5.32-5.37 without the need for further iteration. Unfortunately, Newton-Raphson iteration is computationally expensive and this issue is explored in the follow results section.

Fig. presents a flow chart that summarizes the 2D-MPSC algorithm design.

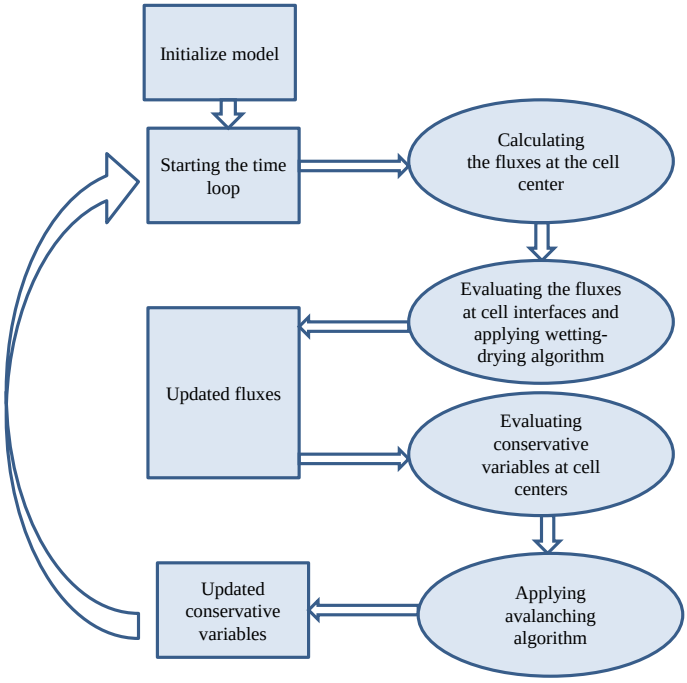

Figure 5.1: DFM's update Flowchart.

5.3 Circular Dam-Break Test Problem

A simple test problem that offers valuable insight into model performance is a circular dam-break problem. The spatial domain is given by a square of dimension $L \times L$ with L=10 m, the sediment height is uniformly set to zero everywhere, and fluid thickness h_m is set to unity everywhere but in the center of the domain, where a circular subdomain of radius R=2.5 m centered at $x = L/2$ and $y = L/2$ is characterized by a fluid thickness of h_m=4 m.

To implement the 2D-MPSC model, the spatial domain is discretized by $N \times N$ computational cells and integrated with a time step that satisfies the CFL condition for a period of 20 s. The model is implemented using Matlab® and run on a on a desktop workstation with an Intel®Xeon® W3550 quad-core processor with a base frequency of 3.07 GHz and 20 GB RAM.

5.3.1 Preliminary Results

Fig. 5.2 shows model results at selected times for based on a 40×40 computational grid. The solution is qualitatively correct in that the hump, which is located in the center of the domain, evolves in a radially symmetric manner and that the bed profile is eroded where the velocity is high. However, the computational cost is found to be very high. In this case, when the model is integrated sequentially, the run time is 13.86 s, which is only slightly faster than the duration of the model simulation.

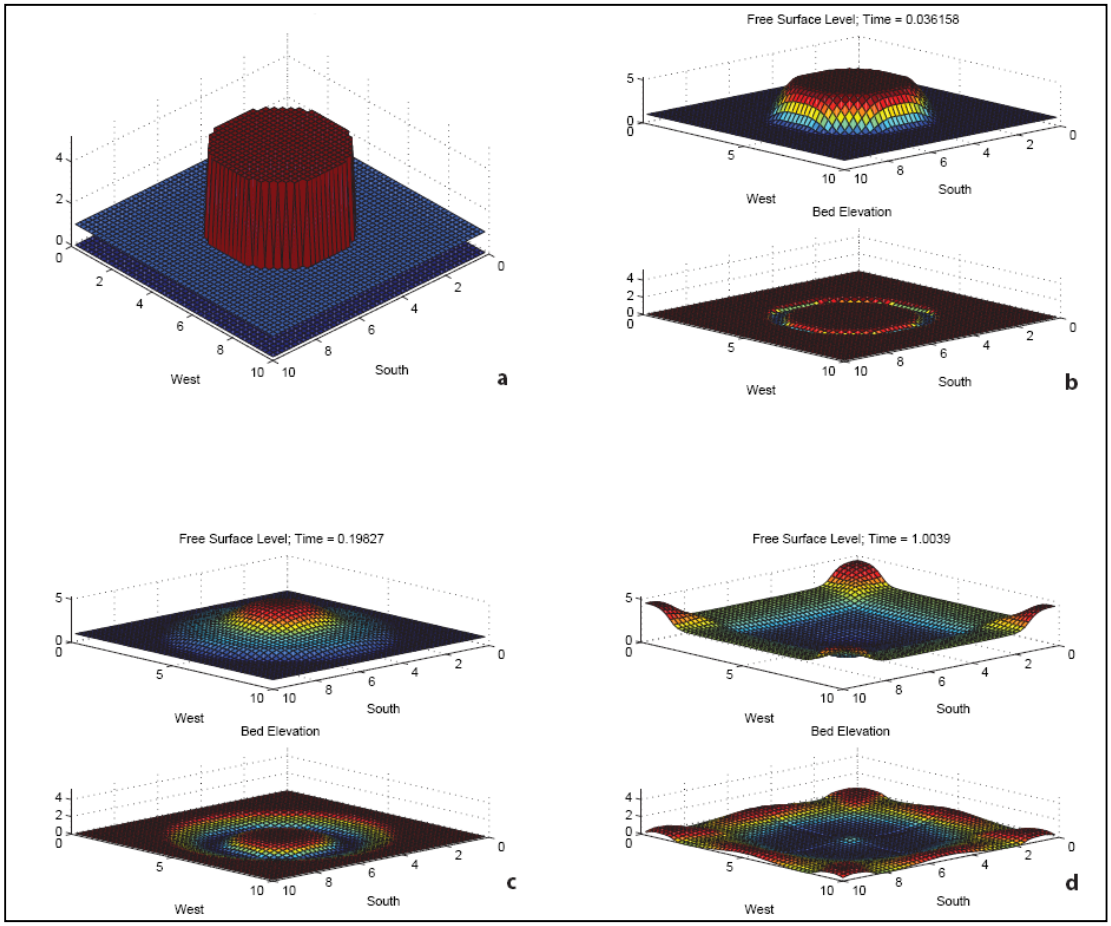

Figure 5.2: Snapshots for a benchmark test, a 2D circular dambreak.

The previous model run was profiled in Matlab® to determine the parts of the algorithm responsible for high computational demands, and the results are shown in Table 5.1. This indicates that about 70% of the computational cost of associated with updating the con-

servative variables, which requires the iterative Newton-Raphson solver. Hence, as a first step towards reducing computational costs, the conservative variable update routine is parallelized using a Single Process Multiple Domain (SPMD) technique of parallelization. That is, the domain is decomposed into subdomains that are assigned to different processors.

Table 5.1: Profiling the DFM for circular dambreak test.

Code	$RunTime$(s)
Cell Center Fluxes	0.76
Interface Fluxes	2.01
Conservative Variables	10.07
Avalanching Algorithm	1.02

Matlab automatically manages the memory aspects of parallel computing, allowing the modeler to focus on designing domain decomposition from an operational perspective. Consequently, four different domain decomposition strategies were tested, including a base case corresponding to sequential execution. In Scenario 1 and 2, domain decomposition occurs in only one coordinate direction, and in Scenario 3, domain decomposition occurs in both coordinate directions. Fig. 5.3, 5.4 and 5.5 graphically illustrate the Scenarios 1, 2 and 3 respectively.

The results of parallelization using N=40, 80, 160 and 320 are shown in Table 5.2.

Table 5.2: Parallel execution times (s) for circular dambreak test

Name	Decomposition	N=40	N=80	N=160	N=320
Scenario 0	Sequential	13.76	50.08	190.94	760.43
Scenario 1	2×1	8.85	28.18	104.37	417.96
Scenario 2	4×1	8.25	23.31	81.10	321.10
Scenario 3	2×2	8.03	22.79	80.50	319.44

5.3.2 Discussion and Recommendations

The preceding results show that domain decomposition in 1D performs (Scenario 2) nearly as well as 2D domain decomposition (Scenario 3), and that run times can be significantly

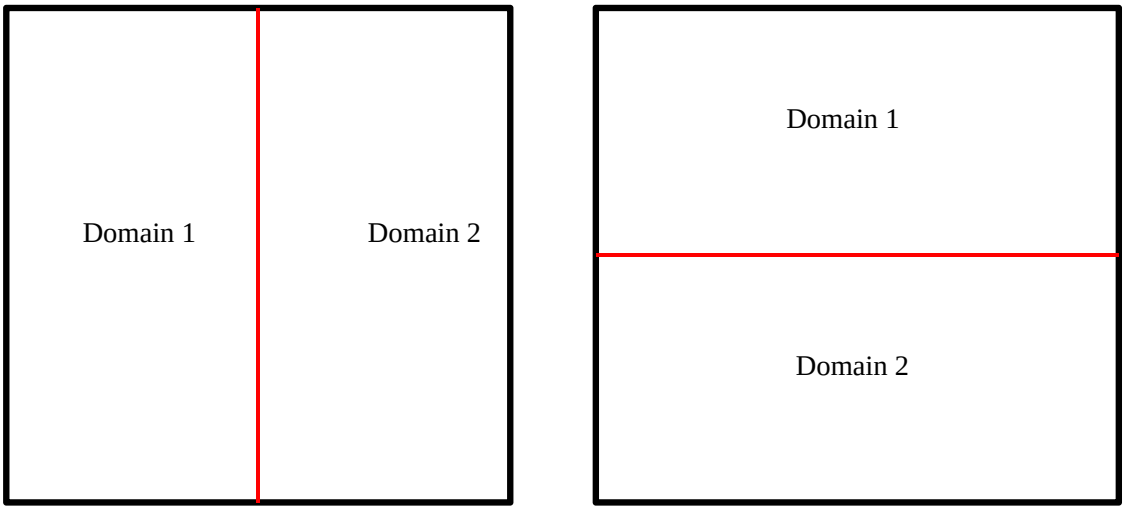

Figure 5.3: Scenario 1. The Original domain decompose into two subdomains, left panel domain decomposition in j direction and right panel shows domain decomposition in i direction.

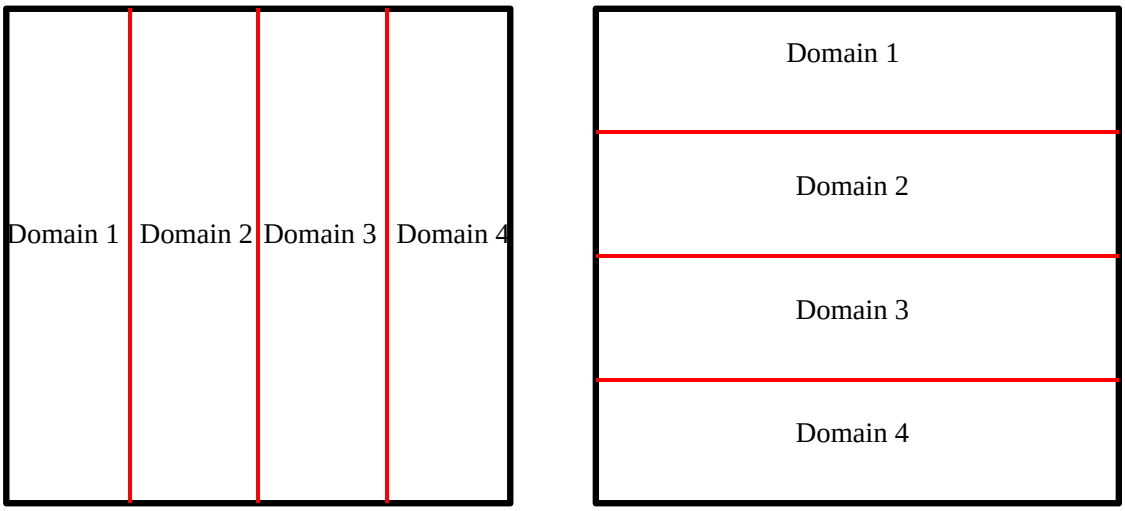

Figure 5.4: Scenario 2. The Original domain decompose into four subdomains, left panel domain decomposition in j direction and right panel shows domain decomposition in i direction.

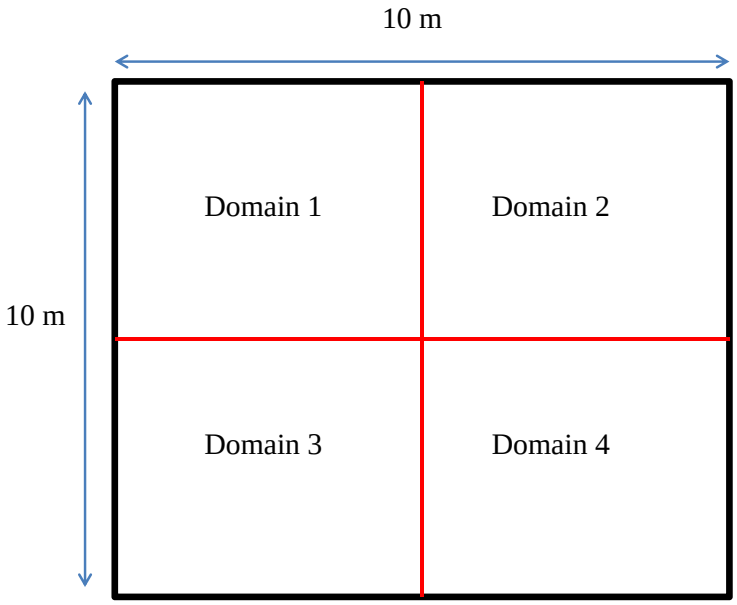

Figure 5.5: Scenario 3. The Original domain decompose into four subdomains.

reduced by using more computational cores. Further reduction in run times can presumably be achieved by parallelizing the remainder of the algorithm, especially the flux calculation. Therefore several steps are recommended to make the 2D-MPSC algorithm more computationally efficient:

- Use domain decomposition to parallelize all explicit loops (domain sweeps) that contribute to updating the solution over time.
- Use the Fortran programming language instead of Matlab; based on previous experience, Fortran codes involving many sweeps and operations are capable of significantly faster execution than Matlab codes.
- Research alternatives to using Newton-Raphson iteration to update the conservative variables at each time step.

5.4 Summary and Outlook

In this chapter, a two dimensional version of the MPSC model, 2D-MPSC, is introduced. The governing equations and numerical methods are presented, and the method is shown to give qualitatively correct solutions in a simple test problem. The intellectual merit of the 2D-MPSC model over other existing 2D models parallels the unique advantages of the 1D model: minimal numerical diffusion of sediment, ability to preserve stationary solutions, and ability to track wet/dry fronts on a sloping bed which is critical for beach applications. Additional research is needed to make the 2D-MPSC model more computational efficient, so it can be applied to practical test cases. A strategy to achieve this goal is presented herein, and is based primarily on parallel computing. When a reasonably efficient model is developed, there is an excellent opportunity to further explore the berm erosion with unique experimental data presented in Chapter 3. In particular, there are unanswered questions regarding the mechanisms responsible for moving sediment away from the toe of the berm; and one possible explanation is alongshore advection that cannot presently be modeled by 1D-MPSC. Development of 2D-MPSC will also need to focus attention on the offshore boundary condition, which ideally needs to accommodate directional waves.

Chapter 6

Summary and Conclusions

Beaches are challenging environments for hydromorphodynamic modeling because of the complexity of wave dynamics, sediment transport and shoreline movement. Advances in shock-capturing numerical methods have enabled Bagnold-type, NLSW swash zone shallow-models to resolve discontinuities in both the fluid and sediment distribution which are dominant features on beaches. Field and laboratory studies have shown that spikes in sediment concentration occur on beaches during uprush and downrush, which could invalidate conventional models that use a clear water momentum balance, but it does not pose a limitation for a Multi-Phase, Shock-Capturing (MPSC) approach. A wave by wave model of swash zone hydromorphodynamics capable of simulating hyperconcentrated flows, wetting and drying, and erosion and overtopping of anthropogenic beach berms is presented for modeling rapid erosion of beaches and protective berms that guard against coastal flooding.

Chapter 2 presents an LHLLC scheme which constitutes the numerical engine of the MPSC model. The LHLLC scheme can be viewed as an enhanced version of the LHLL scheme with several advantages and broader applicability compared to the LHLL scheme: Since LHLLC uses the contact wave speed for sediment mass flux computations, the LHLLC scheme can

be applied to test problems with steep, submerged slopes whereas the LLHL scheme will erroneously predict massive terrain slumping. The LHLLC shows significantly less diffusion of sharp sediment fronts under subcritical flow conditions, compared with the LHLL scheme. By introducing a wet/dry tolerance and a modified flux under "dry" conditions, the LHLLC scheme preserves stationary solutions involving wet/dry interfaces. The LHLLC scheme includes an avalanching that offers improved accuracy in a channel flow test problem scheme and is important in field applications to account for slumping of near vertical channel features common to incised channels and beach berms.

Chapter 3 presents experiments that were conducted to develop a better understanding of anthropogenic bern erosion and to support modeling presented in Chapter 4. Anthropogenic berms are built on a seasonal basis or in anticipation of a hazardous event by scraping a thin layer of sediment off the foreshore of the beach, during low tides when the beach is accessible to motorized equipment, and depositing the sediment on beach crest. Chapter 3 shows that Terrestrial Laser Scanning (TLS) delivers an accurate model of the berm geometry as it is eroded by waves. Additionally, Chapter 3 shows reveals the basic processes that contribute to berm erosion: waves first inundate the berm toe, causing slumping upon saturation of previously unsaturated material. Furthermore, upon slumping of the toe, the face of the berm steepens which triggers avalanching down the berm face. This adds material to the toe of the berm, which is in turn wetted by waves and moved offshore with the backwash. Experiments also indicate that the crest of the berm is lowered primarily as a result of avalanching, and that there is significant alongshore variability in the berm height over time. Overtopping first occurs after a low point in the berm crest, or breach, is exposed.

Chapter 4 formally presentes the MPSC model as a tool to model rapid beach and berm erosion during storms. The model is shown to remain stable and conserve both fluid and solid mass to numerical precision, to geometrically converge with grid refinement, and to calibrate with physically reasonable parameter values in laboratory and field test cases. The MPSC

model also includes a diffusive flux of sediment transport that can be used to smear out predictions of overly sharp sediment fronts that form when beaches are quickly eroded and material is moved offshore. The diffusive flux is termed Slope Assisted Transport because it enhances transport of suspended sediment in the downslope direction. The diffusive flux can be scaled by a user specified parameter, k, and a value of 0.01 was found to perform well in test cases presented here.

The MPSC model is forced by a stochastic time series of water level derived from the wave energy spectrum predicted at a shallow to intermediate depth. Testing at Newport Beach indicates that predictions of beach berm erosion are not strongly sensitive to the location of the offshore boundary over a range of positions characterized by $k_w h_m$ values between 0.6 and 0.2, but run times increased as the boundary was placed further offshore as a result of more computational cells and a smaller time step for stability. Average height errors based on the boundary location were about 1-2 cm. Additionally, predictions were not found to be strongly sensitive to stochastic variability which also accounts for 1-2 cm change in average height errors. Future application of the model should be accompanied by sensitivity checks on the boundary location and stochastic variability as this may be more important under different circumstances.

The Newport Beach test cases show that the MPSC model accurately predicts the erosion and overtopping of an anthropogenic berm with the same set of model parameters in two of three cases with different wave heights and berm heights; in these test cases overall berm height errors are less than 10 cm. In the third case, the berm height error is about 20 cm or about 15% of the initial berm height. This test case corresponds to twice the signficant wave height as the two other cases where the model performed well, a likely explanation for the error is infragravity wave energy that is not captured by the model.

To summarize, this study points to a promising numerical modeling framework for resolving flow, sediment transport, and beach changes in a computationally manageable way to support

coastal flood preparedness, mitigation and emergency response. However, additional research is needed to address model limitations and characterize uncertainties under a wide range of field conditions. A 2D extension of the 1D-MPSC model is presented in Chapter 6, and preliminary results indicate the need to address high computational demands especially as a result of an implicit update scheme that requires Newton-Raphson iteration.

Bibliography

M.B. Abbott, H.M. Petersen, and O. Skovgaard. On the numerical modeling of short waves in shallow water. *Journal of Hydraulic Research*, 1:173–203, 1978.

A. Armanini, L. Fraccarollo, and M. Larcher. Liquidgranular channel flow dynamics. *Powder Technology*, 182:218227, 2008.

A. Armanini, L. Fraccarollo, and G. Rosatti. Two-dimensional simulation of debris flows in erodible channels. *Computers and Geosciences*, 35:9931006, 2009.

C. Armaroli, P. Ciavola, L. Perini, L. Calabrese, S. Lorito, A. Valentini, and M. Masina. Critical storm thresholds for significant morphological changes and damage along the emilia-romagna coastline, italy. *Geomorphology*, 143-144:34–51, 2012.

R. A. Bagnold. Mechanics of marine sedimentation, in the sea: Ideas and observations. *Interscience*, 3:4963, 1963.

R. A. Bagnold. An approach to the sediment transport problem from general physics. *U.S. Geol. Surv., Professional Papaer*, 422-I, 1966.

J.A. Bailard. An energetics total load sediment transport model for a plane sloping bed. *Journal of geophysical research*, 86(C11):10938–10954, 1981.

D.M. Barber and J.P. Mills. Vehicle based waveform laser scanning in a coastal environment. *International Archive of Photogrammetry, Remote Sensing and Spatial Information Sciences*, 36, 2007. c55.

David R Basco and Cheol S Shin. Dune damage curves and their use to estimate dune maintenance costs. *Coastal Engineering Proceedings*, 1(25), 1996.

P.D. Bates. Simplified two-dimensional numerical modelling of coastal flooding and example applications. *Hydrological Processes*, 26(16):2515–2521, 2012.

P.D. Bates, R.J. Dawson, J.W. Hall, M.S. Horritt, R.J. Nicholls, J. Wicks, and M.A.A.M. Hassan. Simplified two-dimensional numerical modelling of coastal flooding and example applications. *Coastal Engineering*, 52(9):793–810, 2005.

M. Bitenc, R. Lindenbergh, K. Khoshelham, and A.P. Van Waarden. Evaluation of a lidar land-based mobile mapping system for monitoring sandy coasts. *Remote Sensing*, 35(7): 1472–1491, 2011.

N. Booij, L.H. Holthuijsen, and R.C. Ris. Athird-generation wave model for coastal regions. part 1: Model description and validation. *Journal of Geophysical Research*, 104:76497666, 1999.

Scott F. Bradford and Brett F. Sanders. Finite-volume model for shallow-water flooding of arbitrary topography. *Journal of Hydraulic Engineering*, 128:289298, 2002.

R. Briganti and N. Dodd. Shoreline motion in nonlinear shallow water coastal models. *Coastal Engineering*, 56:495–505, 2009a.

R. Briganti and N. Dodd. On the role of shoreline boundary conditions in wave overtopping modeling with non-linear shallow water equations. *Coastal Engineering*, 56:1061–1067, 2009b.

M. Brocchini and T.E. Baldock. Recent advances in modeling swash zone dynamics: influence of surf-swash interaction o nearshore hydrodynamics and morphodynamics. *Rev. of Geophysics*, 46:RG3003, 2008.

M. Brocchini and N. Dodd. Nonlinear shallow water equation modeling for coastal engineering. *Journal of Waterway, Port, Coastal and Ocean Engineering*, 134(2):104–120, 2008.

J. Brock, C. Wright, A. Sallenger, W. Krabill, , and R. Swift. Basis and methods of nasa airborne topographic mapper lidar surveys for coastal studies. *Journal of Coastal Research*, 18(1):1–13, 2002.

J.D. Brown, T. Spencer, and I. Moeller. Modeling storm surge flooding of an urban area with particular reference to modeling uncertainties: A case study of canvey island, united kingdom. *Water Resources Research*, 43(6), 2007. W06402.

L.M. JR. Brush and M.G. Wolman. Knickpoint behavior in noncohesive material: A laboratory study. *Bulletin of The Geological Society of America*, 71(1):59–74, 1980.

P. Bruun. Beach scraping is it damaging to beach stability? *Journal of Coastal Engineering*, 7(2):167173, 1983.

Z. Cao, R. Day, and S. Egashira. Coupled and decoupled numerical modeling of flow and morphological evolution in alluvial rivers. *J. Hydraulic Engineering*, 128(3):306–321, 2002.

H. Capart and D.L. Young. Formation of a jump by the dam-break wave over a granular bed. *Journal of Fluid Mechanics*, 372:165–187, 1998.

J.T. Carley, T.D Shand, I.R. Coghlan, M.J. Blacka, R.J. Cox, A. Littman, B. Fitzgibbon, G. McLean, and P. Watson. Beach scraping as a coastal management option. *19th NSW Coastal Conference, Batemans Bay, NSW*, 2010. online at: www.coastalconference.com/2010/papers2010/James

G. F. Carrier and H. P. Greenspan. Water waves of finite amplitude on a sloping beach. *Journal of Fluid Mechanics*, 4:97–109, 1958.

D. Cayan and et.al. Climate change scenarios and sea level rise estimates for the california 2009 climate change scenarios assessment. *California Climate Change Center*, CEC-500-2009-014-F, 2009.

D.R. Cayan, P.D. Bromirski, K. Hayhoe, M. Tyree, M.D. Dettinger, and R.E. Flick. Cclimate change projections of sea level extremes along the california coast. *Climatic Change*, 87, 2008. S57-S73.

S. Chen and S. Peng. Two-dimensional numerical model of two-layer shallow water equations for confluence simulation. *Advances in Water Resources*, 29:1608–1617, 2006a.

S. Chen, S. Peng, and H. Capart. Two-layer shallow water computation of mud flow intrusions into quiescent water. *Journal of Hydraulic Research*, 45(1):13–25, 2007.

Su-Chin Chen and Szu-Hsien Peng. Two-dimensional numerical model of two-layer shallow water equations for confluence simulation. *Advances in water resources*, 29(11):1608–1617, 2006b.

G. Chust, I. Galparsoro, A. Borja, J. Franco, and A. Uriarte. Coastal and estuarine habitat mapping, using lidar height and intensity and multi-spectral imagery. estuarine. *Coastal and Shelf Science*, 78(4):633–643, 2008.

R. Clark. Hurricane dennis supplemental damage assessment report: Impact of hurricane dennis on dog island and discussion of post-storm recovery responses. *Florida Department of Environmental Protection, Division of Water Resource Management, Bureau of Beaches and Coastal System*, 2005.

N. Cox, L.M. Dunkin, and J.L. Irish. An empirical model for infragravity swash on barred beaches. *Coastal Engineering*, 81:44–50, 2013.

William R Dally. Random breaking waves: Field verification of a wave-by-wave algorithm for engineering application. *Coastal Engineering*, 16(4):369–397, 1992.

Richard J Dawson, Mark E Dickson, Robert J Nicholls, Jim W Hall, Mike JA Walkden, Peter K Stansby, Mustafa Mokrech, Julie Richards, Jianguo Zhou, Jessica Milligan, et al. Integrated analysis of risks of coastal flooding and cliff erosion under scenarios of long term change. *Climatic Change*, 95(1-2):249–288, 2009.

Paul de Groot. Swash zone sediment transport. Master's thesis, Delft University of Technology, Delft, The Netherlands, 2002.

R.A. Feagin, A.M. Williams, S. Popescu, J. Stukey, and R.A. Washington-Allen. The use of terrestrial laser scanning (tls) in dune ecosystems: The lessons learned. *Journal of Coastal Research*, 30(1):111–119, 2014.

J. Figlus, N. Kobayashi, C. Gralher, and V. Iranzo. Wave overtopping and overwash of dunes. *Journal of Waterway, Port, Coastal and Ocean Engineering*, 137(1):26–33, 2011.

R.E. Flick. Comparison of california tides, storm surges and mean sea level during the el nio winters of 1982-83 and 1997-98. *Shore and Beach*, 66(3):7–11, 1998.

L. Fraccarollo and H. Capart. Riemann wave description of erosional dam-break flows. *J. Fluid Mech.*, 461:183228, 2002.

L. Fraccarollo and E. F. Toro. Experimental and numerical assessment of the shallow water model for two-dimensional dam-break type problems. *Journal of Hydraulic Research*, 33: 843864, 1995.

L. Fraccarollo, H. Capart, and Y. Zech. A godunov method for the computation of the erosional shallow water transients. *Int. J. Numerical Methods Fluids*, 41:951976, 2003.

T. W. Gallien, P. L. Barnard, M. van Ormondt, A. C. Foxgrover, and B. F. Sanders. A parcel-scale coastal flood forecasting prototype for a southern california urbanized embayment. *Journal of Coastal Research*, 29(3):642–656, 2013.

T. W. Gallien, W.C. O'Reilly, and R.T. Guza. Geometric properties of anthropogenic flood control berms on southern california beaches. *Ocean and Coastal Management*, 105:35–47, 2015.

T.W. Gallien, J.E. Schubert, and B.F. Sanders. Predicting tidal flooding of urbanized embayments: A modeling framework and data requirements. *Journal of Coastal Engineering*, 58(6):567–577, 2011.

T.W. Gallien, B.F. Sanders, and R.E. Flick. Urban coastal flood prediction: Integrating wave overtopping flood defenses and drainage. *Journal of Coastal Engineering*, 91:18–28, 2014.

G. Garegnani, G. Rosatti, and L. Bonaventura. Free surface flows over mobile bed: mathematical analysis and numerical modeling of coupled and decoupled approaches. *Communications in Applied and Industrial Mathematics*, 2012. ISSN 2038-0909,e-371.

Marta Gonçalves, Eugen Rusu, and C Guedes Soares. Evaluation of two spectral wave models in coastal areas. *Journal of Coastal Research*, 31(2):326–339, 2015.

L Gorrell, Britt Raubenheimer, Steve Elgar, and RT Guza. Swan predictions of waves observed in shallow water onshore of complex bathymetry. *Coastal Engineering*, 58(6): 510–516, 2011.

H. Gotoh, S. Shao, and T. Memita. Sph-les model for numerical investigation of wave interaction with partially immersed breakwater. *Coastal Engineering Journal*, 46:39–63, 2004.

L. Goutire, S. Soares-Frazo, C. Savary, T. Laraichi, and Y. Zech. One-dimensional model for transient flows involving bed-load sediment transport and changes in flow regimes. *Journal of Hydraulic Eng., ASCE*, 86:726–735, 2008.

RT Guza and Edward B Thornton. Wave set-up on a natural beach. *Journal of Geophysical Research: Oceans (1978–2012)*, 86(C5):4133–4137, 1981.

S. Hanson, R. Nicholls, N. Ranger, S. Hallegatte, J. Corfee-Morlot, C. Herweijer, and J. Chateau. A global ranking of port cities with high exposure to climate extremes. *Climatic Change*, 104:89–111, 2011.

M.D. Harley and P. Ciavola. Managing local coastal inundation risk using real-time forecasts and artificial dune placements. *Coastal Engineering*, 77:77–90, 2013.

A. Harten, P.D. Lax, , and B. Van Leer. On upstream differencing and godunov-type schemes for hyperbolic conservation laws. *SIAM*, Rev. 25:3561, 1983.

M. Heberger and et.al. The impacts of sea-level rise on the california coast. *California Climate Change Center*, CEC-500-2009-024-F, 2009.

FM Henderson. Open channel flow. *MacMi1lan, New York*, 1966.

K. Hu, C.G. Mingham, and D.M. Causon. Numerical simulation of wave overtopping of coastal structures using the non-linear shallow water equations. *Coastal Engineering*, 41: 433465, 2000.

M.E. Hubbard and N. Dodd. A 2d numerical model of wave run-up and overtopping. *Coastal Engineering*, 47:1–26, 2002.

J. Hudson and P. Sweby. Formulations for numerically approximating hyperbolic systems governing sediment transport. *Journal of Scientific Computing*, 19:225–252, 2003.

N. Knowles. Potential inundation due to rising sea levels in the san francisco bay region. *San Francisco Estuary and Watershed Science*, 8(1), 2010.

M.G. Kratzmann and C.J. Hapke. Quantifying anthropogenically driven morphologic changes on a barrier island: Fire island national seashore. *Journal of Coastal Research*, 28(1):76–88, 2012.

S.N. Kuiry, W. Wu, and Y. Ding. A hybrid finite-volume/finite-difference scheme for one-dimensional boussinesq equations to simulate wave attenuation due to vegetation. *Proc. World Environmental and Water Resources Congress 2011*, 2011. Bearing Knowledge for Sustainability, ASCE 2011.

M. Larson, L. Erikson, and H. Hanson. An analytical model to predict dune erosion due to wave impact. *Coastal Engineering*, 51(4):675696, 2004.

N.A. Laudier, E.B. Thornton, and J. MacMahan. Measured and modeled wave overtopping on a natural beach. *Coastal Engineering*, 58:815–825, 2011.

P.L.F Liu, P. Lin, K.A. Chang, and T. Sakakiyama. Numerical analysis of wave overtopping of rubble mound breakwaters. *Journal of Waterway, Port, Coastal and Ocean Engineering*, 6(125):322–330, 1999.

I.J. Losada, J.L. Lara, R. Gunache, and J.M. Gonzalez-Ondina. Numerical analysis of wave overtopping of rubble mound breakwaters. *Coastal Engineering*, 55:47–62, 2008.

J. Liu M. R. Spiegel. *Mathematical Handbook of Formulas and Tables*. McGraw-Hill, New York, 1999.

Morteza Shakeri Majd and Brett F Sanders. The lhllc scheme for two-layer and two-phase transcritical flows over a mobile bed with avalanching, wetting and drying. *Advances in Water Resources*, 67:16–31, 2014.

L. Martinelli, B. Zanuttigh, and C. Corbau. Assessment of coastal flooding hazard along the emilia romagna littoral, it. *Coastal Engineering*, 57:1042–1058, 2010.

Gerd Masselink, Robert McCall, Tim Poate, and Pieter van Geer. Modelling storm response on gravel beaches using xbeach-g. *Proceedings of the ICE-Maritime Engineering*, 167(4): 173–191, 2014.

Gerhard Masselink and Paul Russell. Flow velocities, sediment transport and morphological change in the swash zone of two contrasting beaches. *Marine Geology*, 227(3):227–240, 2006.

Maurice McCabe, Peter K Stansby, and David D Apsley. Coupled wave action and shallow-water modelling for random wave runup on a slope. *Journal of Hydraulic Research*, 49(4): 515–522, 2011.

RT McCall, G Masselink, TG Poate, JA Roelvink, LP Almeida, M Davidson, and PE Russell. Modelling storm hydrodynamics on gravel beaches with xbeach-g. *Coastal Engineering*, 91:231–250, 2014.

RT McCall, G Masselink, TG Poate, JA Roelvink, and LP Almeida. Modelling the morphodynamics of gravel beaches during storms with xbeach-g. *Coastal Engineering*, 103:52–66, 2015.

Jesse McNinch and John T. Wells. Effectiveness of beach scraping as a method of erosion control. *Shore and Beach*, 1(60):13–20, 1992.

J. Murillo and P. Garcia-Navarro. Augmented versions of the hll and hllc riemann solvers including source terms in one and two dimensions for shallow flow applications. *Journal of Computational Physics*, 231:6861–6906, 2012.

N. Nagata, T. Hosoda, and Y. Muramoto. Numerical analysis of river channel processes with bank erosion. *Journal of Hydraulic Engineering*, 126(4):243–252, 2000.

Committee National Research Council. *Mapping the Zone. Improving Flood Map Accuracy.* The National Academies Press, Washington D.C., 2009. NCR's Committee on FEMA Flood Maps.

R.J. Nicholls. Impacts of and responses to sea-level rise. *Understanding Sea-Level Rise and Variability. Wiley-Blackwell.*, pages 17–51, 2010. In: Church, J.A., Woodworth, P.L., Aarup, T. and Wilson W.W., (eds.).

R.J. Nicholls. Planning for the impacts of sea level rise. *Oceanography*, 24(2):144–157, 2011.

R. Nobrega, J.A. Quintanilha, and C.G. O'Hara. A noise-removal approach for lidar intensity images using anisotropic diffusion filtering to preserve object shape characteristics. *Procedings of the ASPRS 2007 Annual Conference*, 2007. Tampa,Florida.

OCPW. *Geodetic Control/OCRTN*. County of Orange, California, Department of Public Works, 2009. Accessed at www.ocgeomatics.com/Documents/pdf/Procedures_for_using_OCRTN.pdf.

M.D. Orzech, Ad J.H.M Reniers, E.B. Thornton, and MacMahan J.H. Megacusps on rip channel bathymetry: Observations and modeling. *Coastal Engineering*, 58:890–907, 2011.

H. Tuba Ozkan-Haller and James. T. Kirby. A fourier-chebyshev collection method for the shallow water equations including shoreline runup. *Applied Ocean Research*, 19:2134, 1997.

D.H. Peregrine. Long waves on a beach. *Journal of Fluid Mechanics*, 27:815–827, 1967.

JA Puleo, KT Holland, NG Plant, DN Slinn, and DM Hanes. Fluid acceleration effects on suspended sediment transport in the swash zone. *Journal of Geophysical Research: Oceans (1978–2012)*, 108(C11), 2003.

Jack A Puleo, Tony Butt, and Nathaniel G Plant. Instantaneous energetics sediment transport model calibration. *Coastal engineering*, 52(7):647–653, 2005.

M.J. Purvis, P.D. Bates, and C.M. Hayes. A probabilistic methodology to simulate future coastal flood risk due to sea level rise. *Coastal Engineering*, 55:1062–1073, 2008.

M.T. Reis, K. Hu, T.S. Hedges, and H. Mase. A comparison of empirical, semiempirical, and numerical wave overtopping models. *Journal of Coastal Research*, 2B(24):250–260, 2008.

P.L. Roe. Approximate reiman solver, parametere vectors, and difference schemes. *Journal of Computational Physics*, 43:357–372, 1981.

D. Roelvink, A. Reniers, A. Van Dongeren, J. Van Thiel de Vries, McCall R., and J. Lescinski. Modelling storm impacts on beaches, dunes and barrier islands. *Coastal Engineering*, 56: 1133–1152, 2009.

J. Rogers, B. Hamer, A. Brampton, S. Challinor, M. Glennerster, P. Brenton, and A. Bradbury. Beach management manual (second edition). *CIRIA*, 2010. London,UK.

G. Rosatti and L. Begnudelli. An accurate well-balanced, generalized roe-type approach for the simulation of debris flows over mobile bed. *River Flow 2010, Dittrich, Koll, Aberle and Geisenhainer*, 2010.

G. Rosatti and L. Begnudelli. Two-dimensional simulation of debris flows over mobile bed: Enhancing the trent2d model by using a well-balanced generalized roe-type solver. *Computer and Fluids*, 71:179–195, 2013.

G. Rosatti and L. Fraccarollo. A well-balanced approach for flows over mobile-bed with high sediment-transport. *Journal of Computational Physics*, 220:312–338, 2006.

G. Rosatti, J. Murrillo, and L. Fraccarollo. Generalized roe schemes for 1-d two-phase, free-surface flows over a mobile bed. *Journal of Computational Physics*, 227:1058–10077, 2008.

Asbury Sallenger and et al. Evaluation of airborne topographic lidar for quantifying beach changes. *Journal of Coastal Research*, 19(1):125–133, 2003.

Asbury H. Jr. Sallenger. Storm impact scale for barrier islands. *Journal of Coastal Research*, 16(3):890–895, 2000.

C.C. Sampson, T.J. Fewtrell, A. Duncan, K. Shaad, M.S. Horritt, and P.D. Bates. Use of terrestrial laser scanning data to drive decimetric resolution urban inundation models. *Advances in Water Resources*, 41:1–17, 2012.

Alejandro Sanchez and Weiming Wu. A non-equilibrium sediment transport model for coastal inlets and navigation channels. *Journal of Coastal Research*, 59:3948, 2011.

Brett F. Sanders. Non-reflecting boundary flux function for finite volume shallow-water models. *Advances in Water Resources*, 25:195–202, 2002.

Jochen E Schubert, Timu W Gallien, Morteza Shakeri Majd, and Brett F Sanders. Terrestrial laser scanning of anthropogenic beach berm erosion and overtopping. *Journal of Coastal Research*, 31(1):47–60, 2014.

R.A.E.l Smith, P.D. Bates, and C. Hayes. Evaluation of a coastal flood inundation model using hard and soft data. *Environmental Modelling and Software*, 30:35–46, 2012.

S. Soares-Frazao and Y. Zech. Hllc scheme with novel wave-speed estimators appropriate for two-dimensional shallow-water flow on erodible bed. *Int. J. Numer. Meth. Fluids*, 66: 10191036, 2011.

J. P. Soni, R. J. Grade, and K. G. Raju. Aggradation in streams due to overloading. *Journal of Hydraulic division, ASCE*, 106(1):117–132, 1980.

B. Spinewine and Y. Zech. Geomorphic dam-break floods: Near-field and far-field perspectives. *Proceedings 1st Project Workshop, Wallingford, UK, 16- 17 May, EC Contract EVG1-CT-2001-00037 IMPACT Investigation of Extreme Flood Processes and Uncertainty, Accessed online at http://www.impact-project.net/cd/cd/default.htm*, 2002.

B. Spinewine and Y. Zech. Small-scale laboratory dam-break waves on movable beds. *Journal of Hydraulic Research*, 45:7386, 2007.

H.F. Stockdon, R.A. Holman, P.A. Howd, and A.H. Sallenger. Empirical parameterization of setup, swash, and runup. *Coastal Engineering*, 7(53):573–588, 2006.

B.H. Strauss, R. Ziemlinski, J.L. Weiss, and J.T. Overpeck. Tidally adjusted estimates of topographic vulnerability to sea level rise and flooding for the contiguous united states. *Environmental Research Letters*, pages 7–12, 2012.

C. Swartenbroekx, S. Soares-Frazao, R. Staquet, and Y. Zech. Two-dimensional operator for bank failures induced by water-level rise in dam-break flows. *Journal of Hydraulic Research*, 48(3):302314, 2010a.

C. Swartenbroekx, S. Soares-Frazo, R. Staquet, and Zech Y. Two-dimensional operator for bank failures induced by water-level rise in dam-break flows. *Journal of Hydraulic Research*, 48(3):302–314, 2010b.

C. Swartenbroekx, Y. Zech, and Soares-Frazo. Two-dimensional two-layer shallow water model for dam break flows with significant bed load transport. *Int. J. Numer. Meth. Fluids*, 73:477–508, 2013.

B.H. Tebaldi, C. Strauss and C.E. Zervas. Modelling sea level rise impacts on storm surges along us coasts. *Environmental Research Letters*, pages 7–12, 2012. doi:10.1088/1748-9326/7/1/014032.

M. Tonelli and M. Petti. Hybrid finite volume - finite difference scheme for 2dh improved boussinesq equations. *Coastal Engineering*, 56:609–620, 2009.

E.F. Toro. Riemann problems and the waf method for solving the two-dimensional shallow water equations. *Philosophical Transactions: Physical Sciences and Engineering*, 338 (1649):4368, 1992.

E.F. Toro. *Riemann Solvers and Numerical Methods for Fluid Dynamics.* Springer, Berlin,Germany, 1997.

R.S Tye. Impact of hurricane david and mechanical dune restoration on folly beach, south carolina. *Shore and Beach*, 51(2):3–9, 1983.

J.W. Van Der Meer and J.P.F.M. Janssen. Wave run-up and wave overtopping at dikes. *In: KOBAYASHI, N., and DEMIRBILEK, Z. (eds.), Wave Forces on Inclined and Vertical Wall Structures,New York: ASCE*, pages 1–27, 1995.

S. Van Emelen, C. Swartenbroekx, Y. Zech, and S. Soares-Frazo. Numerical modelling of the breaching process in an earthen dike. *Fifth International Conference on Advanced Computational Methods in ENgineering, Belguim*, pages 1–10, 2011.

S. Van Emelen, L. Schmocker, W.H. Hager, S. Soares-Frazo, and Y. Zech. Sediment transport models to simulate erosion of overtopped earth-dikes. *River Flow*, pages 449–506, 2012.

M.R.A. van Gent, J.S.M. van Thiel de Vries, E.M. Coeveld, J.H. de Vroeg, and J. van de Graaff. Large-scale dune erosion tests to study the influence of wave periods. *Coastal Engineering*, 55:10411051, 2008.

Leo C. van Rijn. Prediction of erosion due to stroms. *Coastal Engineering*, 56:441–457, 2009.

G. Vossman and H.G. Maas. *Airborne and Terrestrial Laser Scanning*. Whittles Publishing, 2010. Dunbeath, Scotland, UK.

M.I. Vousdoukas, O. Ferreira, L.P. Almeida, and A. Pacheco. Toward reliable storm-hazard forecasts: Xbeach calibration and its potential application in an operational early-warning system. *Ocean Dynamics*, 62(7):1001–1015, 2012.

M.I. Vouskoukas, T. Kirupakaramoorthy, H. Oumeraci, M. de la Torre, F. Wubbold, B. Wagner, and S. Schimmels. The role of combined laser scanning and video techniques in monitoring wave-by-wave swash zone processes. *Coastal Engineering*, 83(1):150–165, 2014.

M.P. Wadey, R.J. Nicholls, , and C. Hutton. Coastal flooding in the solent: An integrated analysis of defences and inundation. *Water*, 4:430–459, 2012.

Group WAFO. WAFO - a matlab toolbox for analysis of random waves and loads - a tutorial. pages 35–47, 2000. URL `http://www.maths.lth.se/matstat/wafo`.

J.T. Wells and J. McNinch. Beach scraping in north carolina with special reference to its effectiveness during hurricane hugo. *Journal of Coastal Research*, 8:249–261, 1991.

W. Wu and S. Y. Wang. One-dimensional explicit finite-volume model for sediment transport with transient flows over movable beds. *J. Hydraulic Research*, 46(1):87–98, 2008.

W. Wu, R. Marsooli, and Z. He. Depth-averaged two-dimensional model of unsteady flow and sediment transport due to noncohesive embankment break/breaching. *Journal of Hydraulic Engineering*, 138(6):503–516, 2002.

Weiming Wu. *Computational river dynamics*. Taylor and Francis, London, 2007.

Weiming Wu, Mustafa S Altinakar, Scott F Bradford, Qin J Chen, Serban G Constantinscu, Jennifer G Duan, D Michael GEE, Blair Greimann, Greg Hanson, Zhiguo HE, et al. Earthen embankment breaching. *Journal of hydraulic engineering*, 137(12):1549–1564, 2011.

M.L. Yates, R.T. Guza, R. Gutierrez, , and R. Seymour. A technique for eliminating water returns from lidar beach elevation surveys. *Journal of Atmospheric and Oceanic Technology*, 25(9):1671–1682, 2008.

Y. Zech, S. Soares-Frazo, B. Spinewine, and N. Le Grelle. Dam-break induced sediment movement: Experimental approaches and numerical modelling. *Advances in Water Resources*, 46(2):176190, 2008.

Y. Zech, S. Soares-Frazo, B. Spinewine, C. Savary, and L. Goutiere. Inertia effects in bed-load transport models. *Canadian Journal of Civil Engineering*, 36:1587–1597, 2009.

F. Zhu and N. Dodd. Net beach change in the swash zone: A numerical investigation. *Advances in Water Resources*, 53:12–22, 2013.

M. Zijlema, G. Stelling, and Smit P. Swash: An operaional public domain code for simulating wave field and rapidly varied flows in coastal waters. *Coastal Engineering*, 58:992–1012, 2011.